The University of Osaka
Institutional Knowledge Archive

| | |
|---|---|
| Title | Photodisintegration of 3He in the peak region |
| Author(s) | 内藤, 晋 |
| Citation | 大阪大学, 2001, 博士論文 |
| Version Type | VoR |
| URL | https://doi.org/10.18910/43613 |
| rights | |
| Note | |

*The University of Osaka Institutional Knowledge Archive : OUKA*

https://ir.library.osaka-u.ac.jp/

The University of Osaka

(博士論文題名) Photodisintegration of $^3$He in the peak region

(氏　　名) 内藤 晋

(専 攻 名) 物理学

大阪大学大学院理学研究科

# Photodisintegration of $^3$He in the peak region

Susumu Naito [1]

June 12, 2001

[1]Research Center for Nuclear Physics in Osaka University

# Contents

**Abstract** **1**

**1 Introduction** **1**
1.1 General . . . . . 1
1.2 Previous experiments . . . . . 2
1.2.1 Two-body breakup . . . . . 2
1.2.2 Three-body breakup . . . . . 2
1.2.3 Total cross section . . . . . 3
1.3 Theoretical work . . . . . 11
1.4 Comparison of experimental values with theoretical ones . . . . . 17
1.5 Aim of the present study . . . . . 17

**2 Experimental methods and procedures** **25**
2.1 Outline of experimental methods and procedures . . . . . 25
2.2 LCS $\gamma$-ray source . . . . . 28
2.2.1 Principle . . . . . 28
2.2.2 Generating $\gamma$-rays . . . . . 30
2.3 $\gamma$-ray monitor . . . . . 33
2.4 Operation principle of the TPC . . . . . 34
2.4.1 Outline of operation principle . . . . . 34
2.4.2 The motion of a charged particle in gases . . . . . 36
2.4.3 The electron motion in the electric field . . . . . 39
2.4.4 The amplification of electrons in the strong electric field . . . . . 39
2.4.5 Signal at MWPC . . . . . 40
2.5 Design of our TPC . . . . . 42
2.6 Target gas . . . . . 45
2.7 Electronics and data acquisition . . . . . 47
2.8 Noise reduction . . . . . 47
2.9 Performance of TPC system . . . . . 50

**3 Measurements and data analysis** **52**
3.1 The condition of the measurement . . . . . 52
3.2 Data analysis of TPC . . . . . 53
3.2.1 Reconstruction of trajectories . . . . . 53
3.2.2 Analysis of events . . . . . 55
3.2.3 The number of events . . . . . 64
3.2.4 Detection efficiency of TPC and Effective length . . . . . 65
3.2.5 The number of target atomic nuclei . . . . . 81
3.3 Determinant of $\gamma$-ray flux and $\gamma$-ray energy distribution . . . . . 83
3.3.1 $\gamma$-ray flux . . . . . 83
3.3.2 Energy distribution . . . . . 87
3.4 Results . . . . . 92

**4 Discussion and conclusion** **93**
4.1 Discussion . . . . . 93
4.1.1 Comparison of the present results with previous experiments . . . . . 93
4.1.2 Comparison of the present results with theoretical values . . . . . 94
4.2 Conclusion . . . . . 100

**A Development of multipass system** **105**
A.1 Introduction . . . . . 105
A.1.1 History of the development . . . . . 105
A.1 .2 Our design . . . . . 106
A.2 Optical system . . . . . 108
A.2.1 Principle . . . . . 108
A.2.2 Details of the optical system . . . . . 109
A.3 Mirror chamber . . . . . 115
A.4 Measurements . . . . . 116
A.5 Results . . . . . 118
A.6 Discussion . . . . . 120
A.7 Conclusion . . . . . 121

## Abstract

The two-body and three-body photodisintegration cross sections of $^3$He have been measured at $E_\gamma$=10.5 and 16.5 MeV. These energies are theoretically predicted to give the maximum values for the two-body breakup and total cross sections, respectively, and the cross sections are claimed to be very sensitive to the potentials employed in the calculations. Since the experimental values so far made for the two-body breakup and total cross sections have large errors and are so much scattered between various data sets, one cannot test the theoretical calculations. Therefore in the present study we aimed at measuring these cross sections accurately using a newly constructed time projection chamber (TPC) and laser Compton backward-scattering (LCS) photon beams.

Since the TPC contains an active gas target of $^3$He together with the quenching gas of methane, charged particles from the photodisintegration of $^3$He can be detected with almost 100% detection efficiency a large acceptance of $4\pi$ geometry. Hence the two-body and three-body breakup reaction can be simultaneously measured. The TPC has also high capability for distinguishing true events from background, which can be made by using the tracks of the charged particles. The LCS photon beam with quasi-monochromatic energy can be well-collimated and it's beam intensity can be precisely measured. These characteristic points of the TPC and LCS are crucial to determine the cross sections accurately. The experiment was successfully carried out and the present results are discussed by comparing with the recent calculations.

In order to further extend this study, it is quite useful to increase the photon intensity. Therefore we have newly developed the equipment to increase the photon intensity, which is called the multipass system. With this equipment, we could increase the photon intensities by a factor of about 3 compared to the intensities without the equipment. The result indicates that this equipment is useful for the precise measurement of the $^3$He photodisintegration.

# 1. Introduction

## 1.1 General

The studies of the three-nucleon system have been one of the most fundamental ones in nuclear physics and many works have been carried out both experimentally and theoretically. Since there have been big advances on the techniques for calculating scattering and reaction processes for the three-nucleon system and on the quality of nucleon-nucleon (NN) potentials [1][2], the three-nucleon system provides an excellent laboratory to study of nuclear physics beyond the two-body system. Many high precision experimental results have been compared with predicted values of exact quantum mechanical calculations based the high quality NN potentials. From the comparison one hopes to test of our understanding of the NN potentials and to explore the possible role of three-body forces in nuclear reactions. Theoretically three-body forces are expected to exist. However, experimentally we see only circumstantial evidence of the existence of the three-body forces, which comes from the binding energies of the mass 3 and 4 nuclei. Namely, it has been claimed that if one takes only two-body interaction into account, one obtains the underestimated value of the binding energies for both $^3$H and $^3$He compared to the measured values. Hence, one needs to include the effect of three-nucleon forces. Although the three-nucleon forces are expected to exist theoretically, the forces are exceedingly complicated and it is difficult to develop any intuitive understanding of how three-nucleon forces affect the wave function of the three-nucleon systems. Hence, it is very important to study in detail observables in which three-nucleon forces influence the wave functions in the three-nucleon systems. Actually a lot of efforts have been made to detect the effects of three-body forces on nuclear reaction. So far, however, these efforts have not yet been successful.

The aim of the present work is to measure precisely the absolute photodisintegration cross sections of $^3$He to study of our understanding of the NN potentials and to explore the possible role of the three-body forces. Among the various reaction studies of the three-nucleon system, the photodisintegration studies are quite useful. This is because the ground state of $^3$He is well understood, the interaction is well known, and the disintegration process is purely an E1 at low energies ($E\gamma < 40 MeV$).

## 1.2 Previous experiments

The cross sections of the two-body and three-body photodisintegrations for the three nucleon system at low energies have been measured using bremsstrahlung beam and mono-energetic photons from the annihilation in flight of fast positrons and the corresponding inverse nucleon-deuteron reaction as mentioned below.

### 1.2.1 Two-body breakup

The electron bremsstrahlung beam was used to measure the two-body breakup cross section of $^3$He by Fetisov *et al.* and Ticcioni *et al.*. Fetisov *et al.* measured the cross section of the two-body breakup of $^3$He from the threshold to 170MeV using a cloud chamber filled with $^3$He and Ticcioni *et al.* measured the angular distribution of deuterons using a magnetic spectrometer and Si detectors. Kundu *et al.* measured the cross section using the $^3$He(e,e')pd reaction and a theoretical virtual photon spectrum. While Skopik *et al.* used the inverse D(p,$\gamma$)$^3$He reaction and obtained the cross sections by measuring the $\gamma$-ray angular distribution using NaI(Tl) detectors. On the other hand, the cross section of $^3$H was measured by Faul *et al.* using mono-energetic photons from the annihilation in flight of fast positrons and detecting neutrons from the reaction with $BF_3$ counters. The cross section results of the two-body photodisintegration for $^3$H and $^3$He, so far measured, are summarised in Tables 1.1 and 1.2, and shown in Figs.1.1 and 1.2, respectively. The measured cross sections for $^3$H agree each other within an experimental error up to 15MeV, while for energies above 20MeV there is a large discrepancy between the different data sets. For $^3$He, there are large discrepancies between the different data sets around 11 MeV and the discrepancies become small above around 16MeV. Here it should be noted that two results, the most recent one by Skopik *et al.* and the result by Fetisov *et al.*, who measured also the three-body breakup cross section, deviates considerably from the results by Wolfli *et al.* and Ticcioni *et al.*.

### 1.2.2 Three-body breakup

The three-body photodisintegration cross sections for $^3$H were measured only by Faul *et al.* and those for $^3$He were measured by Fetisov *et al.* and Faul *et al.*. Their experimental methods are same as mentioned above. The experimental results for $^3$H and $^3$He, so far measured, are summarised in Tables 1.3 and 1.4, and are shown in Figs. 1.3 and 1.4, respectively. The results for $^3$He agree with each other within an experimental error.

### 1.2.3 Total cross section

The total cross section was obtained by adding the measured two-body and three-body photodisintegration cross section. The total cross sections were thus obtained by Faul *et al.* for $^3$H and Fetisov *et al.* for $^3$He, respectively, and the results are shown in Figs.1.5 and 1.6, respectively. In figs.1.6 the total cross section of $^3$He derived by Faul *et al.* is also shown as a dotted line. It is obtained by adding their data for the three-body breakup and other group's data for the two-body breakup.

Table 1.1: Summary of the measured $^3\mathrm{H}(\gamma, n)D$ cross-sections.

| Reaction | Author | Ref. | Year | Beam | Target | Detected particles | Assumed systematic error |
|---|---|---|---|---|---|---|---|
| D(p,$\gamma$)$^3$He | Bösch | [3] | 1964 | $\gamma$ | $^3$H(gas) | n | |
| $^3$H($\gamma$,n)D | Kosiek | [4] | 1966 | $\gamma$(bremss.) | $^3$H(gas) | D | 20% |
| $^3$H($\gamma$,n)D | Faul | [5] | 1981 | $\gamma$(anihilation) | $^3$H(gas) | n | 5% |
| $^3$H($\gamma$,n)D | Skopik | [6] | 1981 | $\gamma$(bremss.) | $^3$H(solid) | D | |
| D(n,$\gamma$)$^3$H | Mitev | [7] | 1986 | n | $D_2O$(liquid) | $\gamma$ | |
| D(n,$\gamma$)$^3$H | Mösner | [8] | 1986 | n | $D_2$(gas) | $^3$H | |

Table 1.2: Summary of the measured $^3$He$(\gamma, p)D$ cross sections.

| Reaction | Author | Ref. | Year | Beam | Target | Detected particles | Assumed systematic error |
|---|---|---|---|---|---|---|---|
| D(p,$\gamma$)$^3$He | Griffiths | [9] | 1962 | p | $D_2O$ solid/ /D gaseous | $\gamma$ | 10% |
| $^3$He($\gamma$,p)D | Warren | [10] | 1963 | $\gamma$ | 3He(gas) | p/D | (7-16)% |
| $^3$He($\gamma$,p)D | Fetisov | [11] | 1965 | $\gamma$(brems.) | 3He(gas) | p/D | 6% |
| D(p,$\gamma$)$^3$He | Wolfli | [12] | 1966 1967 | p | $D_2$(gas) | $\gamma$ | 10% |
| p(D,$\gamma$)$^3$He | Belt | [13] | 1970 | D | polystrene | $^3$He | 8% |
| p(D,$\gamma$)$^3$He | Woude&Belt | [14] | 1971 | D | polystrene | $^3$He | 8% |
| $^3$He($\gamma$,D)p | Kundu | [15] | 1971 | $e^-$ | $^3$He(gas) | D | 15% |
| $^3$He($\gamma$,p)D | Ticcioni | [16] | 1973 | $\gamma$(brems.) | $^3$He(gas) | D | 5% |
| D(p,$\gamma$)$^3$He | Matthews | [17] | 1974 | p | deutrated polyethylene | $^3$He | 10% |
| D(p,$\gamma$)$^3$He | Skopik | [18] | 1979 | p | $CD_2$(powder) | $\gamma$ | |

Table 1.3: Summary of the measured $^3$H$(\gamma, nn)p$ cross sections.

| Reaction | Author | Ref. | Year | Beam | Target | Detected particles | Assumed systematic error |
|---|---|---|---|---|---|---|---|
| $^3$H($\gamma$,nn)p | Faul | [5] | 1981 | $\gamma$(annihilation) | $^3$H(gas) | n | (8-15)% |

Table 1.4: Summary of the measured $^3$He$(\gamma, pp)n$ cross sections.

| Reaction | Author | Ref. | Year | Beam | Target | Detected particles | Assumed systematic er |
|---|---|---|---|---|---|---|---|
| $^3$He($\gamma$,pp)n | Fetisov | [11] | 1965 | $\gamma$(brems.) | $^3$He(gas) | p/D | 10% |
| $^3$He($\gamma$,pp)n | Gerstenberg | [19] | 1966 | $\gamma$(brems.) | $^3$He(liquid) | n | 10% |
| $^3$He($\gamma$,pp)n | Berman | [20] | 1974 | $\gamma$(annihilation) | $^3$He(liquid) | n | 10% |
| $^3$He($\gamma$,pp)n | Faul | [5] | 1981 | $\gamma$(annihilation) | $^3$He(gas) | n | (8-15)% |

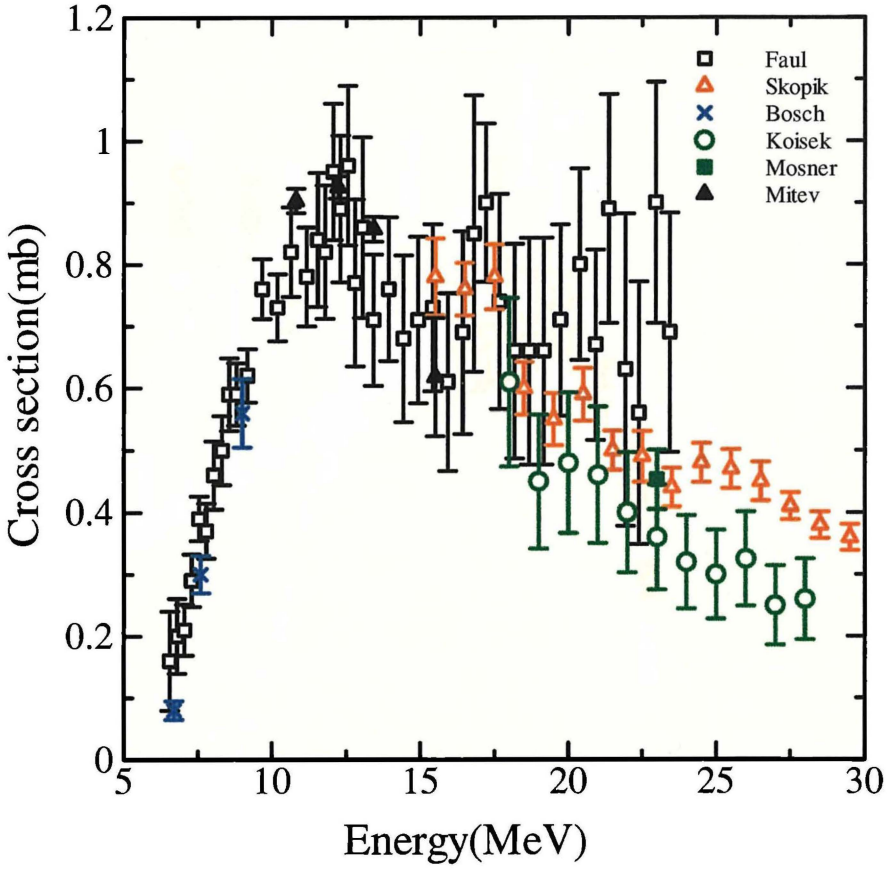


Figure 1.1: Measured cross sections of the $^3$H($\gamma$,n)d reaction

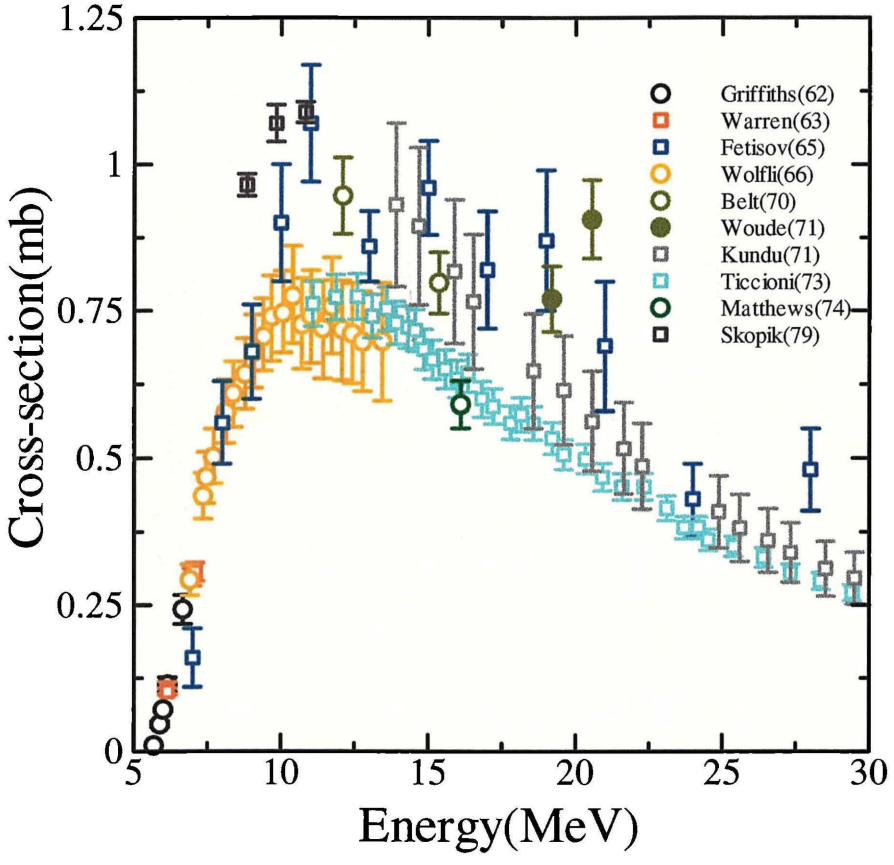


Figure 1.2: Measured cross sections of the $^3$He($\gamma$,p)d reaction

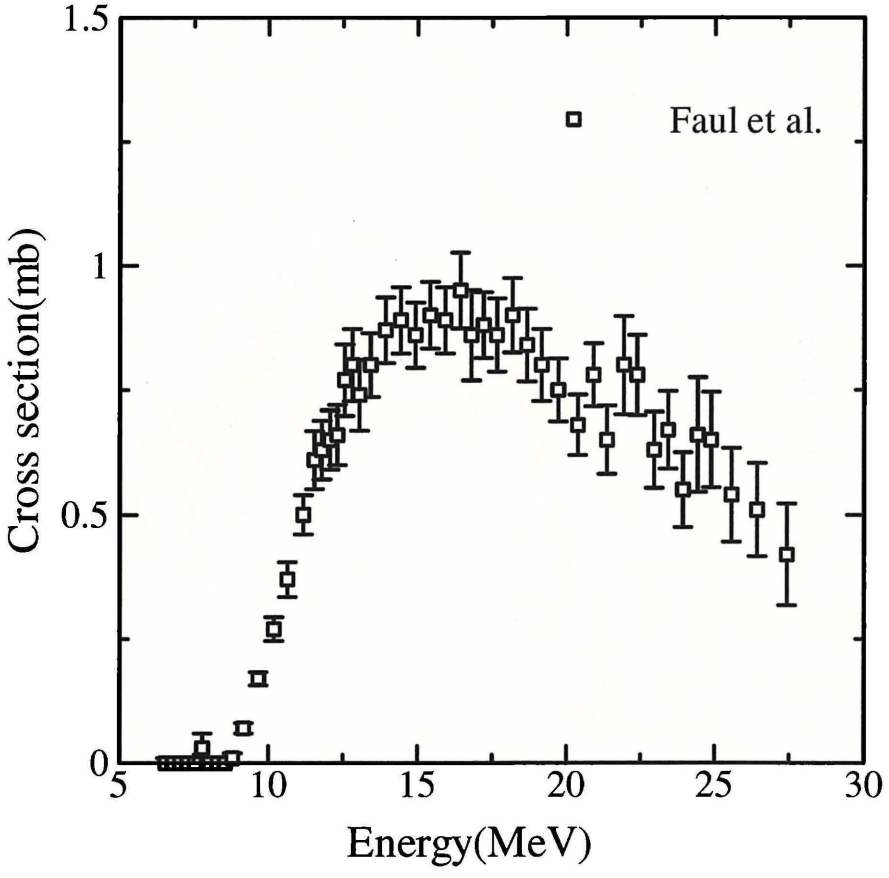


Figure 1.3: Measured cross sections of the $^3$H($\gamma$,nn)p reaction

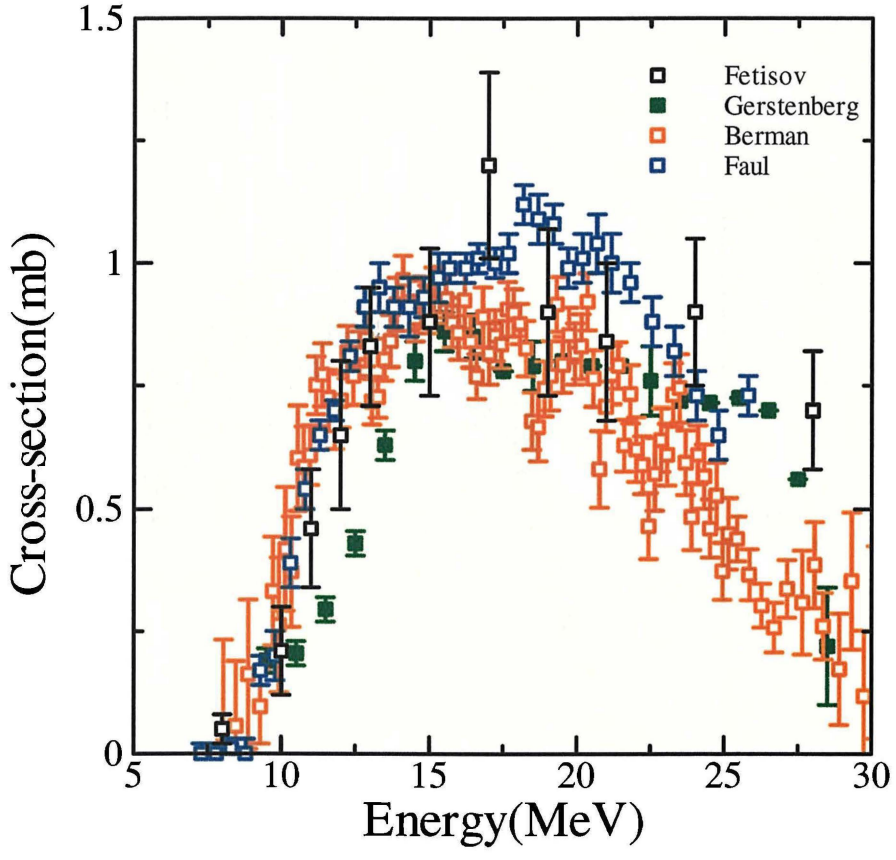


Figure 1.4: Measured cross sections of the $^3$He($\gamma$,pp)n reaction

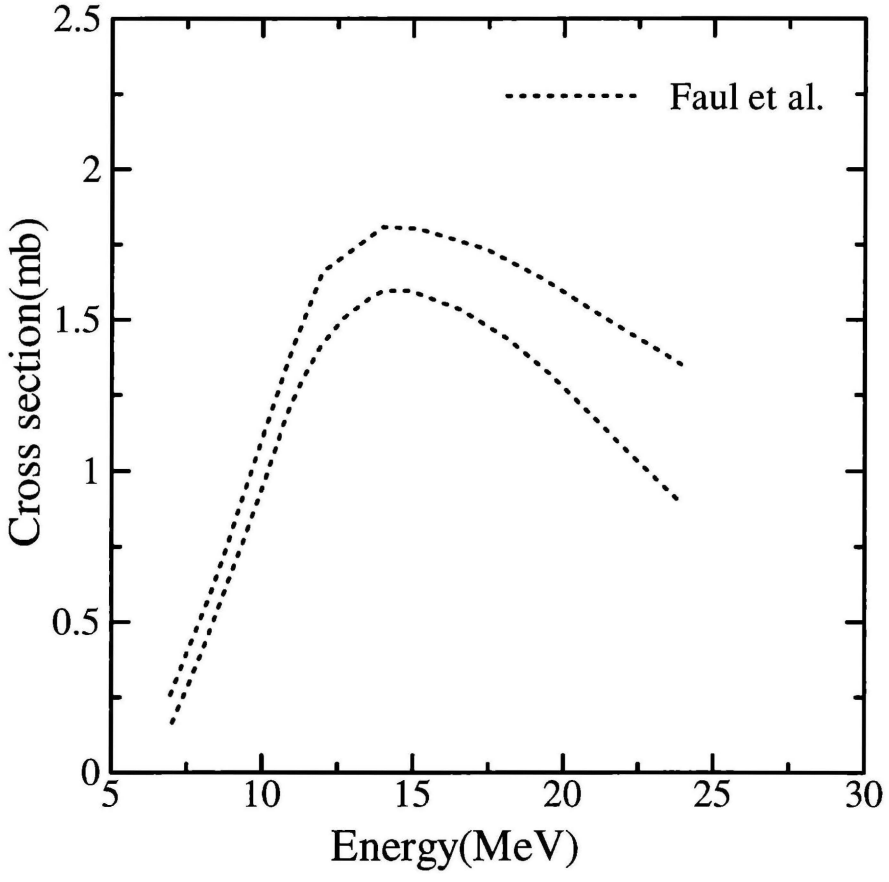


Figure 1.5: Measured total cross sections of the $^3$H photodisintegration with error range (dotted curves)

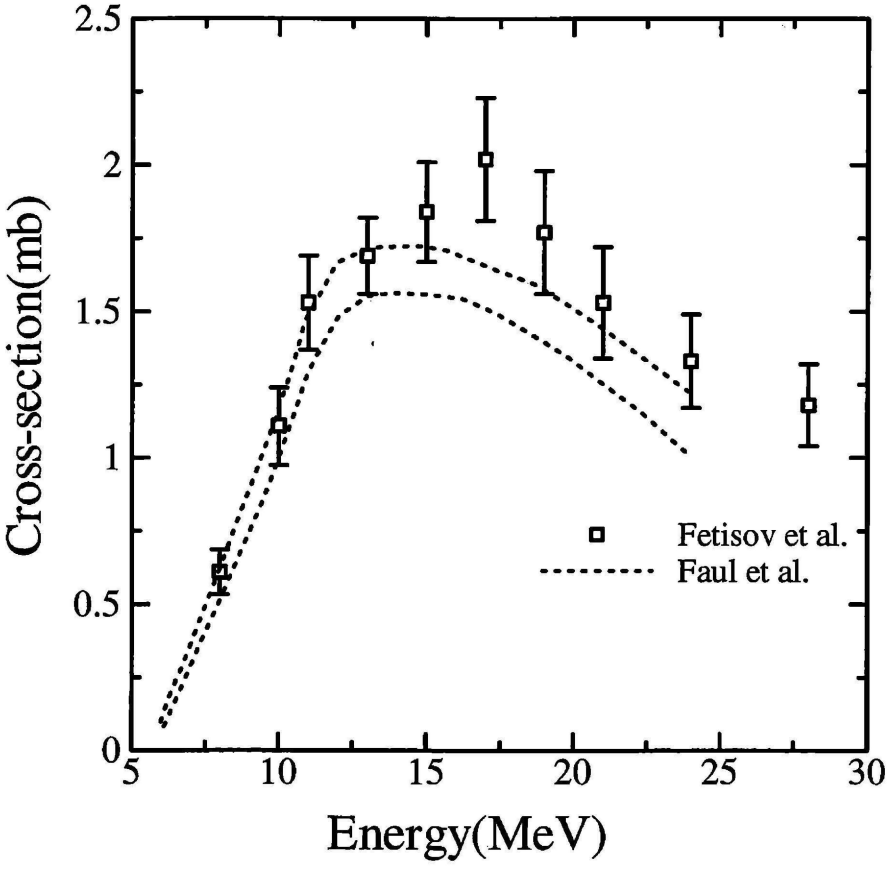


Figure 1.6: Measured total cross sections of the $^3$He photodisintegration

## 1.3 Theoretical work

The photodisintegrations of $^3$H and $^3$He in the low energy region ($E_\gamma < 50MeV$) have been studied theoretically by two basically different methods; the Faddeev equations in momentum space [21][22][23] and the Lorentz integral transformation method[24] using expansions in the correlated hyperspherical harmonic (CHH) basis in configuration space[25]. Theoretical calculations of the cross sections of the two-body and three-body photodisintegrations of $^3$He based on the Faddeev approach was made for the first time by Barbour and Phillips (BP)[26][27]. They considered the three-particle aspects of the nucleon-deuteron and three-nucleon final states, and the distortion of the deuteron for the nucleon-deuteron state. Using the Faddeev approach one can treat the three-particle aspects of the three-nucleon system exactly, and thus the two- and three- body photodisintegration channels can be related. Actually it was shown that the particular two-nucleon interaction which is responsible for the deuteron, and hence allows the existence of the two-body disintegration channel, has a large effect via the final-state interactions in the three-body channel[28]. It would be clear that if the two-nucleon interaction is weakened so that the deuteron is no longer bound, then the disappearance of the two-body disintegration channel would lead a large increase in the three-body cross section. Barber and Phillips calculated the continuum amplitudes assuming the disintegration process was purely an electric dipole (E1). As for the $^3$He ground state wave function, they used a phenomenological form which was obtained by separable interactions, and set the binding energy to the experimental value and used the root-mean-squared (rms) radius to fix the remaining parameter introduced. In this way, they succeeded for the first time to eliminate the theoretical overestimate, by about a factor of two, for the three-body breakup channel of $^3$He and also to recover the 30% underestimate of the two-body cross section.

Then the first consistent calculation of the photodisintegration of the three-nucleon system for both the initial and the final state was carried out by Gibson and Lehman[29][30]. They used the same interactions to obtain both the bound and continuum states, and they solved the Faddeev type equations using Yamaguchi interactions and taking into account only the E1 contributions. Since the bound and continuum states derive from the same Hamiltonian, this leads to consistently better agreement with the measured total cross section data than the calculations by BP. They also calculated the cross section of the three-body photodisintegration of $^3$He.

Quite recently, Schadow and Sandhas *et al.* have calculated the cross section of the two-body breakup for $^3$H and $^3$He based on the Faddeev approach[31]. They used the various realistic NN potentials, such as Paris[32], Bonn A and Bonn B[33] potentials. All calculations are carried out with theoretical binding energies. Their results for $^3$H and $^3$He are shown in Figs. 1.7 and 1.8, respectively, where one sees clearly a remarkable potential dependence of the cross section in the peak region, which is quite useful to test the potentials employed.

On the other hand, the Lorentz integral transformation method combined with the variational technique has been developed to calculate the photodisintegration cross section of the

three-nucleon system. It has been claimed that since the transform can be obtained using bound-state type methods, one does not need to solve the complicated continuum wave functions. This is the essential point of the transform. Several accurate variational techniques have been developed to solve the three- and four-nucleon bound system. One of the merits of the variational method is that the convergence in the number of decomposition channels is faster than in the Faddeev technique due to the absence of a partial-wave expansion of the potential. One sees the point in the treatment of the pp Coulomb interaction. As it is well known, the nuclear and Coulomb potential are expanded in channels with increasing angular momenta and the expansion is enlarged with a satisfactory convergence for the wave function of the system and the part of potential taken into account is found. The expansion in partial waves of the Coulomb interaction, however, is slowly convergent. In the variational treatment, although the wave function is expanded in channels, the interaction is fully taken into account as no expansion of the potential is made. The variational technique has been developed to reduce all the relevant details of the investigated structure by increasing the number of trial parameters and by using the computer to carry out the numerical calculation. However, the variational treatment of the bound and scattering states of the three-nucleon system with realistic potentials have encountered the difficulties. One possible solution is to use adequate expansion bases for the radial dependence of each channel in the wave function expansion. Since the NN interaction produces strong nucleon-nucleon correlations, it is convenient to introduce sets of basis functions, which are able to include these correlations. Thus the correlated hyperspherical harmonic (CHH) expansions have been introduced as sets of basis functions. It has been claimed that the advantage of the CHH expansion is it's possibility to treat potentials with infinite NN repulsion. In the calculation for the three-nucleon problem potentials with a hard-core repulsion have not been used due to the difficulty of performing accurate calculations. It is known that the Faddeev techniques are not directly applicable when an infinite repulsion exists. While the CHH expansion technique can be shown to guarantee that each channel in the wave function will vanish when the distance of any pair of particles is less than the hard-core radius.

Total cross sections of the photodisintegrations for $^3$H and $^3$He have been calculated in the framework of the correlated hyperspherical harmonic basis method together with the Lorentz integral transform method by Efros *et al.*[34]. Here as discussed above the transforms can be calculated without knowing the continuum wave functions. The total cross sections have been performed using realistic NN and NNN forces; final state interactions are fully included. In the calculation, two NN potential models, the AV14[35] and Bonn-A potentials are considered, and for the three-nucleon forces the Urbana-VIII [36] and Tucson-Melbourne [37] models are employed. The results for the total $^3$H and $^3$He photodisintegration cross sections are shown in Figs.1.9 and 1.10, respectively, where the AV14 and AV14+UrbVIII potentials were used in the calculation. The similar peak height of the cross sections for these rather different potentials is due mostly to the similarity of the ground state proton radii computed from these potentials. While in all cases the calculation with NNN forces in addition to realistic NN forces reduces the cross section by about 10% in the peak region,

which can be understood that the addition of NNN forces increases the binding energy and thus decreases the radius. Hence accurate measurements of the total cross sections are quite important to pick up the three-body forces.

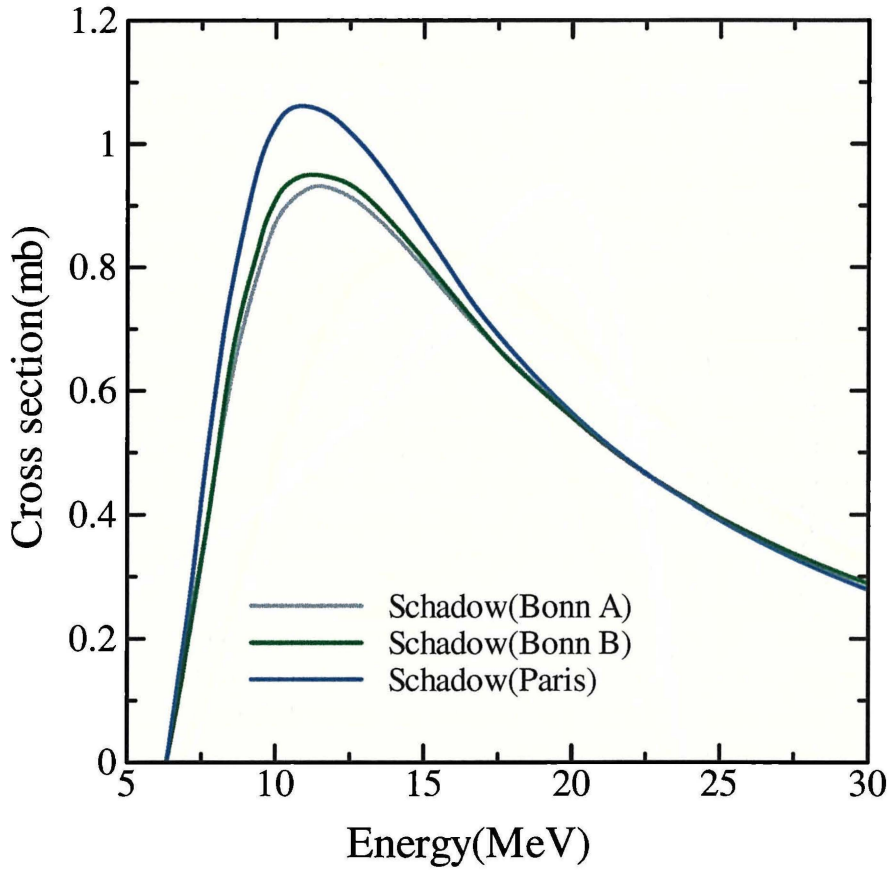


Figure 1.7: Calculated cross sections of the $^3$H($\gamma$,n)d reaction with Bonn A, Bonn B and Paris potentials.

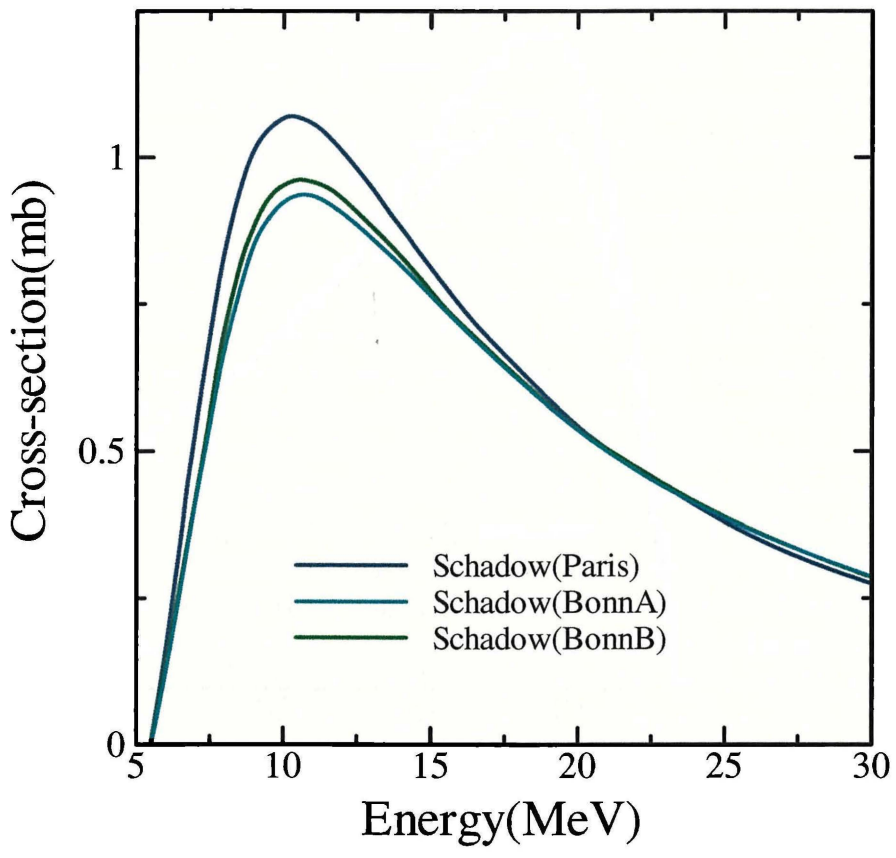


Figure 1.8: Calculated cross sections of the $^3$He($\gamma$,p)d reaction with Bonn A, Bonn B and Paris potentials

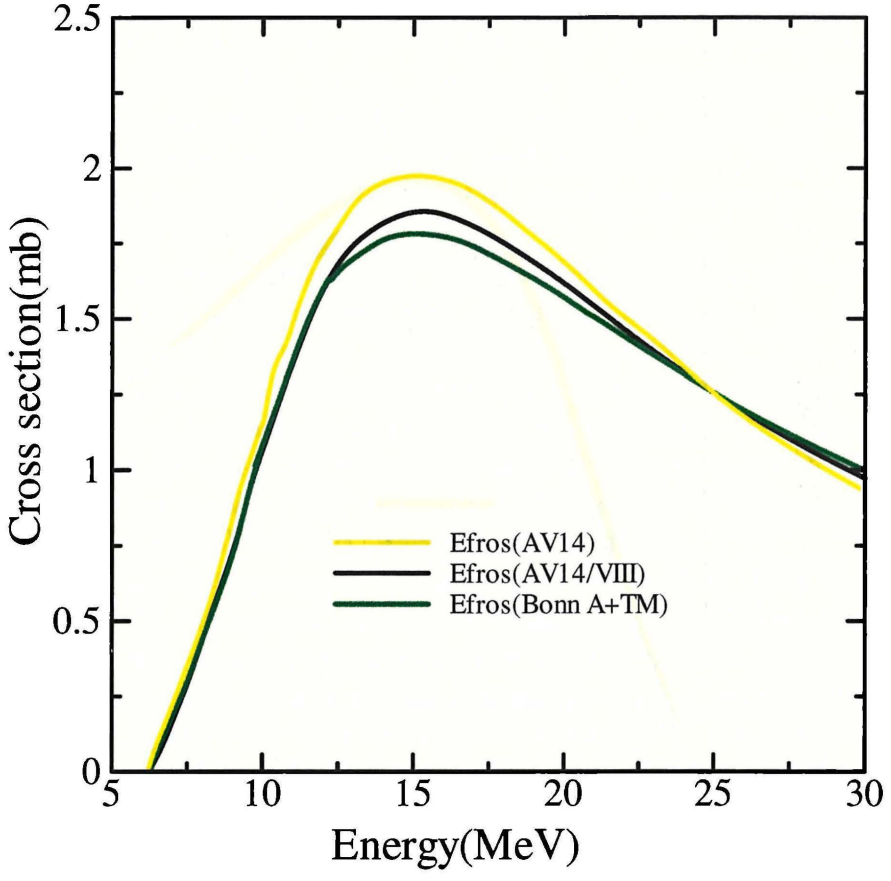


Figure 1.9: Calculated total cross sections of the $^3$H photodisintegration with AV14, AV14+VIII, and Bonn A + TM potentials.

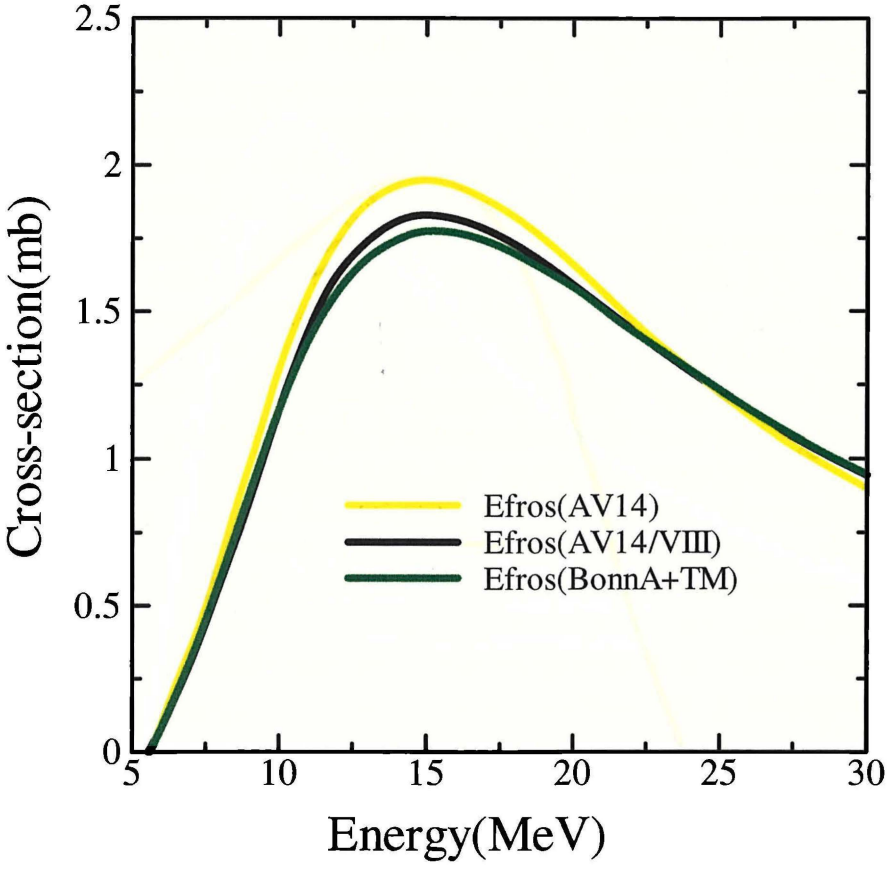


Figure 1.10: Calculated total cross sections of the $^3$He photodisintegration with AV14, AV14+VIII, and Bonn A + TM potentials.

## 1.4 Comparison of experimental values with theoretical ones

The measured two-body breakup, three-body breakup and total cross sections of the photodisintegrations for $^3$H and $^3$He are compared with several theoretical calculations.

In Fig.1.11 theoretical results for the two-body breakup of $^3$H calculated by Schadow *et al.* are compared with most of the experimental data. In the peak region, the theoretical values for the Bonn A and Bonn B potentials roughly agree with the experimental data within an experimental error. While for energies above 20MeV there is a large discrepancy between the different data sets, and these data do not agree with the theoretical calculations. Namely, although one sees a remarkable potential dependence of the cross sections of the theoretical two-body breakup, the measured values are so much scattered and it is not possible to test the theoretical models. Hence it is quite important to carry out more precise measurements of the two-body breakup of $^3$H.

In Fig.1.12 the same comparisons as for $^3$H are made for $^3$He. As one sees, there are large discrepancies between the different data sets around 11 MeV, and the theoretical values for the Bonn A and Bonn B potentials lie in between the data sets. The discrepancy of the experimental data becomes small for energies above 20 MeV, and one sees that the theoretical values for the different potentials agree with each other and with the experimental values within experimental error bars. Here due to the large discrepancies of the experimental values around 11MeV one cannot test the potentials used. It is again quite important to make precise measurements of the two-body breakup of $^3$He.

In Fig.1.13 the measured three-body breakup cross section for $^3$He is compared with the old calculation, since the theoretical calculation using realistic NN interactions has not yet been performed. The experimental results agree with the calculated ones by Gibson *et al.* within experimental error bars except for the low energy region below 12MeV.

In Figs.1.14 and 1.15 the total cross sections obtained for $^3$H and $^3$He are compared with the theoretical ones. For $^3$H it is clearly seen that the full calculation with three-body force is in agreement with the measured one within experimental error bars, while the calculation with the AV14 alone overestimates the cross section. Hence, it seems that the three-body force plays an important role in the photodisintegration of $^3$H.

For $^3$He the total cross sections obtained by Fetisov *et al.* are in agreement with the theoretical ones, although the experimental error is so large that one can not test the potentials used here.

## 1.5 Aim of the present study

The theoretical calculations for the two-body breakup and total cross sections for $^3$H and $^3$He have a remarkable potential dependence at the corresponding peak regions as shown in Figs. 1.11, 1.12, 1.14, and 1.15. The experimental values, however, are so much scattered

and/or have large error bars, and thus they can not be used to discriminate the theoretical models. Therefore it is very important to carry out precise measurements of the two-body, three-body breakup and total cross sections of the three-nucleon system at low energies, especially in the peak energy regions of the corresponding reaction channels, where there is a large potential dependence.

The aim of the present study is to determine accurately the absolute cross sections of the two-body and three-body photodisintegration of $^3$He at the photon energies of 10.5 and 16.5 MeV and to test of our understanding of the NN potentials and to explore the possible roles of the three-body force. In this study we use a newly developed Time Projection Chamber and a Laser-Compton Backscattering (LCS) photon. Since the maximum cross sections for the two-body and total photodisintegration of $^3$He have been theoretically predicted to be at around 10.5 and 16.5 MeV, we have chosen the energies.

The reason why we have chosen $^3$He sample for studying the photodisintegration of the three-body system is as follows. The total cross sections of $^3$H and $^3$He have been calculated by Efros *et al.* as shown in Fig. 1.16, where one sees that the effect of the Coulomb force is very small and the cross sections are almost same for $^3$H and $^3$He. Since in this study we aim at studying two-body and three-body photodisintegration separately using a TPC, these two events should be clearly identified. If one uses $^3$H sample, one can only detect one charged particle of deuteron for two-body breakup and proton for three-body breakup. While if one uses $^3$He sample, one can identify the two-body breakup process by detecting two charged particles of proton and deuteron, and three-body one by detecting two protons. Here is should be mentioned that when two charged particles are detected in the TPC, one can unambiguously trace trajectories of true events using reaction dynamics and thus determine the absolute cross section unambiguously. $^3$H is radioactive, and therefore it is not easy to use it as a target gas.

Characteristic points of the present experimental methods are as follows.

First, since we use a time projection chamber, which contains an active gas target of $^3$He, we can detect very low energy charged particles from the photodisintegration of $^3$He with high efficiency of almost 100%. This is crucial to determine the cross section of the three-body breakup by detecting low energy charged particles, since three particles (ppn) are produced in a random direction with broad energy distribution. So far, the three-body breakup has been studied mostly by detecting neutrons, since the neutrons can be detected rather free from the absorption in a sample or a sample container. However, since neutrons are not produced in the two-body photodisintegration, simultaneous measurements for the two-body and three-body breakup can not be performed.

Second, since the true events due to the photodisintegration of $^3$He originate from the Laser Compton Backscattering (LCS) photon beam axis, one can easily discriminate background signals from the true ones. Most background signals are due to the electrons scattered by the LCS photons, and the energy loss of the electrons is so small that the electron's trajectories are not connected to the LCS photon beam axis.

Third, since the LCS photon beam is used in the present work, quasi-monochromatic $\gamma$-ray can be easily obtained by changing either electron energy or laser photon energy. The quasi-monochromatic $\gamma$-ray is very important in this study, since the measurement is carried out at particular energies, which give the maximum cross section for the two-body and three-body breakup, respectively.

Fourth, the absolute flux of the LCS photon can be measured precisely using $\gamma$-ray detectors. While when one uses the electron bremsstrahlung beam, one has to rely on the theoretical estimation to determine the absolute beam flux.

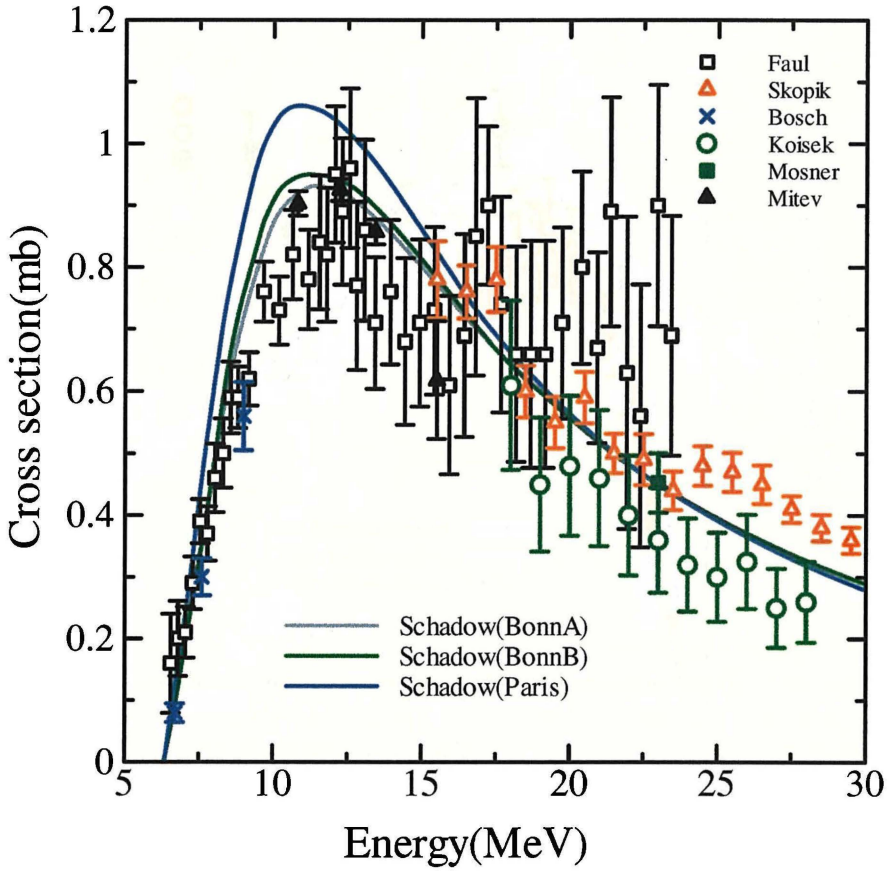


Figure 1.11: Measured and calculated cross sections of the $^3$H($\gamma$,n)d reaction

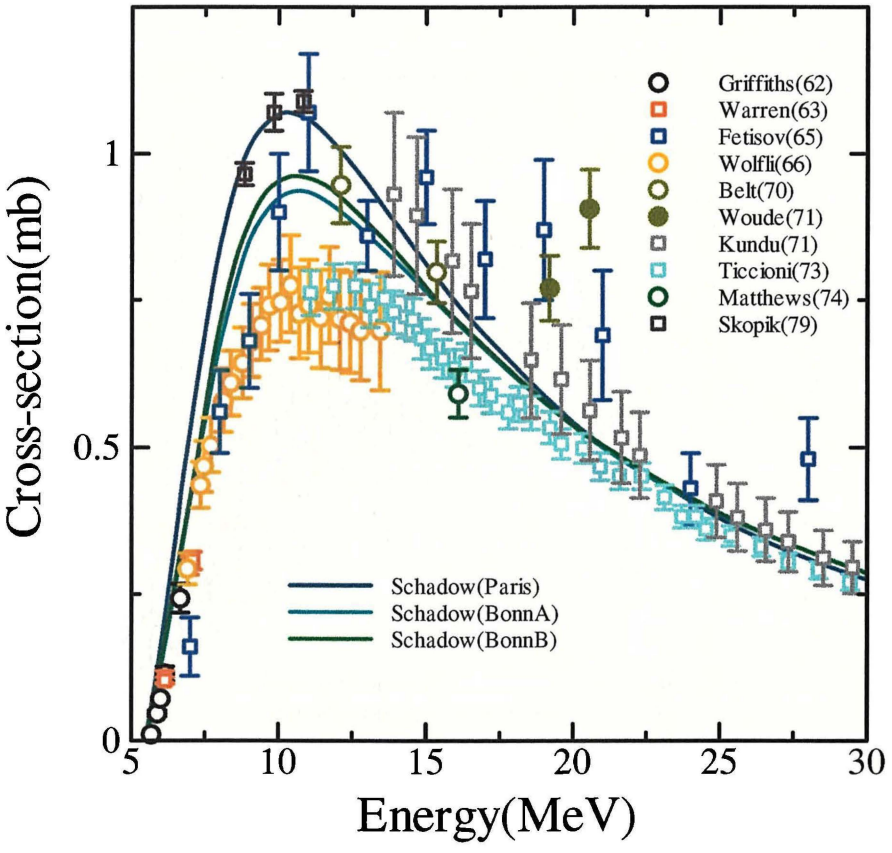


Figure 1.12: Measured and calculated cross sections of the $^3$He($\gamma$,p)d reaction

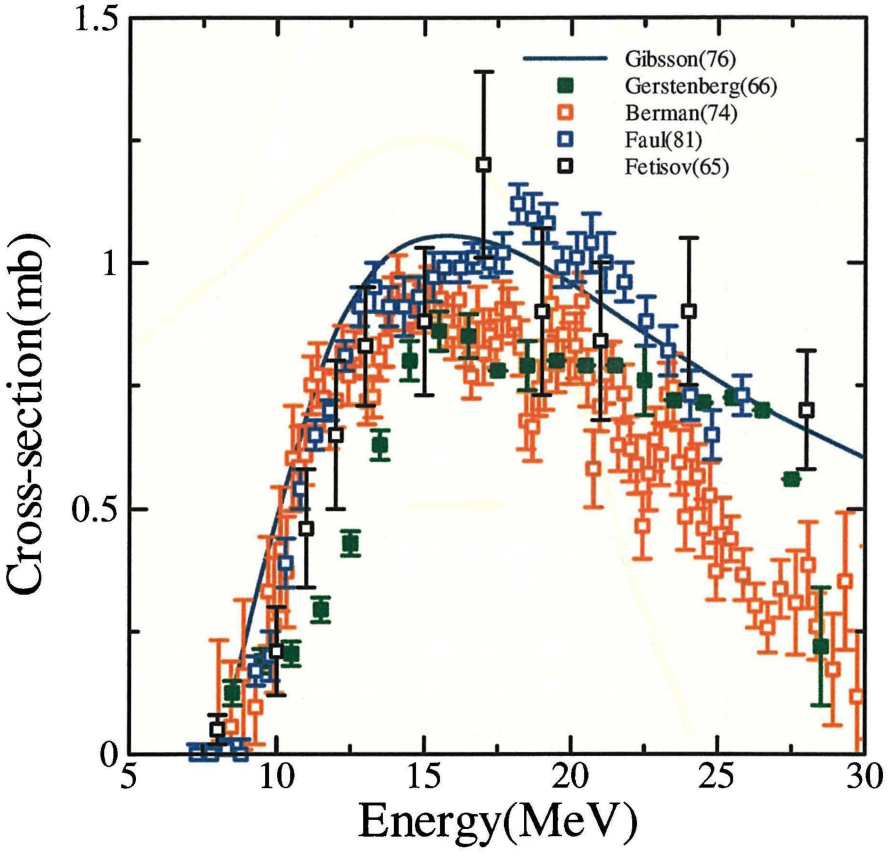


Figure 1.13: Measured and calculated cross sections of the $^3$He($\gamma$,pp)n reaction

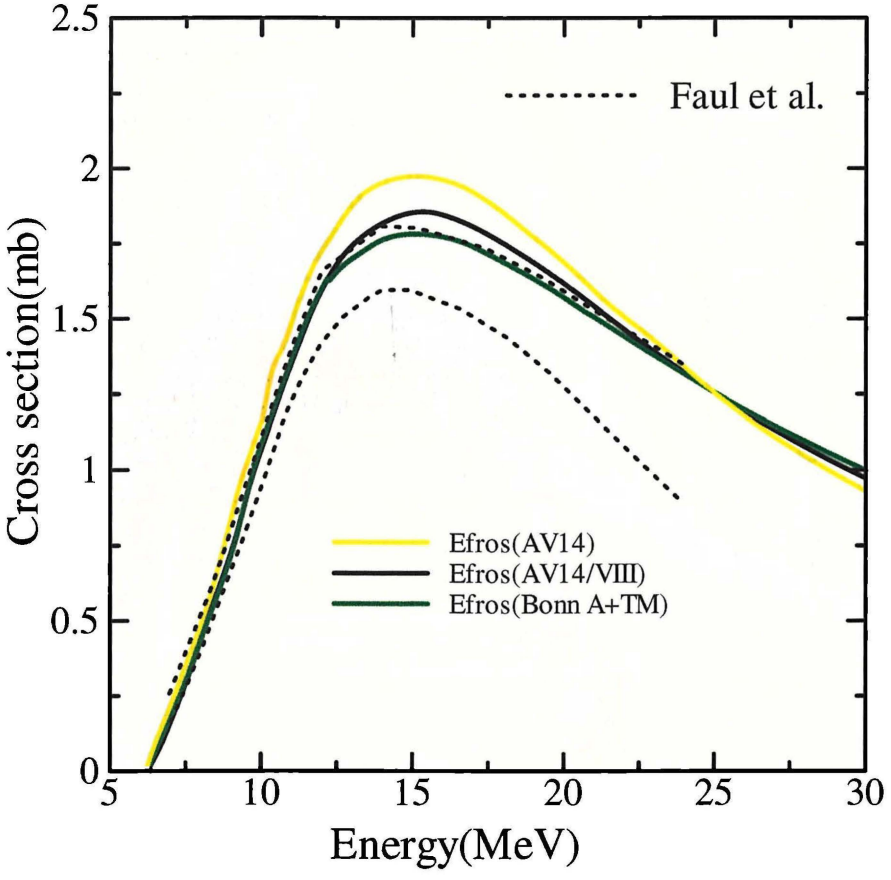


Figure 1.14: Total cross sections of $^3$H photodisintegration experimental result with error range (dotted curves)

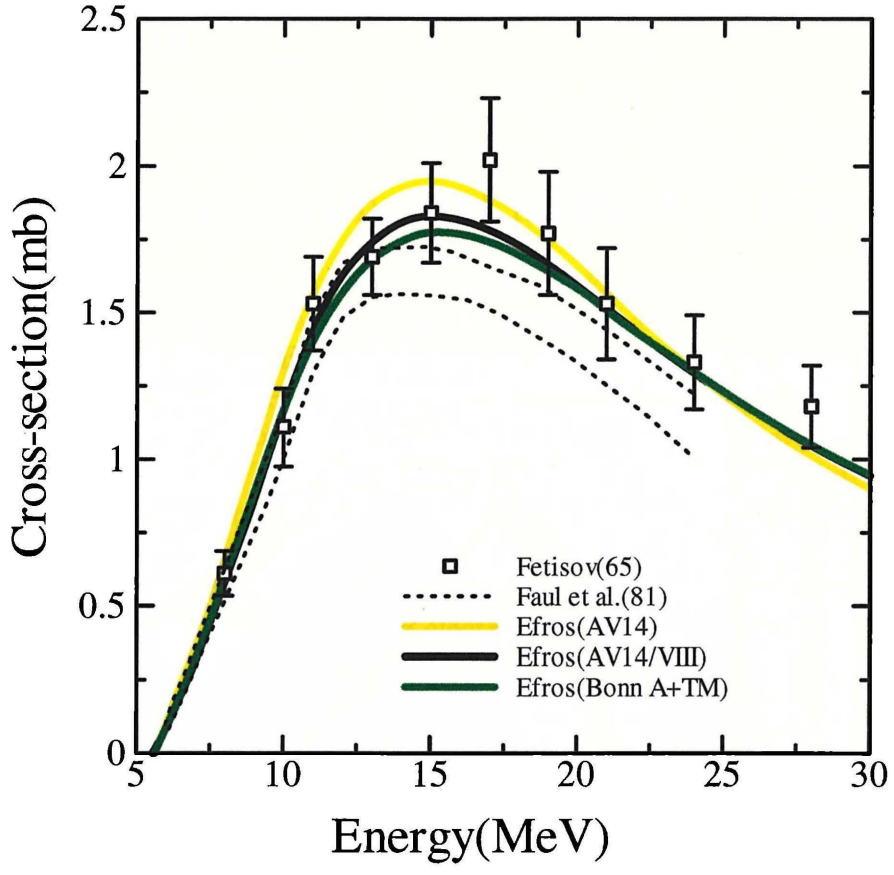


Figure 1.15: Total cross sections of $^3$He photodisintegration experimental result with error range (dotted curves)

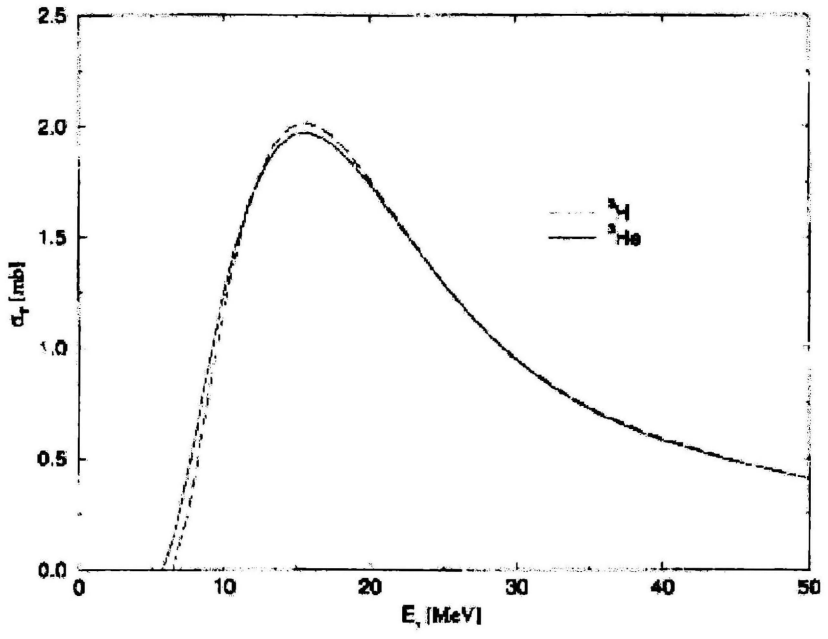


Figure 1.16: Calculated total cross sections of $^3$He and $^3$H
$^3$He(solid curve) and $^3$H(dotted curve)

# 2. Experimental methods and procedures

## 2.1 Outline of experimental methods and procedures

The experiment was performed at $\gamma$-ray energies of $E_{\gamma max}$= 10.5 and 16.5MeV with an electron storage ring TERAS installed at the Electrotechnical Laboratory(ETL). Outline of experimental setup is shown in Figs.2.1 and 2.2. We used Laser-Compton Backscattering (LCS) $\gamma$-rays as the $\gamma$-ray source, which are generated by the Compton backscattering of laser light on relativistic electrons in TERAS. The generated $\gamma$-rays were collimated with a $\gamma$-ray collimator made of lead. The hole diameter and length of the collimator were 2mm and 300 mm, respectively. The time projection chamber (TPC) was installed in the position of 3m of the lower streams of the collimator. The TPC was placed so that the center axis of the TPC was in a straight line with the $\gamma$-ray beam axis. Its adjustment was performed using the synchrotron radiation from the storage electrons. The TPC was filled with mixed gas of $^3$He and methane ($^3$He80%+$CH_4$20%), which serves as an active target. A BGO scintillation counter was used at the lower streams of the TPC for monitoring the incident $\gamma$-ray flux. A plastic scintillator was used at the upper streams of the TPC for monitoring the time when the $\gamma$-ray was generated.

The cross section of $^3$He photodisintegration is given by the following formula.

$$\sigma = \frac{Y}{\epsilon N L \phi} \tag{2.1}$$

Where $\sigma$ is the cross section of $^3$He photodisintegration, $Y$ is the number of detected events, $\varepsilon$ is the detection efficiency of the TPC, $N$ is the number density of target atomic nuclei, $L$ is the effective length of the target, and $\phi$ is the $\gamma$ ray flux, respectively.

Using the TPC we can detect charged particles produced by the photodisintegration of $^3$He with an efficiency of $\sim$100% and thereby construct the trajectories and the pulse heights of the charged particles. The number of events $Y$ was obtained by counting the events of the photodisintegration of $^3$He. The number density of target atomic nuclei $N$ was determined by monitoring the temperature and the pressure in the TPC during the experiment. The $\gamma$-ray flux was determined by analysing the pulse height spectrum of the BGO counter as discussed later. The detection efficiency $\varepsilon$ was determined by fitting the pulse peak spectrum of the events with Monte Carlo simulation. The efficiency $\varepsilon$ depends on the position where the $^3$He photodisintegration occurs in the TPC. The effective length $L$ was determined by studying the position dependence of $\varepsilon$. Therefore it is very important to

determine the position accurately. In this chapter, the experimental methods and procedures are described.

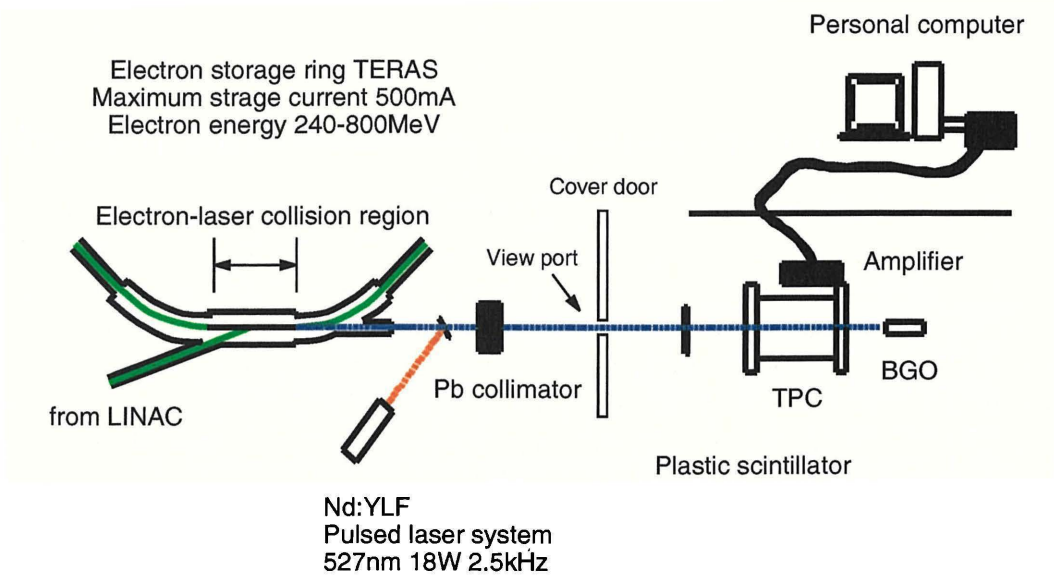


Figure 2.1: Outline of experimental setup

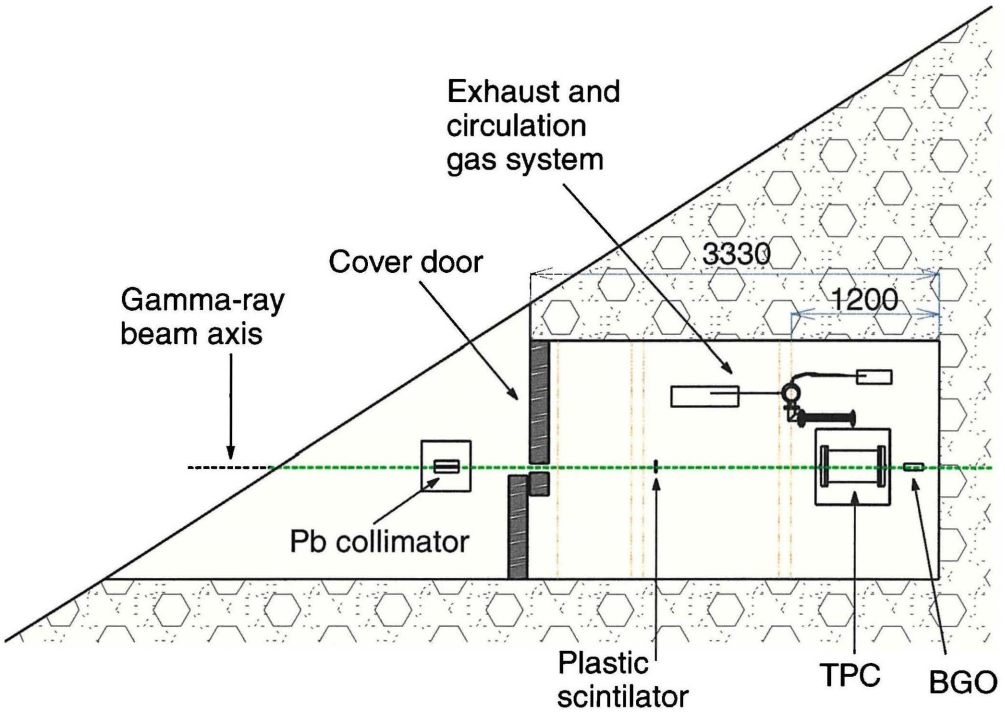


Figure 2.2: Experimental setup around TPC

## 2.2 LCS $\gamma$-ray source

### 2.2.1 Principle

LCS(Laser Compton backward Scattering) $\gamma$-ray is produced in the collision of Compton backward scattering between laser light beam and high energy relativistic electrons. The LCS $\gamma$-ray energy is quasi-monochromatic and the $\gamma$-ray can be linearly and/or circularly polarized[38]. The photon energy $E_\gamma$ in the laboratory system is given as

$$E_\gamma = \frac{\varepsilon_L(1-\beta cos\theta_L)}{1-\beta cos\theta + \frac{\varepsilon_L(1-\beta cos(\theta_L-\theta))}{E_e}} \tag{2.2}$$

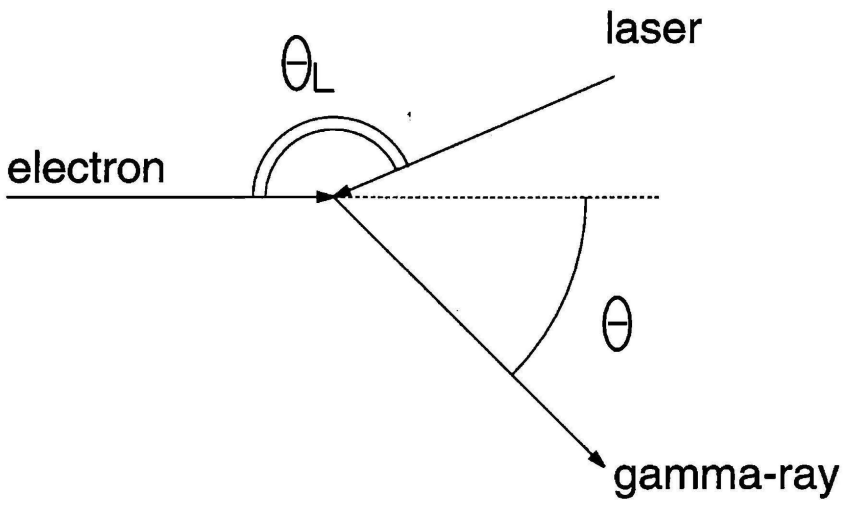


Figure 2.3: Schematic of the laser electron backscattering process

Where $\varepsilon_L$ is the energy of the laser photon, $E_e$ is the energy of the electron, $\theta_L$ and $\theta$ are the angle of the laser beam and the scattered photon in the electron beam direction, respectively and $\beta$ is given as a ratio of the velocity of electron to the velocity of light. The maximum photon energy is obtained at the angle of $\theta_L = \pi$ and $\theta = 0$ and it is approximately written as

$$E_\gamma = \frac{4\gamma^2\varepsilon_L}{1+(\gamma\theta)^2+\frac{4\gamma\varepsilon_L}{m_e c^2}} \tag{2.3}$$

$$\gamma = \frac{E_e}{m_e c^2} \tag{2.4}$$

where $m_e$ is the electron mass. The photon energy spread $\Delta E_\gamma$ is approximately given as

$$\Delta E_\gamma / E_\gamma = \left(\frac{2\Delta E_e}{E_e} + (\gamma \Delta\theta)^4\right)^{1/2} \tag{2.5}$$

$$\Delta\theta = (\theta_e^2 + \theta_c^2)^{1/2} \tag{2.6}$$

where $\Delta E_e$, $\theta_e$ and $\theta_c$ are the energy spread of the electron beam, the electron beam divergence, and a collimator half angle, respectively. The photon yield Y for two non-diverging beams interacting in the length L is given by

$$Y = 2 n_e n_L \sigma L / A c \tau \tag{2.7}$$

where $n_e$ and $n_L$ are total number of electrons and laser photons passing through the length L per unit time, respectively, and $\sigma$ is the cross section. $A$ takes the larger value of the cross section areas between laser beam and electron beam, and $\tau$ is the pulse width of the two beams, and c is the velocity of light.

### 2.2.2 Generating $\gamma$-rays

LCS $\gamma$ rays have been produced in a storage ring TERAS installed at the Electrotechnical Laboratory (ETL)[39][40].

The specification of TERAS is given in Table 2.1.

Table 2.1: The specification of TERAS

| | |
|---|---|
| electron energy | 240-800 MeV |
| Maximum storage current | 300mA |
| energy spread of the electron beam | $6.25 \times 10^{-6}$ |
| degree of the polarization | about 100% |
| Photon yield(photons/sec) | $10^4 - 10^5$ |
| divergence of electron beam | 0.115mrad |

The yield of generated LCS $\gamma$-ray is calculated using eq.(2.7). Since we needed the intense photons of $\sim 10^4$photons/sec, high intensity laser system(Quantronix Nd:YLF Q-switched pulse laser(1-5kHz)) was used in the present experiment.

The performance of the laser system is shown in Table 2.2.

Table 2.2: The specification of LCS $\gamma$-ray in TERAS

| laser | mode | wave length(nm) | average power(W) | maximum $\gamma$-ray energy |
|---|---|---|---|---|
| Nd:YLF Q-switched pulse (1-5kHz) | First | 1053 | 40 | 1-10MeV |
| | Second | 527 | 20 | 2-20MeV |
| | Third | 351 | 3 | 3-30MeV |
| | Fourth | 265 | 0.7 | 4-40MeV |

In order to measure the cross sections of the photodisintegration of $^3$He at the $\gamma$-ray energies of 10.5MeV and 16.5MeV, we used the second harmonic light of the Nd-YLF laser.

A schematic view of the setup to generate the LCS $\gamma$ ray is shown in Fig.2.4.

In order to introduce the generated $\gamma$-rays to the experimental room, the electron orbit must be positioned at the center of the beam tube. The initial orbit, however, is usually not positioned at the center of the beam tube and therefore in order to obtain intense LCS $\gamma$-ray one has to adjust the electron orbit before generating the $\gamma$-ray.

### 2.2.2 Generating $\gamma$-rays

LCS $\gamma$ rays have been produced in a storage ring TERAS installed at the Electrotechnical Laboratory (ETL)[39][40].

The specification of TERAS is given in Table 2.1.

Table 2.1: The specification of TERAS

| | |
|---|---|
| electron energy | 240-800 MeV |
| Maximum storage current | 300mA |
| energy spread of the electron beam | $6.25 \times 10^{-6}$ |
| degree of the polarization | about 100% |
| Photon yield(photons/sec) | $10^4 - 10^5$ |
| divergence of electron beam | 0.115mrad |

The yield of generated LCS $\gamma$-ray is calculated using eq.(2.7). Since we needed the intense photons of $\sim 10^4$photons/sec, high intensity laser system(Quantronix Nd:YLF Q-switched pulse laser(1-5kHz)) was used in the present experiment.

The performance of the laser system is shown in Table 2.2.

Table 2.2: The specification of LCS $\gamma$-ray in TERAS

| laser | mode | wave length(nm) | average power(W) | maximum $\gamma$-ray |
|---|---|---|---|---|
| Nd:YLF Q-switched pulse (1-5kHz) | First | 1053 | 40 | 1-10MeV |
| | Second | 527 | 20 | 2-20MeV |
| | Third | 351 | 3 | 3-30MeV |
| | Fourth | 265 | 0.7 | 4-40MeV |

In order to measure the cross sections of the photodisintegration of $^3$He at the $\gamma$-ray energies of 10.5MeV and 16.5MeV, we used the second harmonic light of the Nd-YLF laser.

A schematic view of the setup to generate the LCS $\gamma$ ray is shown in Fig.2.4.

In order to introduce the generated $\gamma$-rays to the experimental room, the electron orbit must be positioned at the center of the beam tube. The initial orbit, however, is usually not positioned at the center of the beam tube and therefore in order to obtain intense LCS $\gamma$-ray one has to adjust the electron orbit before generating the $\gamma$-ray.

Although the electron orbit changes with the electron energy, one can adjust easily the electron orbit by referring to the previous record, when the energy is close to the used one.

The electron energies for generating 10.5 MeV and 16.5MeV $\gamma$-rays were 545MeV and 685MeV, respectively. Since these electron energies were not used to generate the LCS $\gamma$-rays before, we had to make the adjustment of the electron orbit as discussed below. The currents of steering magnets of TERAS were adjusted so that the electron orbit in the straight-line section of TERAS was in a straight line with a view port in the experimental room as shows in Fig.2.1. The position of the electron beam was determined using the synchrotron orbital radiation. After this rough adjustment we did fine tuning by adjusting all steering magnets. Thus the local orbit may not change greatly and the electron beam may not fall.

In the present experiment we have newly constructed the optical system to produce the LCS $\gamma$-ray as shown in Fig.2.4. This system was constructed so as to produce the LCS $\gamma$-ray as intense as possible by making the spot size of the laser beam about 3mm in the interaction region of the length L. The laser system we used (Quantronx Nd:YLF) was simultaneously oscillated in several modes, and each mode had a different focal distance, and the laser divergence was large (about 5mrad). Hence we placed the lens (L1) just after the laser system to reduce the laser divergence and make the parallel beam. We obtained the proper laser spot size of about 8mm on the concave mirror (M2) in stead of 2cm without L1.

Finally, the number of photons thus obtained was of $10^4 photons/sec$.

The procedure of generating $\gamma$-rays is as follows.

1. In order to obtain the intense LCS-$\gamma$ ray, we adjusted the the positions of the electron beam and the laser beam so that the longer length of the colliding region could be obtained.

2. The number of generated photons was monitored with a plastic scintillator to make the fine tuning of the laser orbit and the electron orbit.

During the experiment, we always monitored the operation status of TERAS to keep the LCS $\gamma$-ray as intense as possible.

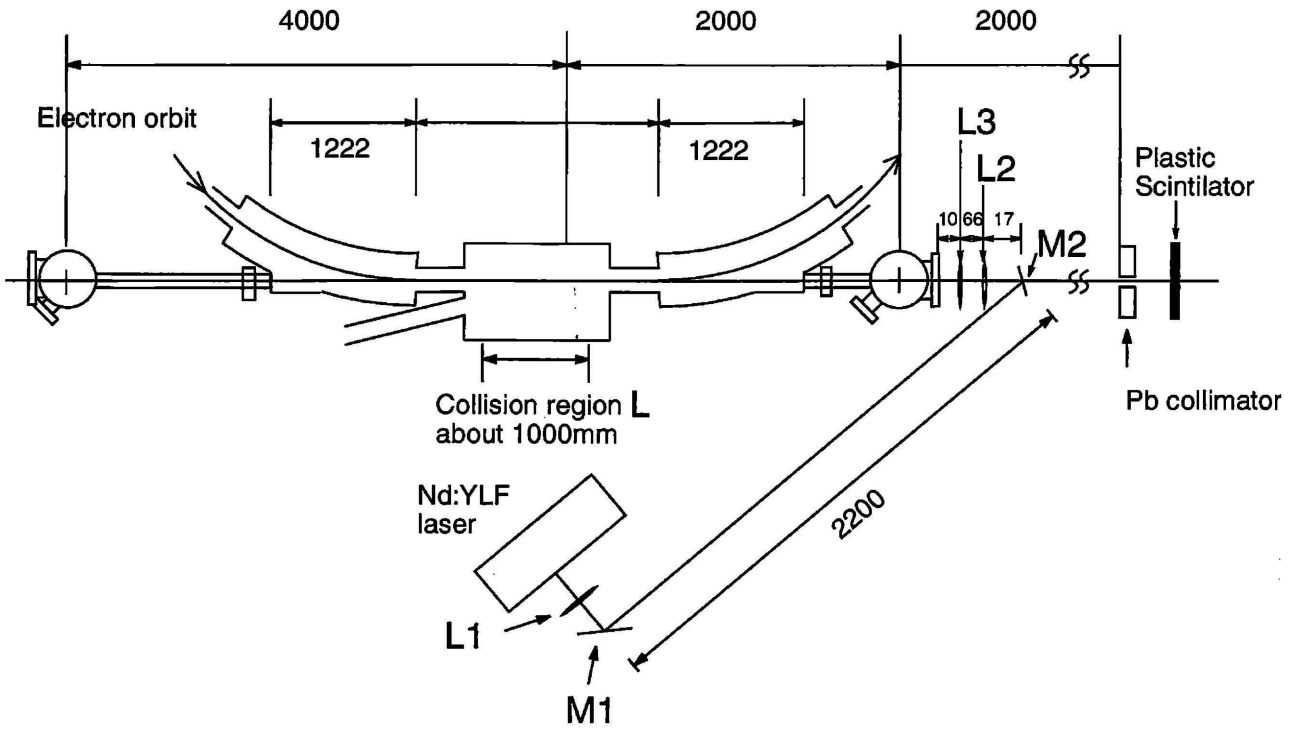


Figure 2.4: Experimental setup to produce the laser Compton backscattering $\gamma$-ray
L1:lens f=1000mm, L2:lens f=5000mm, L3:lens f=2500mm,
M1:flat mirror, M2:concave mirror r=10m

## 2.3 $\gamma$-ray monitor

In the high accurate measurement of the photodisintegration cross section, it is very important to determine accurately the absolute intensities of the incident $\gamma$- rays. In the present experiment since the energies of the $\gamma$-rays are as high as 10.5MeV and 16.5MeV, a $\gamma$-ray detector with a small radiation length is needed to measure the intensity of the LCS-$\gamma$ rays accurately. Therefore we used a BGO scintillation counter with a diameter of 2inch and length of 6in. The absolute intensities of the $\gamma$-rays were determined by analysing the pulse height spectra of the BGO counter. The detail of the analysis is described in Chapter 3. In addition, we used a plastic scintillation counter for obtaining the timing signal, which gives the arrival time of the $\gamma$-ray pulse and is used as the start signal in measuring the drift time of the TPC. The experimental setup to measure the incident LCS $\gamma$-ray is shown in Fig.2.5.

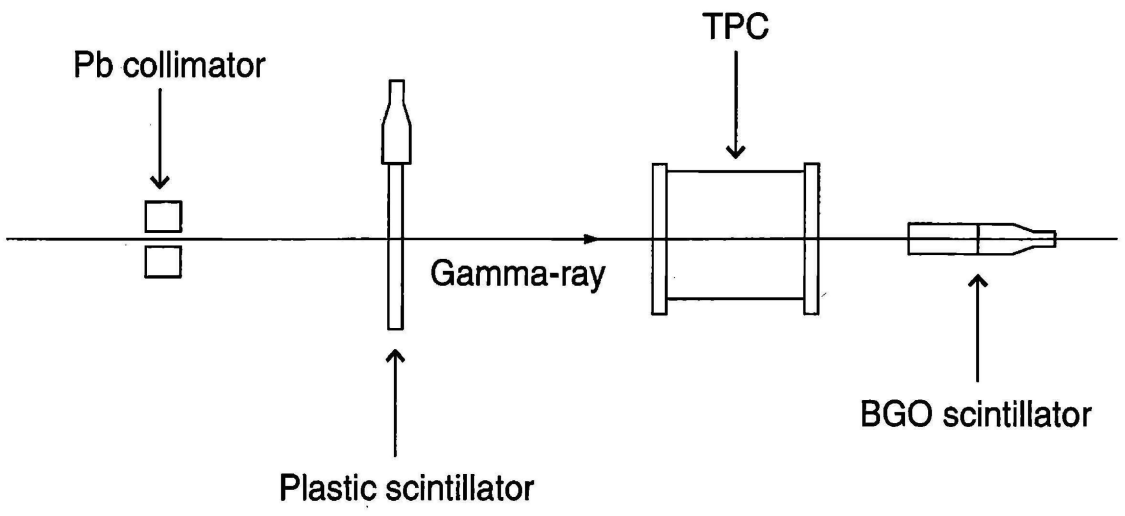


Figure 2.5: Setup of measurement

## 2.4 Operation principle of the TPC

The TPC is a type of the drift chamber, and it has an advantage in the detection of the tracks of the charged particles emitted in the nuclear reactions. The operational principle is as follows.

### 2.4.1 Outline of operation principle

The TPC consists of two sections of the drift region and the electron multiplication region as shown in Fig.2.6. Here the TPC is filled with mixed gas of $^3$He 80% and $CH_4$ 20%.

The operation principle of the TPC is described as follows. When a fast charged particle passes through the drift region,it ionizes or excites atomic or molecular gases and produces ionized electrons along its track. The ionized electrons form an electron cloud, and they are drifted to the multiplication region along the uniform electric field in the drift region. In the multiplication region, drifted electrons are multiplied via the avalanche process in strong electric field near the anode wires. The signals of the avalanche are picked up with the anode wires and the cathode wires. The directions of the wires in two cathode planes are perpendicular to each other, and therefore we can measure the positions of the drift electrons in the x-y plane, where the x- and y-directions are defined as shown in Fig.2.6. The position of the track in the z-direction is obtained from the drift time of the ionized electrons. Here, the drift time is measured as the time difference between the arrival time of the drift electrons to the anode wires and the start time given by an external trigger signal. The currents of the anode signals are measured to determine the energy loss of a particle in the drift region.

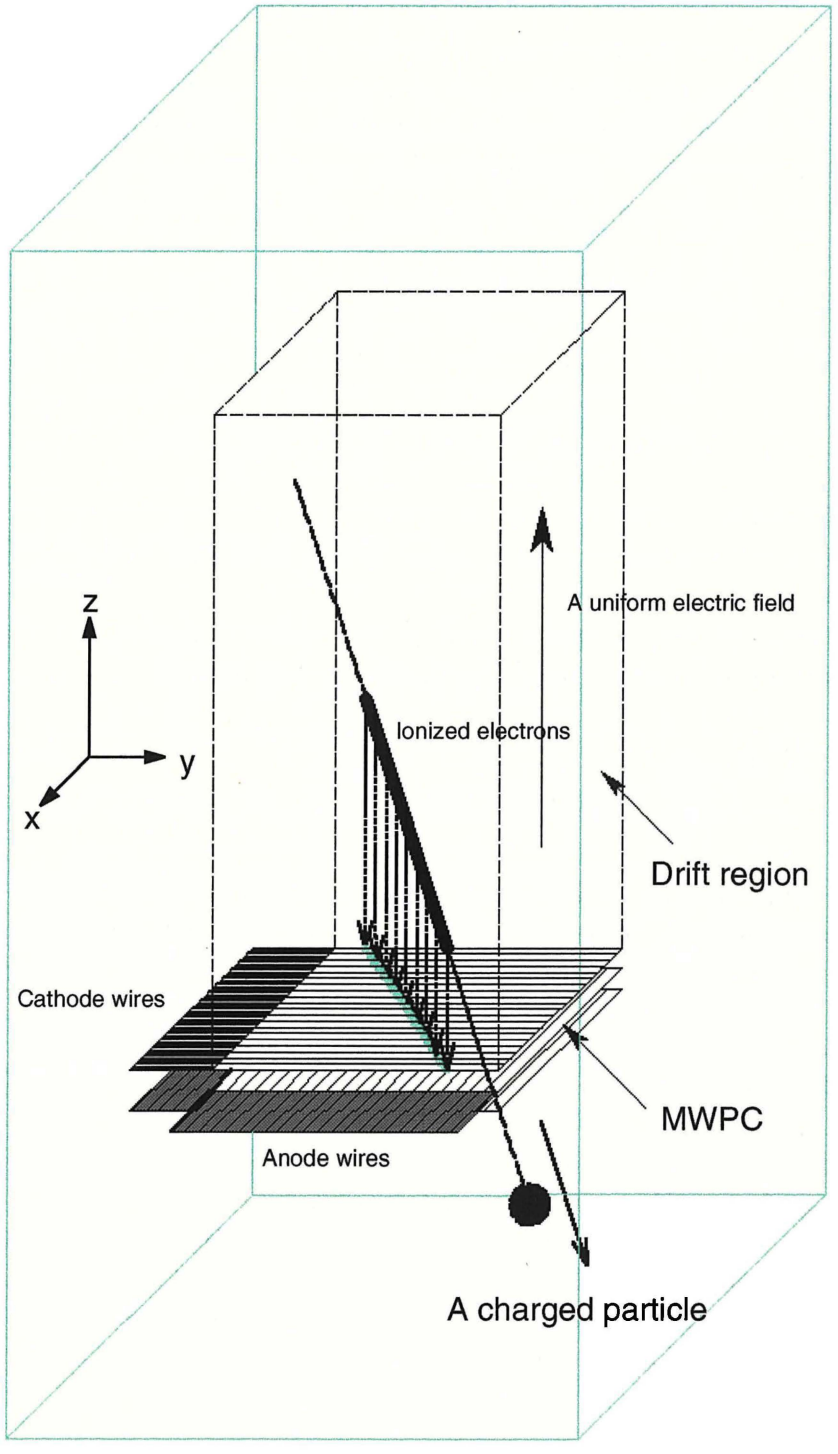


Figure 2.6: A schematic diagram of the TPC

### 2.4.2 The motion of a charged particle in gases

The motion of a charged particle with a few MeV in gas is as follows. The fast charged particle with this energy gives its kinetic energy to atomic or molecular gas with the electromagnetic interaction. And along the particle track electrons are produced by the ionization of the gas. The average energy needed in order to produce one electron by the ionization is called a w value. The w values have been measured for many kind of gasses and typical values are given in Table.2.3[41]. They are a few ten eV and thus the energy loss of a few hundred keV

Table 2.3: The measured w values for typical gases

| *gases* | $H_2$ | $He$ | $CH_4$ | $CO_2$ |
|---|---|---|---|---|
| $W(eV)$ | 37 | 41 | 28 | 33 |

can produce $10^4$ electrons.

Next, we discuss the energy loss of a charged particle by the ionization of gasses in several region of the its kinetic energy.

When the energy of the charged particle per nucleon is larger than 1 MeV, the measured energy losses are reproduced by the following Bethe formula[42],

$$\frac{dE}{dx}[MeV/m] = \frac{4\pi e^4 Z_1^2 Z_2}{mv^2}\left(ln(\frac{2mv^2}{I}) - ln(1-\beta^2) - \beta^2\frac{C}{Z_2}\right) \tag{2.8}$$

$$\beta = v/c \tag{2.9}$$

where $I$ is the ionization potential, and $m, Z_1, Z_2, v, c$ are the mass of an incident particle, the charge of an incident particle, the charge of a target particle, the velocity of an incident particle and the velocity of light, respectively and $C/Z_2$ is the number called the shell correction.

When the energy of the charged particle per nucleon is smaller than 10keV, Thomas-Fermi model shows that the energy loss is proportional to $v$ and the calculated values agree with measured energy losses[41].

However when the energy is between 10keV and 1MeV, there is no theoretical explanation of the energy losses. Hence the energy losses are reproduced by using the experimental formula. Zeiglar *et al.* give the functional form of this formula together with many parameters as discussed below for hydrogen and helium gasses[43]. Here $S$ is the energy loss $[eV/(10^{15}atoms/cm^2)]$ ,and E is the kinetic energy per nucleon [keV/amu] for hydrogen and the kinetic energy [MeV] for helium.

In the case of hydrogen,
1-10keV

$$S = A_1 E^{1/2} \tag{2.10}$$

10-1000keV

$$\begin{aligned} S^{-1} &= (S_{low})^{-1} + (S_{high})^{-1} && (2.11) \\ S_{low} &= A_2 E^{0.45} && (2.12) \\ S_{high} &= A_3 E ln(1 + \frac{A_4}{E} + A_5 E) && (2.13) \end{aligned}$$

1000-100000keV

$$S = \frac{A_6}{\beta^2}(ln\frac{A_7\beta^2}{1-\beta^2} - \beta^2 - \sum_{i=0}^{4} A_{i+8}(lnE)^i) \tag{2.14}$$

And parameters of $A_x$ are given in Table 2.4.
In the case of helium,
1-10MeV

$$\begin{aligned} S^{-1} &= (S_{low})^{-1} + (S_{high})^{-1} && (2.15) \\ S_{low} &= A_1 E^{A_2} && (2.16) \\ S_{high} &= \frac{A_3}{E/1000} ln(1 + \frac{A_4}{E/1000} + \frac{A_5 E}{1000}) && (2.17) \end{aligned}$$

10MeV-

$$\begin{aligned} S &= exp(A_6 + A_7 EE + A_8 EE^2 + A_9 EE^3) && (2.18) \\ EE &= ln(1/E) && (2.19) \end{aligned}$$

And parameters of $A_x$ are given in Table 2.5.

Table 2.4: Parameters for hydrogen

| | $A_1$ | $A_2$ | $A_3$ | $A_4$ | $A_5$ | $A_6$ |
|---|---|---|---|---|---|---|
| $H$ | 1.262 | 1.44 | 242.6 | $1.2 \times 10^4$ | 0.1159 | $5.099 \times 10^{-4}$ |
| $He$ | 1.229 | 1.397 | 484.5 | 587.3 | 0.05225 | 0.00102 |
| $C$ | 2.631 | 2.989 | 1445 | 957.2 | 0.02819 | 0.003059 |
| | $A_7$ | $A_8$ | $A_9$ | $A_{10}$ | $A_{11}$ | $A_{12}$ |
| $H$ | $5.436 \times 10^4$ | $-5.052$ | 2.049 | $-0.3044$ | 0.01966 | $-4.659 \times 10^{-4}$ |
| $He$ | $2.451 \times 10^4$ | $-2.158$ | 0.8278 | $-0.1172$ | 0.007259 | $-1.66 \times 10^{-4}$ |
| $C$ | $1.322 \times 10^4$ | $-4.38$ | 2.044 | $-0.3283$ | 0.02221 | $-5.417 \times 10^{-4}$ |

Table 2.5: Parameters for helium

| | $A_1$ | $A_2$ | $A_3$ | $A_4$ | $A_5$ | $A_6$ |
|---|---|---|---|---|---|---|
| $H$ | 0.39 | 0.63 | 4.17 | 85.55 | 19.55 | 2.371 |
| $He$ | 0.58 | 0.59 | 6.3 | 130 | 44.07 | 2.809 |
| $C$ | 3.47 | 0.4485 | 22.37 | 36.41 | 7.993 | 3.588 |
| | $A_7$ | $A_8$ | $A_9$ | | | |
| $H$ | 0.5462 | $-0.07932$ | $-0.006853$ | | | |
| $He$ | 0.4847 | $-0.08756$ | $-0.007281$ | | | |
| $C$ | 0.3921 | $-0.09935$ | $-0.007804$ | | | |

### 2.4.3 The electron motion in the electric field

Electrons, which are produced by the ionization of atomic or molecular gas, drift to the direction of the multi-wire proportional counter (MWPC) in the uniform electric field. These electrons are in thermal equilibrium by many collisions with gas, and the drift velocity of these electrons is sufficiently slower than a velocity of thermal motion. The drift velocity of electrons is given by a balance between the energy loss of the electrons due to the collisions with gas and the energy gain due to the acceleration by the electric field. The velocity depends on a kind of gas, the gas pressure gradient and the electric field gradient.

If the operational gas contains an impurity gas with high-electro-negativity, electrons are captured by the molecule of the impurity gas. Then the number of the electrons detected by MWPC decreases and therefore both the resolution and the detection efficiency of the TPC become poor. Although the electron capture rate per one collision by an impurity gas of oxygen or water in a standard state ($0^oC$,$1atm$) is about $10^{-5}$, since the number of times of collisions per unit time is about $10^{11}$ times, the small mixing of these impurities cannot be disregarded when the drift time is long. The origins of these impurity gasses are due to the leakage of the TPC and/or the outgas from the surface of the TPC. Therefore we have paid special care to construct the vacuum-tight TPC. Usually rare gas, such as He and Ar, and non-polarity molecule like $CO_2$ and methane, are used as an operational gas of the TPC. In order to operate the TPC stably by reducing a fraction of the possible impurity gas the operational gas is usually flowed. It should be stressed again that one has to make efforts to reduce the impurities, such as oxygen and water, for the stable and reliable operation of the TPC, which is crucial for the high precision experiment.

### 2.4.4 The amplification of electrons in the strong electric field

The drifted electrons are amplified by electrons avalanche process in the strong electric field (a few kV/cm) around the anode wires of the MWPC and are finally detected as the electric signals. Between each collisions (the mean free path $\lambda$), electrons get the kinetic energy $eE\lambda$, where e is an electron charge and E is the magnitude of the electric field. When this energy is larger than the ionization potential of used gas, electrons avalanches occur. When $n$ electrons move to the anode direction from a position $x$ to a position $x + dx$, the number of drifted electrons are written as

$$dn = n\alpha dx \tag{2.20}$$

Where $\alpha$ is called the Townsend first ionization coefficient and $\alpha^{-1}$ is the mean free path until gas is ionized. This coefficient depends on the electric field and changes with the distance from an anode wire. The amplification factor M of the electron is written as,

$$M = exp\Big(\int_{x_1}^{x_2} \alpha(x)dx\Big) \tag{2.21}$$

In the region of a certain strength of electric-field and gas pressure, M is constant and does not depend on the amount of electric charges produced by the primary ionization. In this region, output pulse height is proportional to the initial charge of electrons which are finally detected by the MWPC. Therefore the pulse height obtained from a wire is proportional to the energy which the charged particle gave to the wire. Generally, this region is called as a proportional region. In order to measure the energy of a charged particle, the electrical potential applied to the anode wires needs to be in the proportional region. Generally, M is between $10^4$ to $10^6$.

In addition to the ionization of gases, electrons emit photons when the excited atomic or molecular gas deexcites. When electrons amplification by emitting photons occurs in the wide region of the MWPC, the position resolution of MWPC becomes worse and the electric discharge occurs in the whole region of the detector. Consequently, the operation of the detector becomes unstable. Because organic gases and diatomic molecular gases absorb these photons in their vibrational modes, these gases are added in the operational gas.

### 2.4.5 Signal at MWPC

As shown in Fig.2.6, the MWPC has many wires, and it has the capacitor type structure (capacity C), where each wire of the anode plane is placed between two cathode planes. Electrons generated by the electron multiplication process are carried immediately to an anode wire ($\sim 1cm/\mu sec$). While the positive ions (total charge Q) are carried to the cathode plane slowly since their drift velocity is slower than electrons. And the electric voltage signal is generated in the anode plane by the movement of charge Q. The typical rise time of the signal is $10^{-8} - 10^{-9} sec$ for electron pulse and $10^{-3} sec$ for the positive ion pulse. In the TPC, in order to measure the drift time of electrons in a drift region, the rise time of the signal must be faster than the electron drift time. Therefore the resistance R which connects anode wires to a high-voltage power supply must be chosen to satisfy the conditions, $RC < 10^{-3} sec$.

When electron avalanche occurs at a certain point near a particular anode wire, the signal is induced on the anode wire and also on the cathode wire, which corresponds to the point. As mentioned before, two cathode wires are stretched so that the wires may be orthogonal each other. Hence we can make the projection of the charged particle trajectory onto the cathode wire plane (xy plane) using these two cathode signals. When the electrons produced by a charged particle has a finite spread $\Delta z$ in the drift direction (z direction) as shown in Fig.2.7, these electrons arrive the MWPC region with a finite time spread. Hence the cathode signals induced by these electrons have a finite time spread $\Delta t$, which can be measured by a time to digital converter (TDC). Since we can get the drift velocity $V_d$ of electrons in the TPC as discussed later, we can calculate the spread $\Delta z$ as $\Delta z = V_d \times \Delta t$. In this way we can obtain the three-dimensional trajectory of the charged particle.

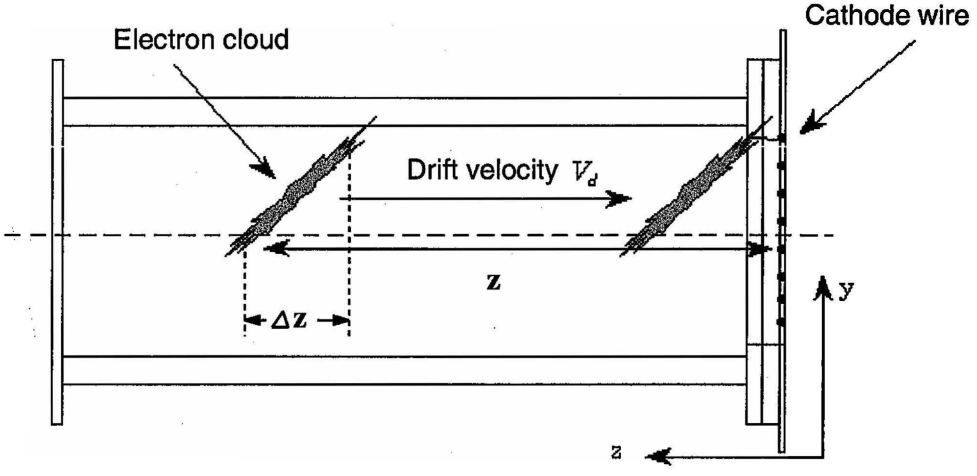


Figure 2.7: A schematic view of the drift region of the TPC

## 2.5 Design of our TPC

A schematic view of our TPC is displayed in Fig.2.8. The TPC consists of three parts of container, drift region and MWPC.

Our TPC was developed for studying photodisintegration of a nucleus, such as D, $^3$He and $^4$He, using laser Compton backscattering photons. It is well known that if high electronegative impurities, such as $H_2O$ and $O_2$, are mixed into a TPC, it is quite difficult to operate the TPC stably. Therefore when a TPC is used in an experiment, a gas flow system is installed to make the stable operation by reducing the concentration of impurities. In the present case, however, target gas of an enriched $^3$H is very expensive, and therefore we can not make our experiment using a gas flow system. Hence we made efforts to construct a vacuum-tight TPC container. The amount of the outgas of all the materials, which were used inside the TPC container, were carefully checked and the materials with small outgas were used. Consequently, we could operate the TPC for about 10 days without introducing any fresh operational gas.

The size of the drift region of the TPC is $60 \times 60mm^2$ in area and 250mm in length as shown in Fig. 2.9. In order to drift the ionized electrons to the MWPC region it is necessary to make the uniform electric field in the drift region. Hence field wires were stretched in the drift region as shown in Fig. 2.9. Each wires were connected though a resistor. As a drift distance becomes long, slight distortion of the electric field influences the accurate determination of the event position. In order to maintain the accuracy as high as possible, the drift region was determined to be 250mm in length. The result of the electric-field calculation is shown in Fig.2.10. In data analysis we considered the distortion of the electric field near the end of the drift region as discussed later.

The MWPC consists of three planes of one anode and two cathodes. The distance between the anode plane and two cathode plane is 2mm. Each plane has 20 wires and the distance between each wires is 2mm. Wires are stretched so that the wires of the two cathode planes may be orthogonal each other. Therefore the spatial resolutions for both x and y coordinates are 2mm. Since each anode wire has the same characteristics as a proportional counter, the MWPC can be considered as the detector with 30 proportional counters.

In order to measure the drift velocity and make the energy calibration of the TPC we put the $\alpha$-ray source of $^{241}$Am inside the TPC. During the experiment of the $^3$He photodisintegration, the $\alpha$-ray source was masked by closing a shutter.

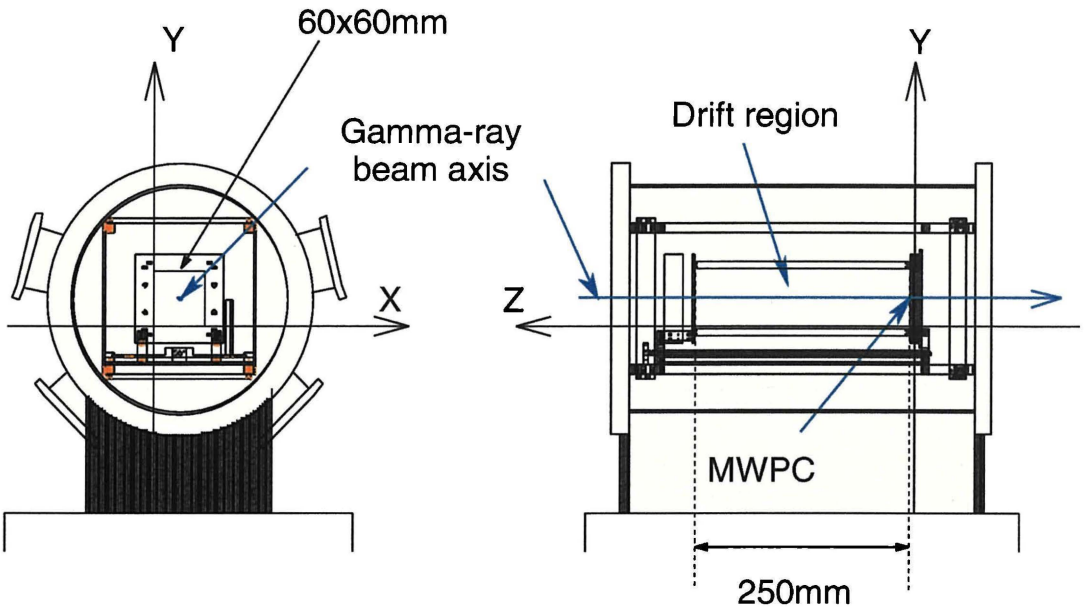


Figure 2.8: A schematic view of our TPC

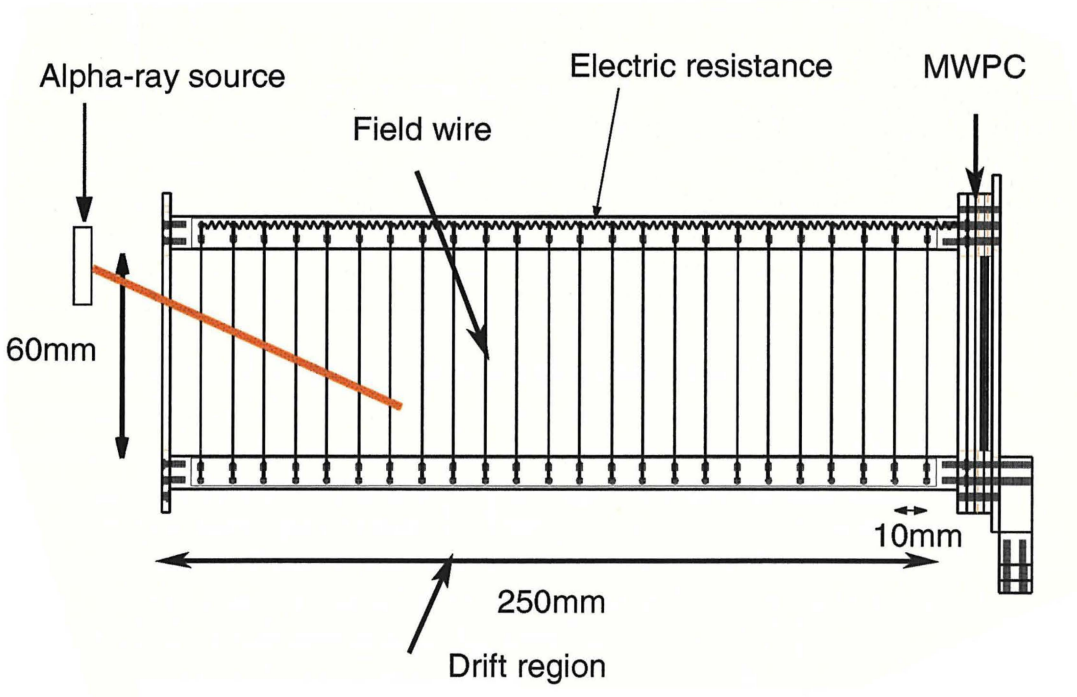


Figure 2.9: The side view of the drift region
A red line expresses the $\alpha$-ray track.

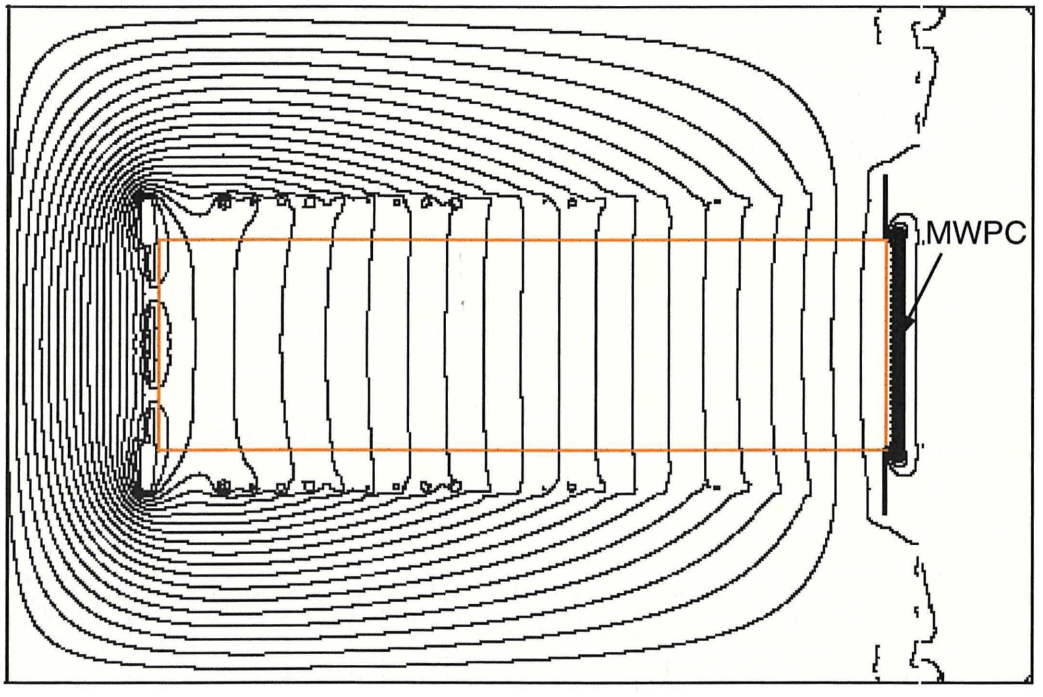


Figure 2.10: Calculated electric field in the drift region of the TPC
The drift region is an area surrounded by a red line.

## 2.6 Target gas

In the present experiment target gas of $^3$He serves also as an operational gas. In order to make the stable operation of the TPC a mixed gas of $^3$He and methane was used.

As discussed before it is quite important for the stable operation of the TPC to use the impurity free gas as a target gas and an operational gas. Therefore we have checked the amount of possible impurities of the commercial $^3$He gas, which got from a company, using a mass analyzer. It was found that the $^3$He gas contained 0.007% of $H_2O$ and 0.3% of oxygen. Hence in order to reduce these impurities less than 10 ppb of total amount of $^3$He we purified the $^3$He gas using the high purity filter (Nippon Sanso Corp. PURIFILTER). It was essential to purify the commercial $^3$He gas for the stable operation of the TPC.

Target gas pressure of 800 Torr was determined by considering following things. In order to increase the true events and the detection efficiency of the TPC it is necessary to increase the gas pressure. Here when the gas pressure is high, the energy loss in the TPC becomes large and therefore the pulse height becomes high. Hence the detection efficiency of the TPC becomes high. While one can not increase the gas pressure so high, since the present TPC has not been constructed for the higher pressure operation above an atmospheric pressure. The flight length, the energy losses of a proton and a deuteron from the two-body breakup of the photodisintegration of $^3$He at the photon energy of 10.5 and 16.5 MeV ($^3$He:$CH_4$ is 80%:20%, pressure of 800 torr, temperature of 22.3°C) were calculated using the formula given by Ziegler (Section 2.4.2) and they are shown in Table 2.6. Here it should be noted that since the charged particles can not be stopped within the drift region, these particles have various values of energy loss depending on the angle emitted from the reaction point. Therefore special care must be paid for obtaining the efficiency of the TPC.

Table 2.6: Flight length and energy loss of proton and deuteron

| | $^3$He($\gamma$,p)d | | $^3$He($\gamma$,pp)n | |
|---|---|---|---|---|
| incident $\gamma$-ray energy(MeV) | 10.5 | 16.5 | 10.5 | 16.5 |
| proton kinematic energy $E_p$(MeV) | 3.3 | 7.3 | 0.93 | 2.9 |
| proton flight length $l_p$(cm) | 46 | 187 | 53 | 36 |
| energy loss ($\frac{dE}{dl}$) at $E_p$(MeV/cm) | 0.037 | 0.019 | 0.096 | 0.041 |
| deuteron kinematic energy $E_d$(MeV) | 1.7 | 3.7 | | |
| deuteron flight length $l_d$(cm) | 9.0 | 33 | | |
| energy loss ($\frac{dE}{dl}$) at $E_d$(MeV/cm) | 0.11 | 0.059 | | |

(*) We assume two protons and a neutron have same energy for the $^3$He($\gamma$,pp)n.

An enriched $^3$He gas is very expensive, and therefore we made special efforts to operate the TPC stably without exchanging the $^3$He gas for a long time as discussed below. The beam time we could get for the present works was about 3 days per month. Therefore in order to avoid deterioration of the target gas caused by out gas or leakage of the TPC, it is desirable to collect the target gas from the TPC after every beam time, and to purify the target gas with the above-mentioned filter further. However we loose the target gas by about 20% in collecting the $^3$He gas. Hence we made efforts to construct the leakage-free and outgas-free TPC and thereby to operate the TPC stably. The long term stability of the TPC was checked as follows. After checking very few leakage rate of the TPC, the enriched $^3$He gas was introduced into the TPC together with methane gas. Then after 20 days later the operation of the TPC was studied using the $\alpha$-rays source. The pulse height spectrum of the $\alpha$-ray is shown in Fig.2.11, indicating that the TPC keeps the good operation condition for at least 20 days.

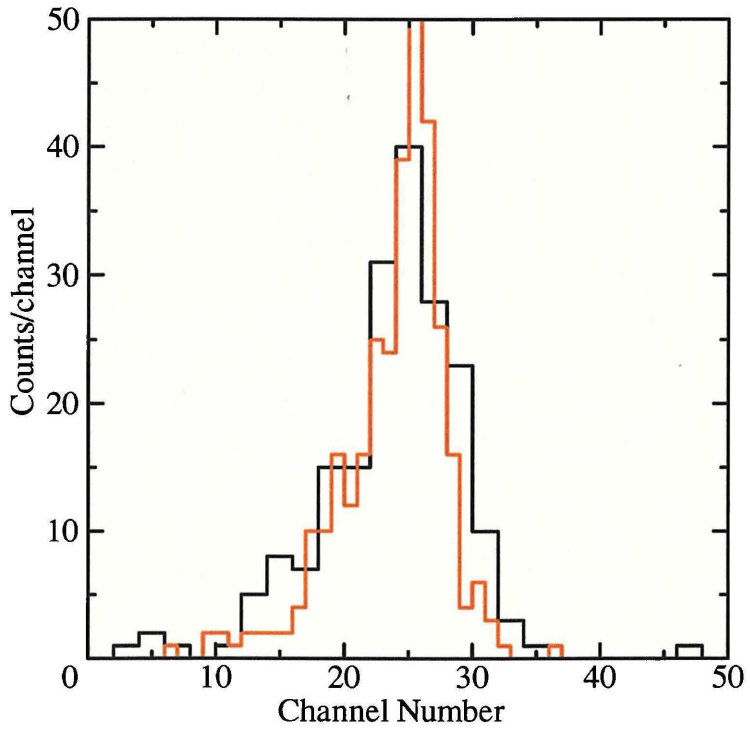


Figure 2.11: Pulse height spectrum of the $\alpha$-ray
red:just after filling the $^3$He gas in the TPC
black:20 days later

## 2.7 Electronics and data acquisition

The schematic diagram of data acquisition system is shown in Fig.2.12. Since the output signals form the present TPC were very low with various noise components, we used the home-made low noise amplifier [44] for the signal processing from the anode wires and cathode wires. Linear signals from the preamplifiers were discriminated by comparators (MAX9690).

The discriminated signals provide the stop signals for LeCroy TDC (2277). A common start signal of TDC is produced from the output of the laser clock of the pulsed laser (Nd:YLF). This TDC can record the time of leading edge and the time of trailing edge for one signal. The time difference between these two edges is larger as the pulse height is higher. Hence the time difference is equivalent to the magnitude of the energy loss of the detected particle in the drift region. The wave forms of the signals from the anode wires are measured with RINNEI flash ADC(RPC-081). Data from the CAMAC modules are acquired by a personal computer (PC/AT,Linux version 2.0.34) via a Kinetic Systems bus interface (K2917) and a Kinetic Systems parallel bus crate controller (K3922). These data are recorded on a hard disk drive in a list mode. The timing chart of data acquisition is shown in Fig.2.13. The signal of BGO is recorded by a peak sensitive ADC.

Here it should be mentioned that two modules of K2917 and K3922 are old enough and therefore it is difficult to obtain new ones, when they are damaged. Therefore a new software system for data acquisition using TOYO-TECHNICA Corp. CC/7000, which is newer CAMAC crate controller, was developed so that the measurement could be continued even when K2917 and K3922 break down.

## 2.8 Noise reduction

One of the essential points to use the TPC for the present experiment of the $^3$He photodisintegration is it's capability to detect the charged particles with small energy loss. Hence it is crucial to have an electric noise level of the TPC as low as possible. Actually, in order to obtain the high detection efficiency the discrimination level of about 30mV is required. While we noticed the large electric noise of about 50mV with a repetition rate of 10MHz. Hence we made efforts to eliminate the noise as discussed below.

When we searched for the place where the electrical noise came from, we found the noise in many places, such as whole areas of the TERAS ring, TERAS control room, the computer room and LINAC room. The noise existed independent of the experimental conditions of the apparatus of another group and the power condition of the TERAS. However, the noise was not observed in the power source of the hot-water-supply room in the lab. Then, it

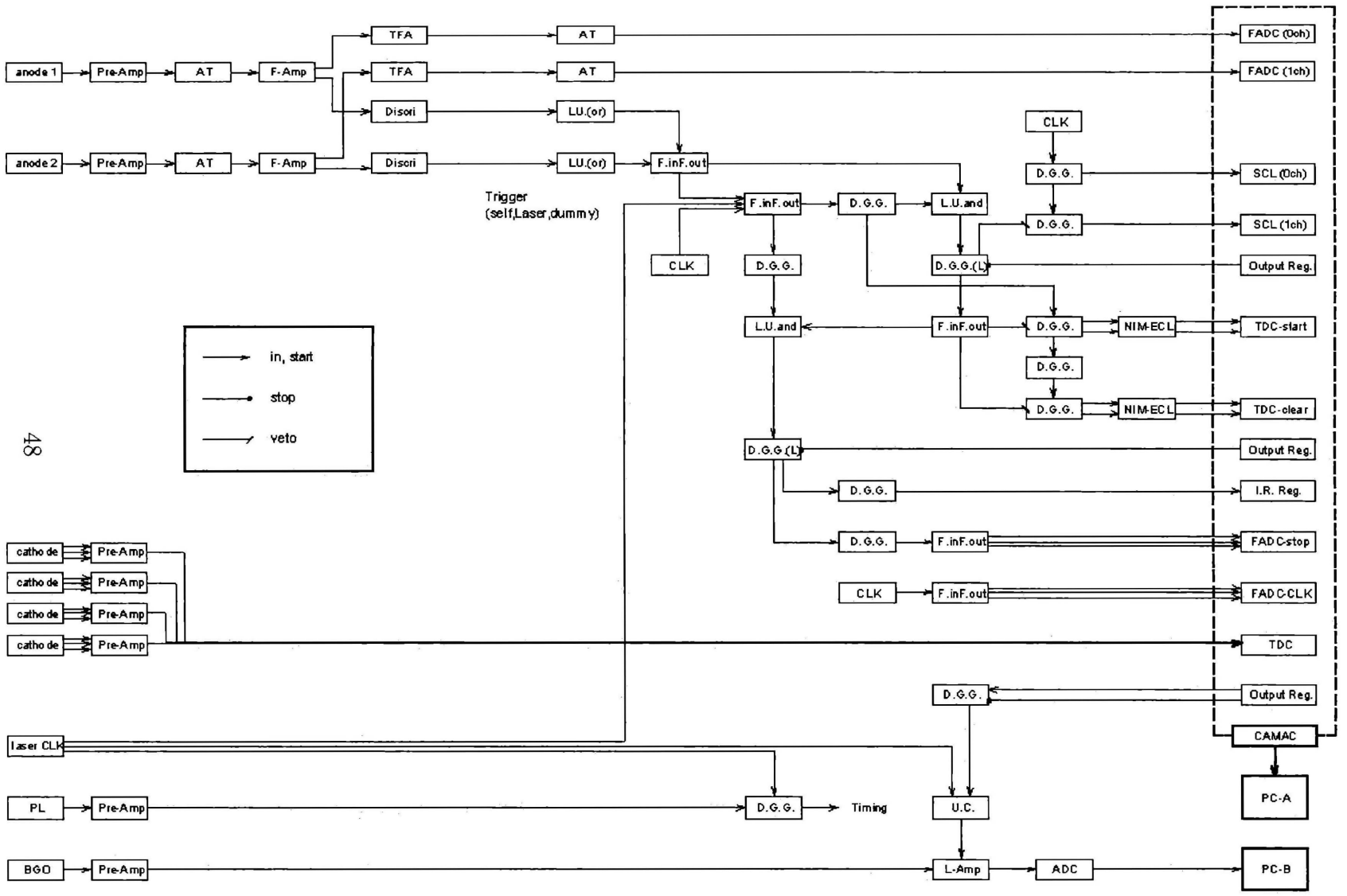


Figure 2.12: The outline of the data acquisition system

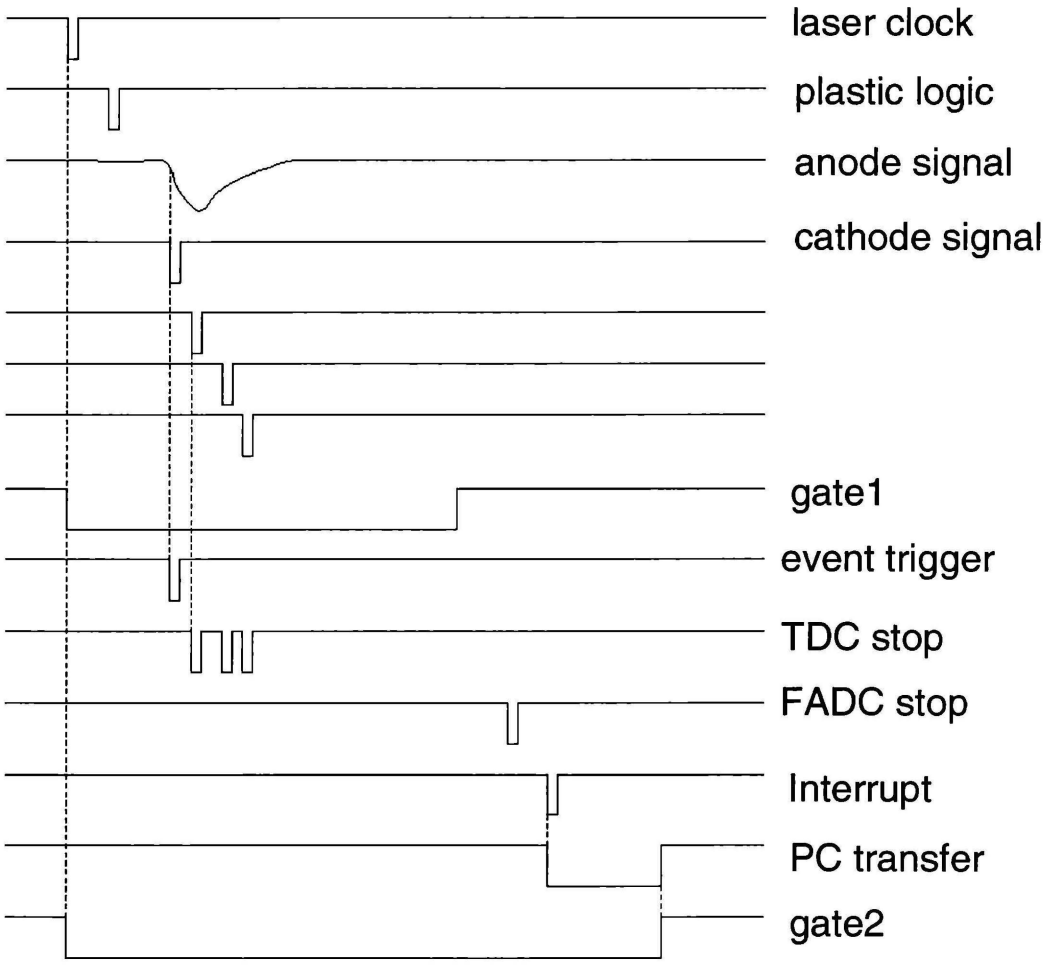


Figure 2.13: The timing chart

turned out that the AC power line of TERAS systems differs from the power source of the hot-water-supply room and noises existed on the AC power line.

In order to reduce the noise from the AC power line sufficiently, we used two AC line filters in cascade. The level of the noise could be reduced down to 15mV using those filters.

## 2.9 Performance of TPC system

The performance of the TPC was studied using the $\alpha$-ray source for the mixed gases of He(80%) and $CH_4$(20%). The energy and time resolution were measured along the whole drift region by moving the $\alpha$-ray source. The energy resolution was 5.8% as shown in Fig.2.14 and the time resolution was 32nsec, as shown in Fig.2.15. The time resolution corresponds to the position resolution of the z direction of 0.4mm, which is good enough for the present experiment.

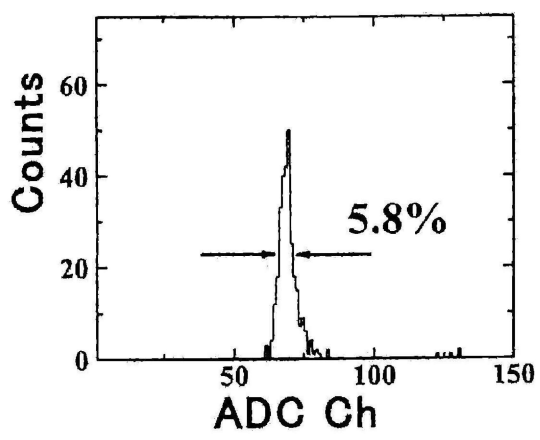


Figure 2.14: The energy resolution of the TPC measured by using the $\alpha$-ray source[44].

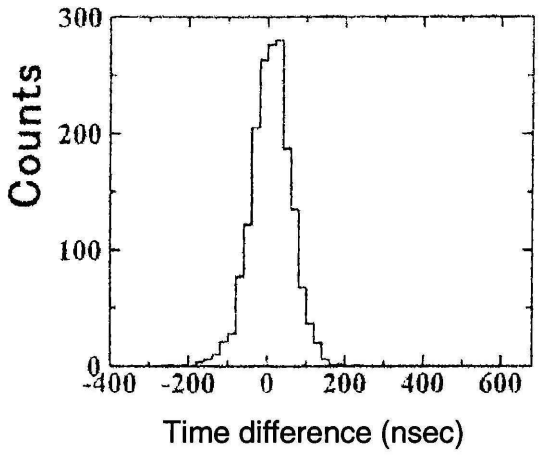


Figure 2.15: The time resolution of the TPC[44].

# 3. Measurements and data analysis

## 3.1 The condition of the measurement

The condition of the measurement is given in Table3.7. The gas pressure of the TPC was set to about 800 torr so that the number of target nuclei was as large as possible, as mentioned in Section 2.6. Since a drift velocity and a rate of the electron multiplication depend on the gas pressure, both the potential of the drift region and the anode potential were optimised. The repetition frequency of the laser was 2.5kHz to obtain the largest power of the laser light.

Table 3.7: The condition of measurement

| | | |
|---|---|---|
| maximum $\gamma$-ray energy | 10.5MeV | 16.5MeV |
| collimator diameter | 2mm | 2mm |
| $\gamma$-ray energy spread(expected values) | $\sim$ 5% | $\sim$ 5% |
| gas pressure | 799.2 torr | 794.8 torr |
| anode potential | +1840V | +1750V |
| potential of drift region(cathode potential) | -4000V | -4000V |
| running time | 71500sec | 147620sec |
| counting rate | $\sim$1cps | $\sim$0.5cps |

Storage electrons gradually decreased with the half life of about 10000 seconds mainly by the collision with the residual gas in a beam tube. Since the intensity of the LCS $\gamma$ rays becomes low as the electron currents decrease, fresh electrons need to be re-stored in TERAS to carry out the experiment efficiently.

The experiment was performed by repeating the cycle of the electron injection.

The count rate of the TPC was $\sim$1cps at 10.5MeV and $\sim$0.5cps at 16.5MeV and the dead time of the measurement system was a few % during the experiment.

## 3.2 Data analysis of TPC

### 3.2.1 Reconstruction of trajectories

Data obtained in the experiment with the TPC are the trajectories of the charged particles and the current of the anode signals produced by the charged particles. Data of trajectories consists of the projection of the trajectory onto the cathode wire plane (xy plane) and the arrival time of the drift electrons to the cathode wire plane (the drift time). (see Section 2.4).

In order to convert the drift time into the z coordinate of the trajectory one has to know the drift velocity of electrons and the start time of the drift.

The drift velocity of electrons was determined by the calibration measurement with $\alpha$-rays as follows. The $\alpha$ source (5.48MeV) was set at the end of the drift region in the TPC. The drift velocity was determined by measuring the drift time of the electrons produced by the $\alpha$ particle and the calculated flight length of the $\alpha$ particle. However in the present gas pressure, the flight length of the $\alpha$-particle (5.48MeV) is about 15 cm, and cannot cover the whole drift region(25cm in length). In the past, we measured the drift velocity in the whole drift region of the TPC using the ultraviolet-rays laser with mixed gas of helium (80%) and methane (20%)[45], where the gas pressure was 700torr and the cathode potential was -3000V. The drift velocity in the same gas is approximately proportional to the strength of an electric field, and inversely proportional to a gas pressure. Therefore, we employed the functional curve of the drift velocity measured in the past[45] and the absolute value of this curve was determined by using the the drift velocity we measured with the $\alpha$-ray during the experiment. And the error for determining the drift velocity with the $\alpha$-ray was 1%. The relation of the drift time and the z coordinate is shown in Fig.3.1.

The start time of the drift is equal to the luminescence time of the plastic scintillator. While the trigger of the TDC was made by using the laser clock. Therefore the drift time was corrected by adding the time difference between the luminescence time of the plastic scintillator and the laser clock to the TDC data. The fluctuation of the time difference which was observed with the digital oscilloscope was $\pm 100ns$. Since the drift velocity is about $1 \times 10^{-2} mm/nsec$, the position resolution in the drift direction is about 1mm.

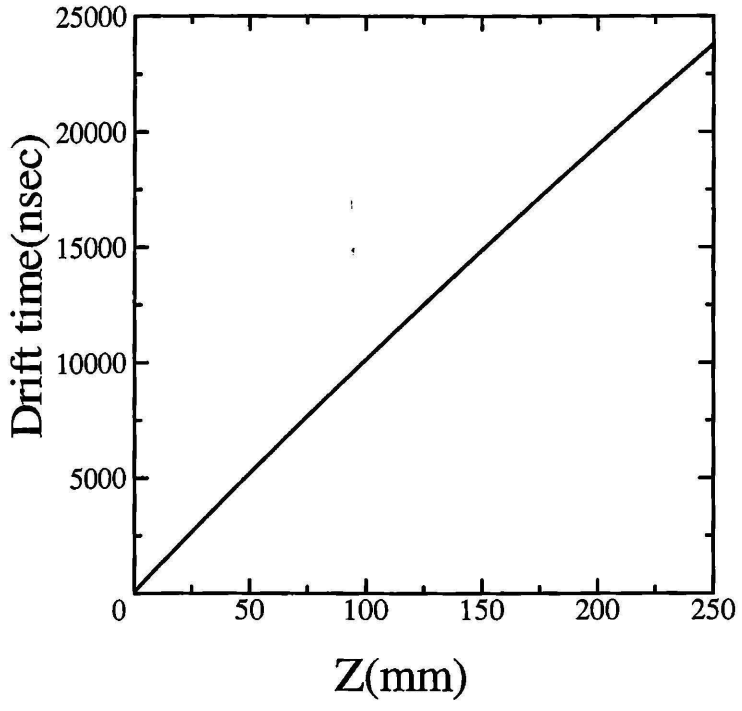


Figure 3.1: Relation of the z position v.s. drift time

### 3.2.2 Analysis of events

In this experiment, we could observe the reaction events by $^3$He photodisintegration and $^{12}$C($\gamma, \alpha\alpha$)$\alpha$ (Q=7.27MeV) at 10.5MeV, and $^3$He photodisintegration and $^{12}$C($\gamma, \alpha\alpha$)$\alpha$ and $^{12}$C($\gamma$,p)$^{11}$B (Q=16.0MeV) at 16.5MeV. Since the Q-value of the $^{12}$C($\gamma$,n)$^{11}$C reaction is 18.7MeV, the $^{12}$C($\gamma$,n)$^{11}$C event was not observed. Also we observed background events and electron events produced by the electromagnetic process between atomic electrons and incident $\gamma$-rays.

Since the incident $\gamma$-rays were collimated by the collimator with 2mm$\phi$, all trajectories of the photodisintegration events originated from the $\gamma$ ray beam axis of 2mm$\phi$. Events, which do not satisfy the condition, are removed as background events. Since the trajectories of all events show characteristic patterns, which reflect the particular reaction, the events of $^3$He photodisintegration can be sorted out from the trajectories. The sorting conditions and typical trajectories are discussed as follows.

In addition to data of trajectories, TDC records the rise time and the falling time of a signal of each cathode wire, as mentioned in Section 2.7. And from the time difference between the rise time and the falling time, the charge (energy loss) of the signal can be obtained. When converting TDC data into the trajectory, both the rise time and the falling time of the signal are converted into the z-coordinates. Therefore, the charge of the signal can be obtained by the width of the trajectory.

**$^3$He($\gamma$,p)D reaction event(Fig.3.2)**

The events of the $^3$He($\gamma$,p)D reactions were identified by checking the following conditions;

1. Both a proton and a deuteron are detected.
2. Both particles are emitted in opposite directions because of the two-body decay.
3. Because of the difference between the energy losses of protons and deuterons, the width of a deuteron track is 3 times larger than that of a proton track.

The typical trajectories are shown in Fig.3.2(at $E_\gamma = 16.5MeV$). The wider track between two tracks which are generated from the $\gamma$-ray axis is a deuteron.

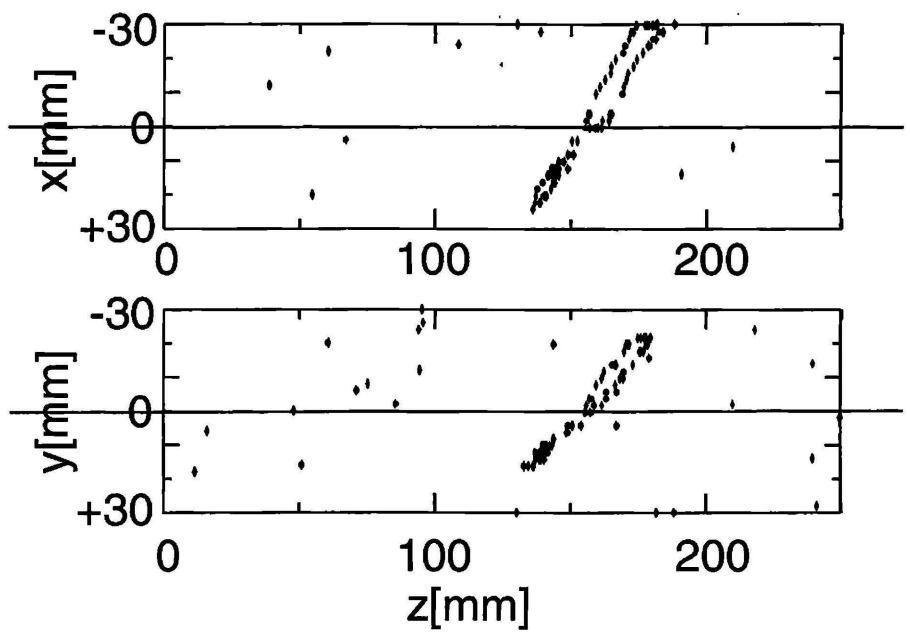


Figure 3.2: Particle trajectories form the $^3He(\gamma,p)D$ reaction at $E_\gamma$=16.5MeV (solid line expresses the $\gamma$-ray axis)

**$^3$He($\gamma$,pp)n reaction event(Fig.3.3)**

The events of the $^3$He($\gamma$,pp)n reactions were identified by checking the following conditions;

1. Two protons among three generated particles are detected.
2. The emitted angles of protons are oriented randomly with respect to one another and with respect to the $\gamma$-ray axis.

Typical trajectories of the three-body breakup are shown in Fig.3.3(at $E_\gamma = 16.5MeV$). Two tracks are generated with random angle from the $\gamma$-ray axis. The width of the track is not constant and depends on the energy of the generated proton.

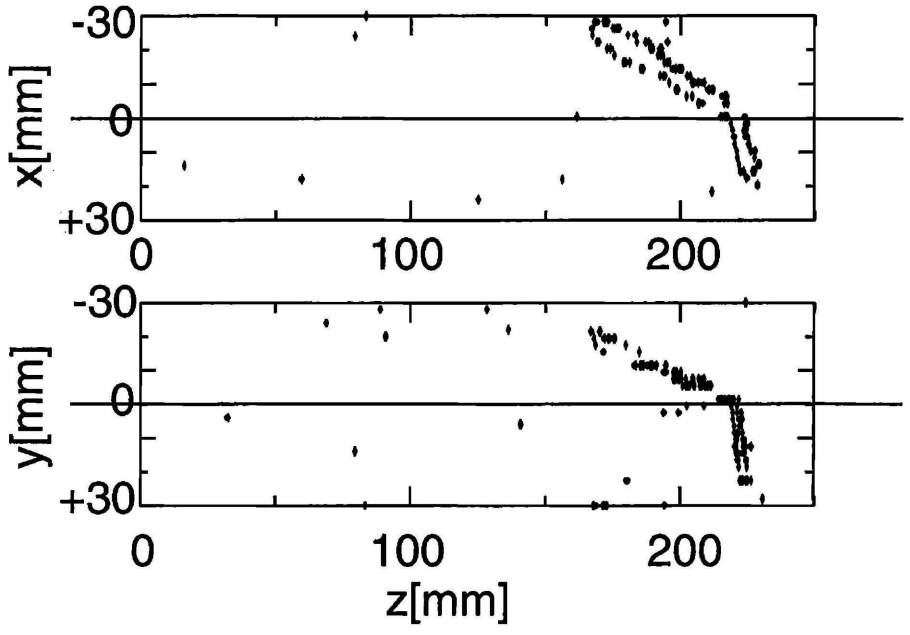


Figure 3.3: Particle trajectories form the $^3He(\gamma, pp)n$ reaction at $E_\gamma$=16.5MeV (solid line expresses the $\gamma$-ray axis)

**Natural background event (Fig.3.4)**

Since most natural background events do not cross the $\gamma$-ray axis, they can be easily rejected. Typical trajectory is shown in Fig.3.4. Natural background events which cross the $\gamma$-ray axis were easily distinguished from the photodisintegration events, since the pulse heights of these events were larger than those of the photodisintegration events. This is described at the end of this Section.

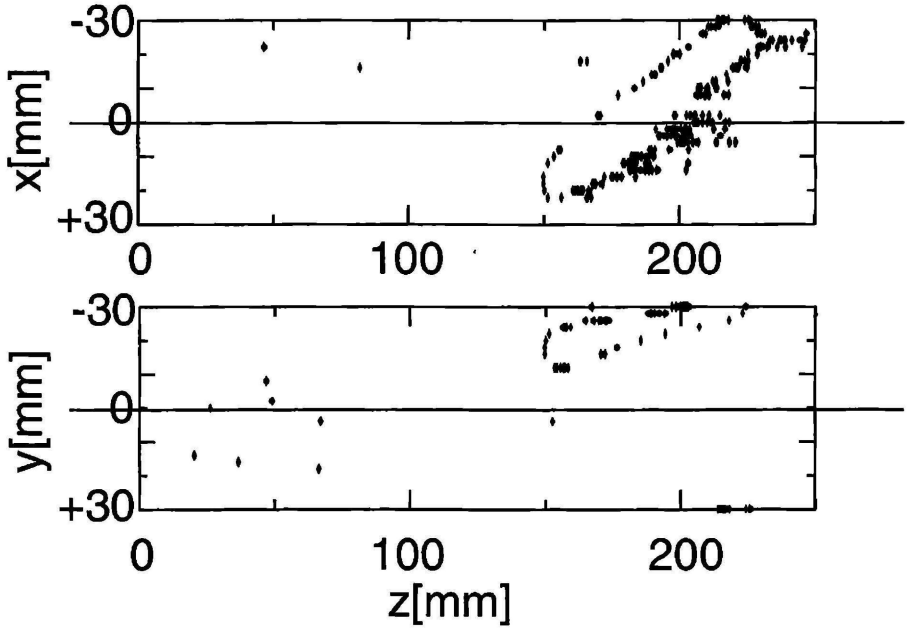


Figure 3.4: Trajectory of natural background (solid line expresses the $\gamma$-ray axis)

**Electron event (Fig.3.5)**

Events of electrons produced by the electromagnetic process between atomic electrons and incident $\gamma$-rays were observed. These electrons have the energy from a few MeV to a few tens MeV, but the energy loss of the electrons per unit length is 1/10 or less than those of generated particles by the $^3$He photodisintegration. Therefore the electron signal seldom exceeds the discrimination levels of cathode wires and only the part of trajectory is observed. A typical electron trajectory is shown as a dot in Fig.3.5.

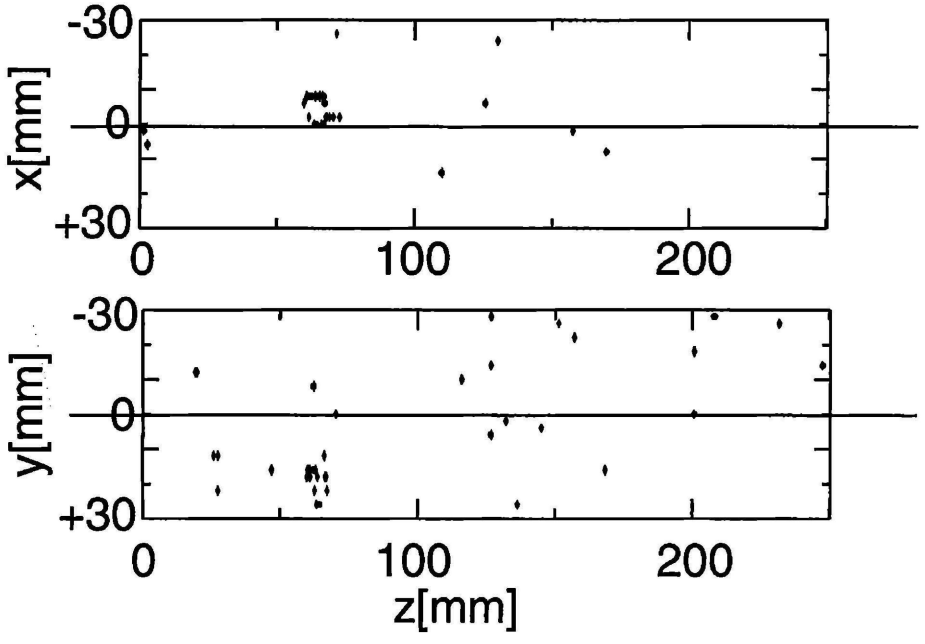


Figure 3.5: Trajectory of electron event (solid line expresses the $\gamma$-ray axis)

**$^{12}$C($\gamma$,p)$^{11}$B (Fig.3.6) and $^{12}$C($\gamma, \alpha\alpha)\alpha$ reaction events (Fig.3.7)**

Since the methane gas was used as an operational gas of the TPC, we observed the events from the $^{12}$C($\gamma$,p)$^{11}$B and $^{12}$C($\gamma, \alpha\alpha)\alpha$ reactions. In the $^{12}$C($\gamma$,p)$^{11}$B reaction, a proton and $^{11}$B are detected. The flight length of $^{11}$B is very short and therefore the track of $^{11}$B is appeared as a large dot on the $\gamma$-ray axis, while the track of a proton is connected to the large dot. In the $^{12}$C($\gamma, \alpha\alpha)\alpha$ reaction, three $\alpha$ particles are detected. Three tracks are extended from the $\gamma$-ray axis. Typical trajectories are shown in Fig.3.6 ($^{12}$C($\gamma$,p)$^{11}$B) and Fig.3.7 ($^{12}$C($\gamma, \alpha\alpha)\alpha$),respectively.

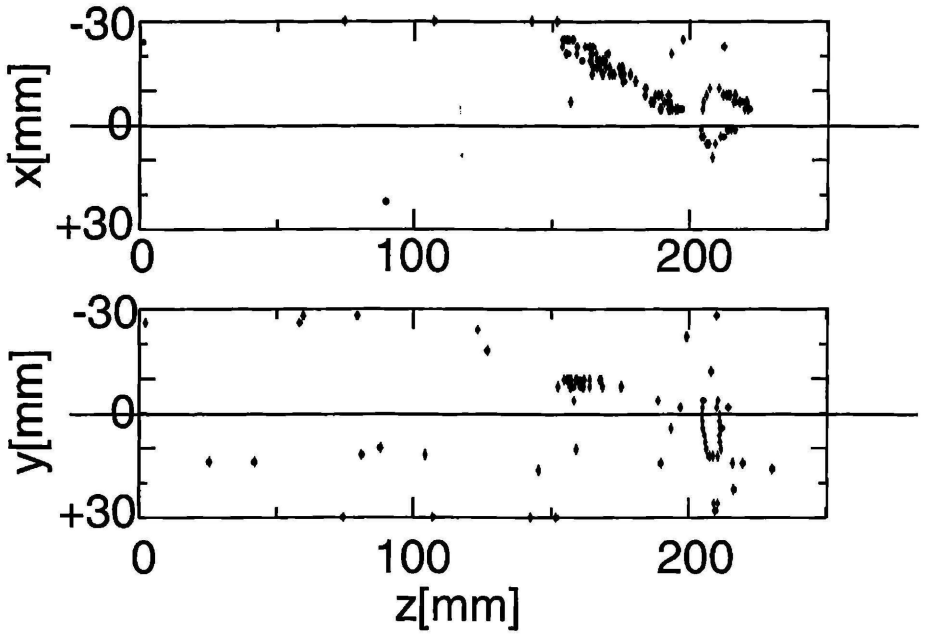


Figure 3.6: Particle trajectories from the $^{12}C(\gamma, p)^{11}B$ reaction (solid line expresses the $\gamma$-ray axis)

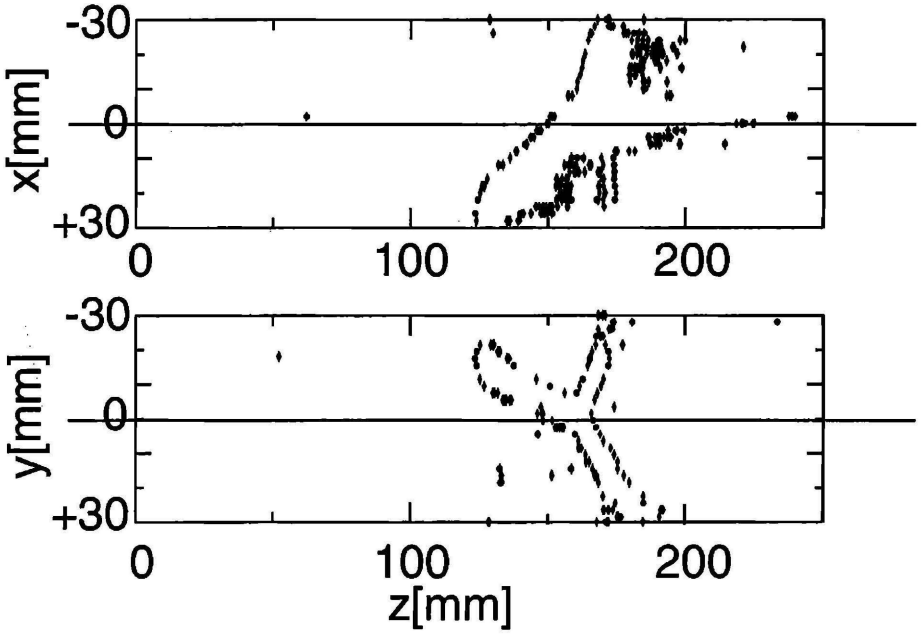


Figure 3.7: Particle trajectories from the $^{12}C(\gamma, \alpha\alpha)\alpha$ reaction (solid line expresses the $\gamma$-ray axis)

Using the above mentioned conditions, events due to the $^3$He photodisintegration were selected out from all detected events. Almost all events can be identified with above-mentioned conditions, but the events which occurred near the both ends of the drift region ($z \sim 0mm$ and $\sim 250mm$) are hard to be identified clearly due to the distortion of the electric field in these places. This problem is described in the next Section where the detection efficiency of the TPC is argued.

Although we could identify the true events from the photodisintegration of $^3$He with the method described above, we might have the problem to distinguish the natural background and/or the two-body breakup from the three-body breakup, which happened in the following kinematic condition. Namely, for the three-body breakup there is a case in which two protons are emitted in opposite directions. In such a case, the ratio of the energy of one proton $E_{P1}$ and another proton $E_{P2}$ becomes (A) $E_{P1}$ : $E_{P2}$=1:1 or (B) 1:2, because of conservation laws.

In the case of (A), the tracks of two protons have the same width. The two such events were observed in all events of the three-body break up. A natural background, which crosses the $\gamma$-ray axis, can have a similar trajectory. However since the pulse heights of natural background are larger than those of the three-body breakup, the distinction between the three-body breakup and the natural background is easy. The histogram of the anode pulse heights (charge) of the three-body breakup and the natural backgrounds which crossed the $\gamma$-ray axis is shown in Fig.3.8. These two events are clearly separated.

In the case of (B), since two protons are emitted in opposite direction with different energies, such three-body breakup event may be misidentified as a two-body breakup event with a proton and a deuteron. Certainly the energy loss for the three-body breakup is different from that for the two-body breakup; at $E_\gamma = 16.5MeV$ the energy loss for the three-body breakup is 51keV/cm and 30keV/cm for two protons and that for the two-body breakup is 19keV/cm for a proton 59keV/cm for a deuteron, respectively, and at $E_\gamma = 10.5MeV$ the energy loss for the three-body breakup is 121keV/cm and 73keV/cm for two protons and that for the two-body breakup is 37keV/cm for a proton and 110keV/cm for a deuteron, respectively. Although there is a finite difference of the energy loss between the three-body breakup and the two-body breakup, one cannot identify the event clearly whether it is due to the two-body or the three-body breakup. Hence we did not use the event in the present analysis. We had one such event in all events. When we estimate the experimental error in the present experiment, we consider the event as a source of systematic error.

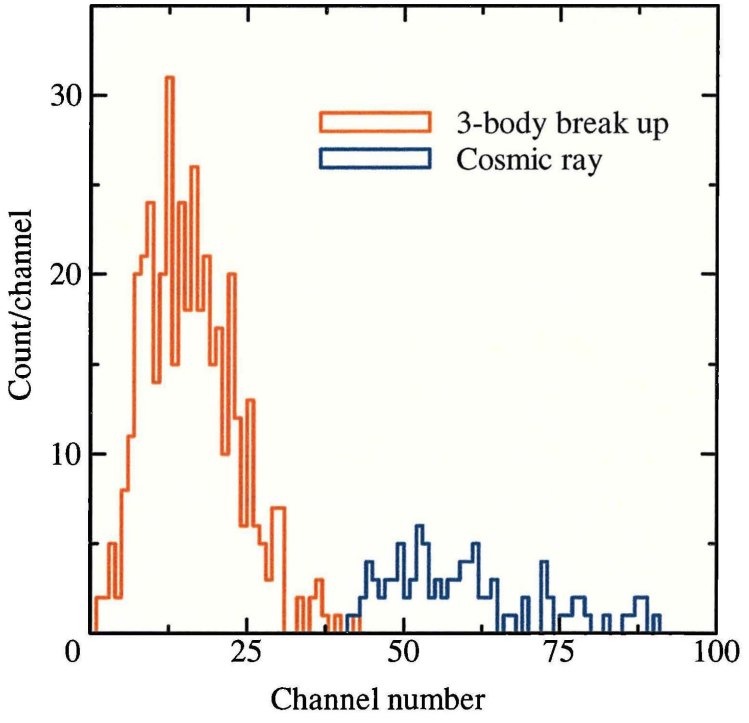


Figure 3.8: The histogram of the anode pulse heights (charge) of the three-body breakup and natural background, which passed the $\gamma$-ray axis.

### 3.2.3 The number of events

The true events of the two-body breakup and the three-body breakup of the $^3$He photodisintegration were distinguished from background as discussed before, and the total events thus analysed are given in Table 3.9.

Table 3.8: The number of events

| incident $\gamma$-ray energy | 10.5MeV | | 16.5MeV | |
|---|---|---|---|---|
| reaction | $^3$He($\gamma$,p)d | $^3$He($\gamma$,pp)n | $^3$He($\gamma$,p)d | $^3$He($\gamma$,pp)n |
| the number of events | 399 | 85 | 256 | 387 |

### 3.2.4 Detection efficiency of TPC and Effective length

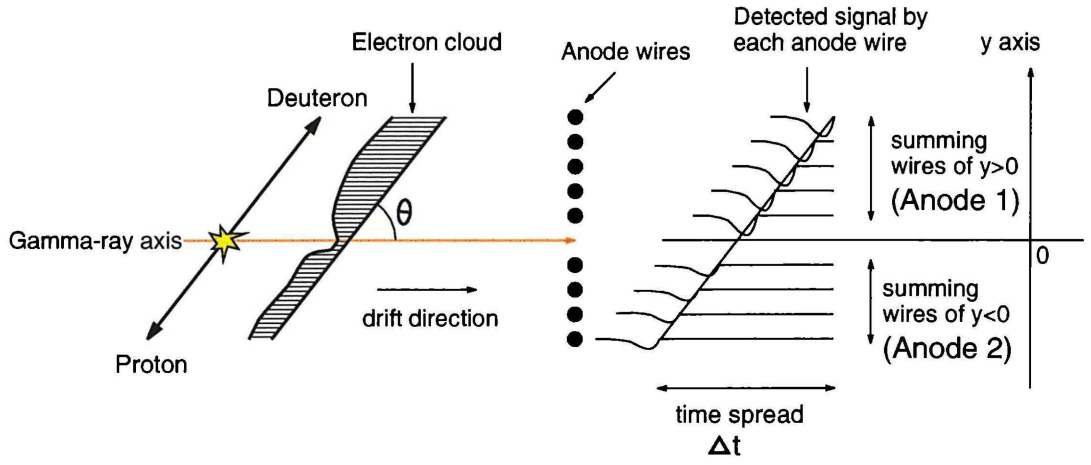


Figure 3.9: Schematic diagram for producing anode signals

In order to determine the photodisintegration cross section of $^3$He using observed events by the TPC we have to know the detection efficiency of charged particles emitted from the reaction and the effective length of the TPC. Since the present TPC contains an active gas target of $^3$He, one would expect the detection efficiency of the TPC to be about 100%. However, the efficiency may not be as high as 100% because of the following possible reasons. First the emitted charged particles from the three-body breakup have broad energy distribution. Second when the electrons produced by the charged particles drift to the anode direction, some of the electrons may be captured by impurities in the TPC and thus the electron number at the anode will decrease. Third one has to set a discrimination level to reject electronic noise.

Hence when pulse heights due to the emitted charged particles become low, the efficiency of the TPC may decrease. Since the second point mentioned above is crucial to determine the efficiency, we discuss the way to make the pulse height spectrum for the emitted charged particles.

A schematic diagram for producing the anode signal for the two-body breakup is shown in Fig.3.9. The y=0 expresses the $\gamma$ ray beam axis here. The anode signals above (Anode 1) and below (Anode 2) z=0 axis were separately sent to the data taking system. Hence when a proton and a deuteron are emitted in opposite directions from the $\gamma$ ray axis in the two-body breakup, we can detect a proton or a deuteron with Anode 1.

A pulse peak height of the Anode 1 (Anode 2) depends on $\theta$, where $\theta$ is an emission angle of a particle with respect to the $\gamma$-ray axis. A time spread $\Delta t$ in Fig.3.9 is smallest at

$\theta = 90°$ and becomes large as $\theta$ approaches to $0°$. The signal of the Anode 1 (Anode 2) has a sharp peak when $\Delta t$ is small, and has a broad small peak when $\Delta t$ is large. The waveform of the Anode 1 (Anode 2) is recorded by the FADC as shown in Fig.3.10. The wave form for $\theta = 90°$ rises sharply and the peak height of the wave form is high. While the wave form for $\theta = 46°$ rise slowly and the peak of the wave form is low. Here it should be noted that a total area of a wave form is equivalent to the energy loss of a particle in the drift region.

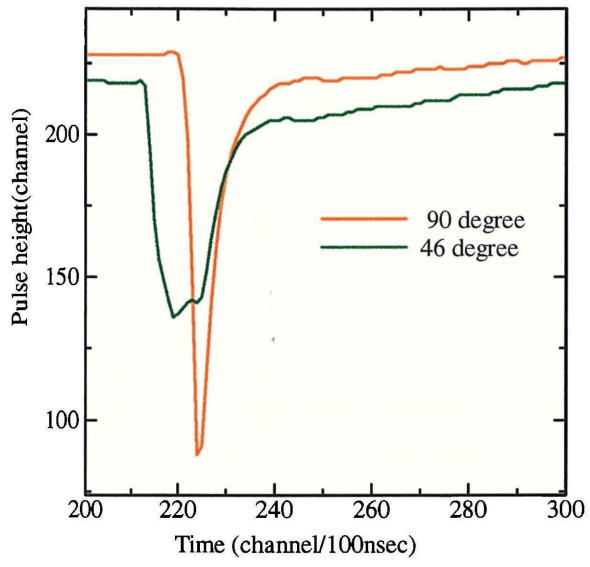


Figure 3.10: Anode pulse wave form of deuteron from the two-body breakup of $^3$He at $E_\gamma$=16.5MeV

Off set level of the signals were shifted in order to make it legible.

In the measurement system, the event which exceeds the discrimination level of the anode is only recorded. A discriminator for the anode signal is a simple comparator as well as that of the cathode signal, and it generates a logic signal only when the signal exceeds the threshold voltage. Two anode signals (Anode 1 and Anode 2) are discriminated independently. The histogram of the pulse peaks of electron events is shown in Fig.3.11. Since an electron event has a small pulse peak and the number of electron events is very large, electron events can be used for determining the discrimination level for the FADC. In Fig.3.11, the discrimination level of the Anode 1 ($y > 0$) was determined as 14 channel.

The pulse peak distribution those obtained for the two-body and three-body breakup is shown in Figs.3.12 and 3.13, as a function of the position (z) along the z axis, where a higher peak between two signals of the anode (Anode 1 and 2), is shown. The green line is the

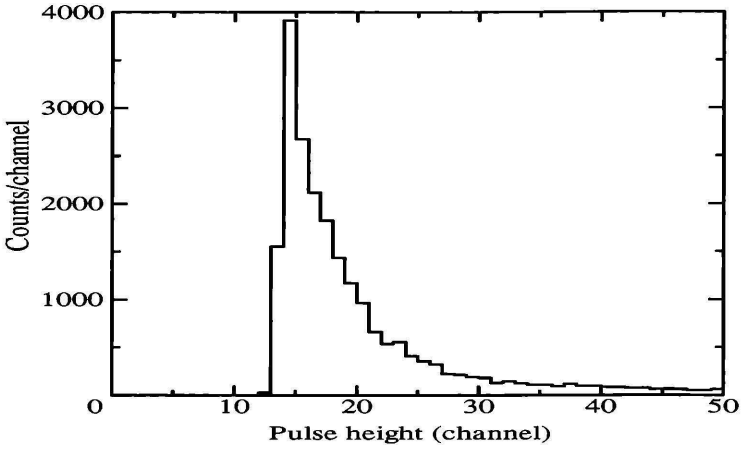


Figure 3.11: Pulse peak histogram of the anode signal($y > 0$) at $E_\gamma$=16.5MeV

discrimination level. The peak channel is corrected for so that the discrimination level of Anode 2 may agree with that of Anode 1. We can clearly see that the pulse peak decreases as the drift length (z) for the electrons increases. This can be understood as follows. Namely the impurities in the TPC make the pulse peak low. And also when the signal is produced far away from the anode wire plane, the time spread $\Delta t$ becomes larger than that of the signal near the anode wire plane. This is because the influence of slight distortion of the drift velocity on $\Delta t$ increases as the distance from the anode wire plane increases. The pulse peak for the three-body breakup(Fig.3.13) has wider distribution than the two-body breakup, because the generated proton has various energy.

As discussed above the anode signal is discriminated by not the total charge of the signal but an instantaneous pulse height of the signal. The pulse height, thus obtained, changes greatly with the emitted angle of a particle and the position of the emitted particles from the anode plane. Hence in order to determine the detection efficiency of the TPC, one has to know the attenuation rate of the pulse peak as a function of the distance z. And the detection efficiency determined by the discrimination level of the anode signal ( the detector efficiency ) was calculated with the Monte Carlo simulation. Furthermore, the total detection efficiency was derived in analysing the trajectory data obtained from the simulation.

### Attenuation rate of the pulse peak

The attenuation rate of the pulse peak was determined using the two-body breakup data. The reason is that the variations of the pulse peaks for the two-body breakup are smaller

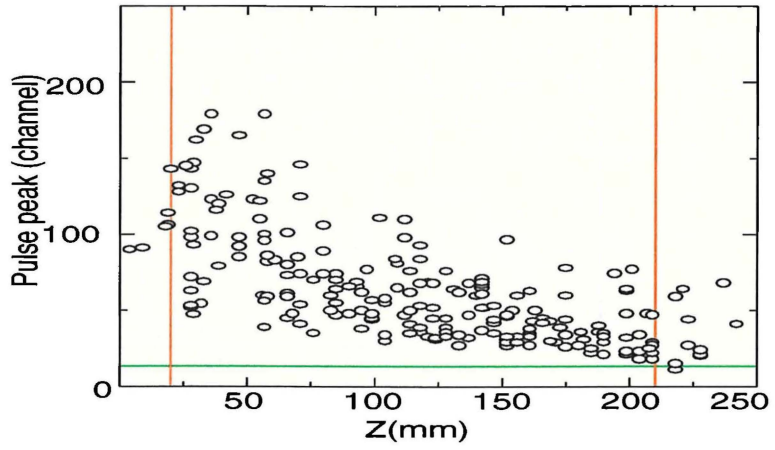


Figure 3.12: Pulse peak distribution of the particle emitted from the $^3He(\gamma,p)d$ reaction at $E_\gamma$=16.5MeV

Two red lines correspond to the z position of 20mm and 210mm, respectively

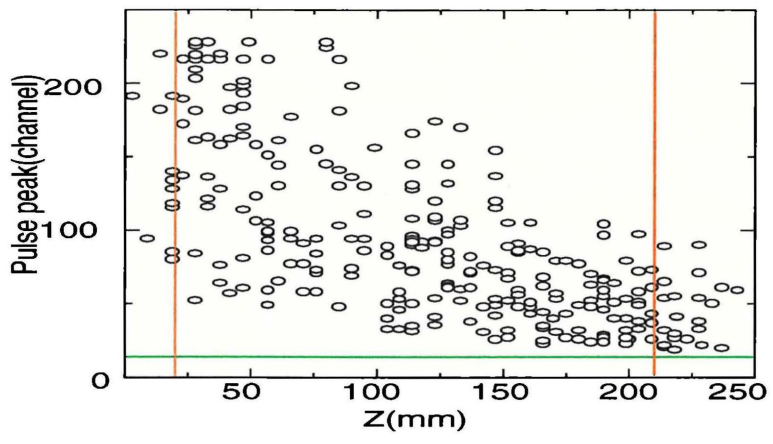


Figure 3.13: Pulse peak distribution of the particle emitted from the $^3He(\gamma,pp)n$ reaction at $E_\gamma$=16.5MeV

Two red lines correspond to the z position of 20mm and 210mm, respectively

than the three-body break up, since generated particles in the two-body breakup have the same energy determined by energy conservation law. The relation between the pulse peak and the z coordinate for deuteron events in the two-body break is shown in Fig.3.14, when the emitted angle $\theta$ is between 30° and 55°. The reason to use the deuteron is that the pulse peak resolution for the deuteron signal in the FADC is better than the proton, since the pulse peak of the deuteron is larger than that of a proton. Here it should be mentioned that in order to determine the attenuation rate of the pulse peak it is important to select the event at a certain point on the z-axis, whose pulse peak does not change so much. We used the data taken between $\theta = 30°$ to $\theta = 55°$. Events with $\theta$ less than 30° have long trajectories in the z-direction, and therefore they are unsuitable for determining the position dependence of the rate of the pulse height.

Although we can draw a straight line using the data in Fig.3.14, it would be nice if we can reduce the width of the data point. For this purpose we made the corrections for the angle and the energy loss of emitted particles. The corrections were performed in the region between z=20 and z=220 mm. Since deuterons have the same energy, the energy loss inside the TPC is equal to the flight lengths of the deuterons. Therefore, the area (energy loss) of the pulse of each events in Fig3.14 was normalised in the area of the pulse at $\theta$=30° by taking the ratio of flight length. Furthermore, since the $\Delta t$ was roughly inversely proportional to the pulse peak of the signal, the pulse peak in Fig.3.14 was multiplied by the ratio of the $\Delta t$ at $\theta$ and $\Delta t$ at 30°. The result is shown in Fig.3.15. The spectrum in Fig.3.15 expresses the change of a pulse peak against the z-coordinate when all particles are emitted to the direction of 30°.

The solid line indicates the rate of the attenuation obtained by the least square method. In the calculation, events between z=30mm to 200mm were used in order to avoid the influence of the discrimination level.

### Determination of detection efficiency by Monte Carlo simulation

The detector efficiency was first calculated using the Monte Carlo simulation code which our group developed. This simulation calculates a physical process of the $^3$He photodisintegration reaction in the TPC. Since the photodisintegration of $^3$He proceeds almost an E1 component, the simulation takes only the E1 component into consideration. And the similar data as obtained in the experiment can be calculated.

A histogram of the pulse peaks in the two-body breakup channel ($z = 20 \sim 210mm$) is shown in Fig.3.16, where a green line expresses the discrimination level. Experimental data obtained at $E_\gamma$=16.5MeV are corrected for by the rate of the attenuation. The simulation (red line) is in agreement with experimental data with the accuracy of $\chi^2/N = 1.04$.

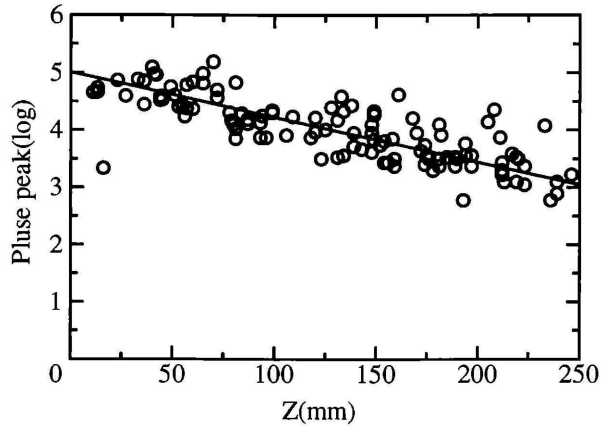


Figure 3.14: Pulse peak distribution of the particle emitted from the $^3He(\gamma,p)d$ reaction at $E_\gamma$=16.5MeV ($\theta = 30^o \sim 55^o$) A solid line expresses the attenuation rate of the pulse peak.

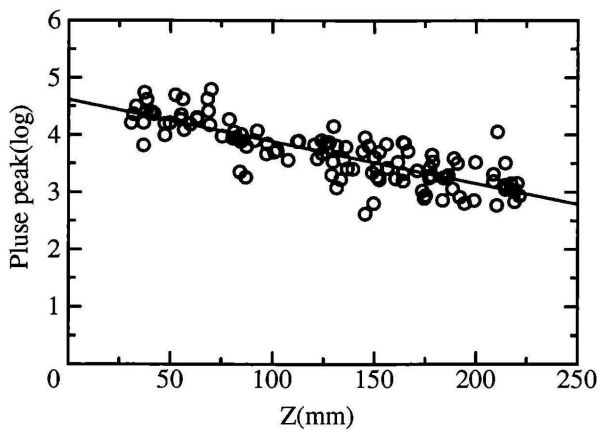


Figure 3.15: Corrected pulse peak distribution of the particle emitted form the $^3$He$(\gamma,p)d$ reaction at $E_\gamma$=16.5MeV

A solid line expresses the attenuation rate of the pulse peak.

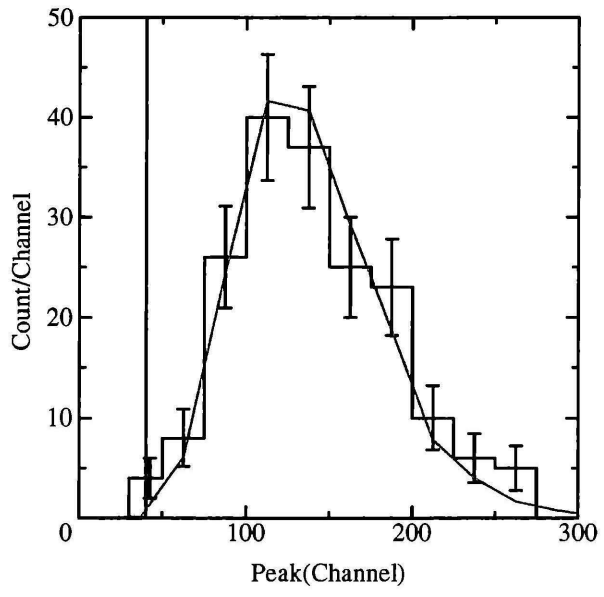


Figure 3.16: Pulse peak histogram of the particle emitted from the $^3He(\gamma,p)d$ reaction at $E_\gamma$=16.5MeV. A green line is the discrimination level of the anode signal. A red line is obtained by simulation ($\chi^2/N \sim 1.04$)

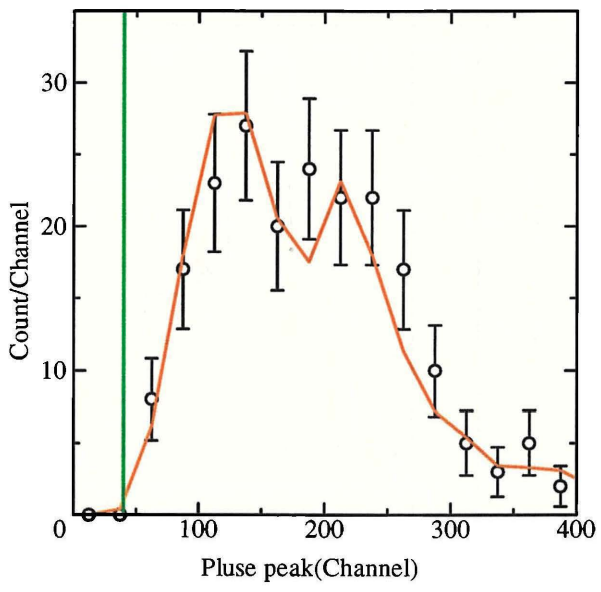


Figure 3.17: Pulse peak histogram of the particle emitted from the $^3He(\gamma, pp)n$ reaction at $E_\gamma$=16.5MeV. A green line is the discrimination level of the anode signal. A red line is obtained by simulation ($\chi^2/N \sim 0.57$)

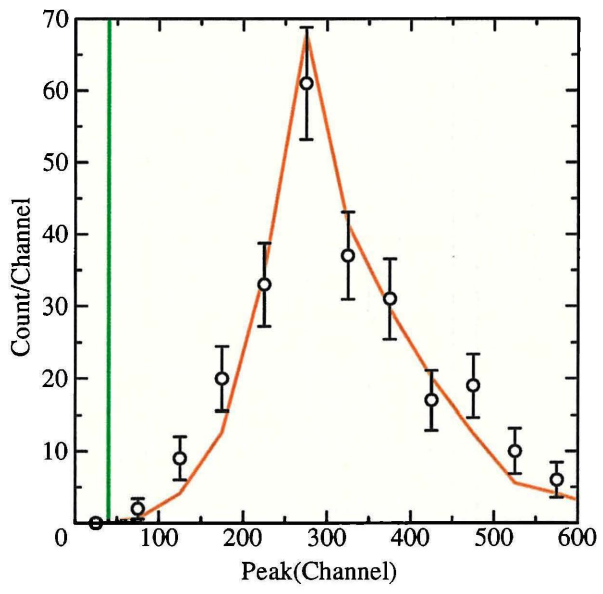


Figure 3.18: Pulse peak histogram of the particle emitted from the $^3He(\gamma,p)d$ reaction at $E_\gamma$=10.5MeV. A green line is the discrimination level of the anode signal. A red line is obtained by simulation ($\chi^2/N \sim 1.40$)

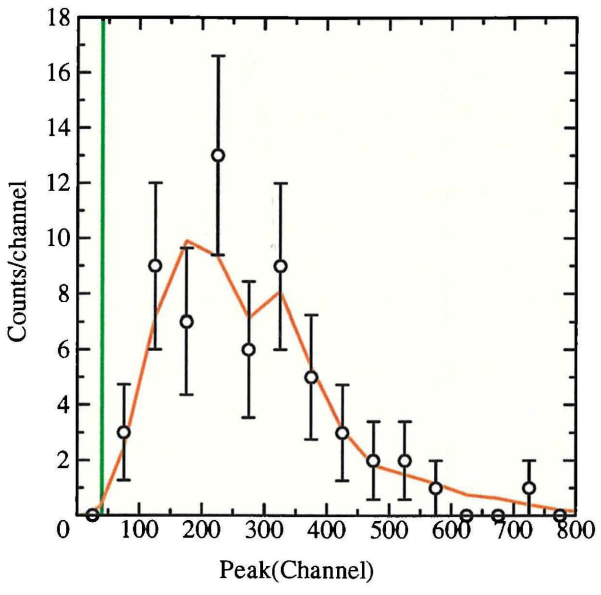


Figure 3.19: Pulse peak histogram of the particle emitted from the $^3He(\gamma, pp)n$ reaction at $E_\gamma$=10.5MeV. A green line is the discrimination level of the anode signal. A red line is obtained by simulation ($\chi^2/N \sim 0.24$)

Next, a histogram of the pulse peaks for the three-body breakup ($z = 20 \sim 210mm$) is shown in Fig.3.17, where the experimental data were obtained at $E_\gamma$=16.5MeV. In order to perform the simulation for the three-body breakup, we have to know an energy distribution of a generated proton or neutron. The energy distribution measured by Fetisov *et al.* is in good agreement with the calculated one by B.F.Gibson and D.R.Lehman[30]. Hence the simulation was performed using the calculated curve by B.F.Gibson and D.R.Lehman. And the result is in agreement with the experimental data with accuracy of $\chi^2/N = 0.57$. The peak near 200 channel in Fig.3.17 is due to the saturation of the FADC. Similarly, the pulse peak histogram of the particle emitted from the $^3$He photodisintegration at $E_\gamma$=10.5MeV is obtained for the two-body breakup and three-body breakup as shown in Figs.3.18 and 3.19, respectively.

It is shown that all the pulse peak obtained at $E_\gamma$=10.5 and 16.5MeV for the two-body and three-body breakup reactions for $^3$He are well above the discrimination level of the anode signals. Namely, the true signals from the $^3$He photodisintegration are not lost by the hardware discriminator. An average pulse peak for the three-body breakup is larger than that for the two-body breakup. If a proton and a deuteron have same energy, an energy loss per unit length of the deuteron is about twice larger than that of the proton. The reason why an average pulse peak for the three-body breakup is larger is as follows,

1. A generated proton can have various energy between $0 \sim 4.4MeV$ at $E_\gamma = 16.5MeV$ and $0 \sim 1.4MeV$ at $E_\gamma = 10.5MeV$. An energy loss per unit length of a proton for the three-body breakup is often larger than that of a deuteron for the two-body breakup.

2. In the two-body breakup, if a deuteron is detected by the Anode 1, a proton is always detected by the Anode 2($y < 0$). On the other hand, each proton is emitted at various angle for the three-body breakup, therefore both two protons are often detected by the Anode 1 (Anode 2). In such case a pulse peak of the anode signal becomes large.

A detector efficiency for the two-body and three-body breakup is calculated by taking the ratio of events which exceed the discrimination level to all events, and is shown in Figs.3.20 and 3.21 with a blue line, respectively.

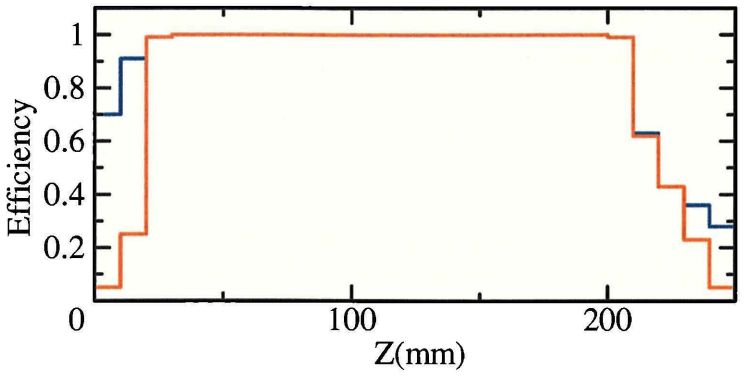


Figure 3.20: Detection efficiency of the TPC for the $^3He(\gamma,p)d$ reaction at $E_\gamma$=16.5MeV The red and blue lines indicate the analysis and detector efficiencies, respectively.

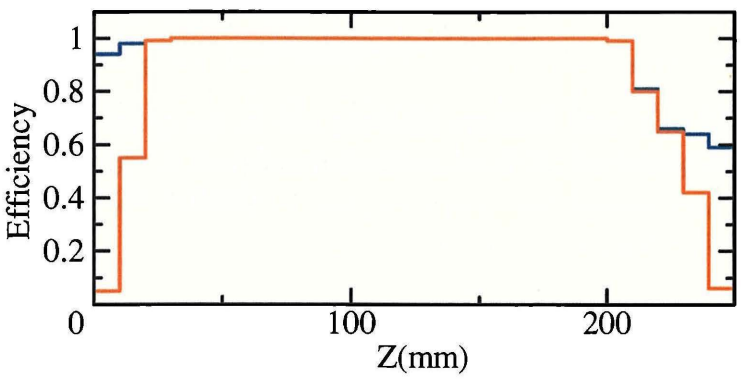


Figure 3.21: Detection efficiency of the TPC for the $^3He(\gamma,pp)n$ reaction at $E_\gamma$=16.5MeV The red and blue lines indicate the analysis and detector efficiencies, respectively.

### Detection efficiency of analysis

The trajectories of the events, which exceed the discrimination level in the simulation, are analysed to obtain the efficiency of analysis. Among the $^3$He photodisintegration events the ambiguous event was removed in the analysis (Section 3.2.2). Such events existed near z=0mm and near z=250mm.

### Near z=0mm

A schematic diagram of generating ambiguous events and an example of ambiguous events are shown in Figs.3.22 and 3.23, respectively. The electric field, which accelerates electrons to the z=0 direction, exists even in the region $z < 0$. Therefore one observes a particle track in this region. In such a case, a trajectory of the particle looks as if the two particles are emitted from the $z = 0$ position. Hence it is difficult to identify the event whether it is due to the three-body breakup or two-body breakup or natural background. Therefore, we exclude such events before the analysis.

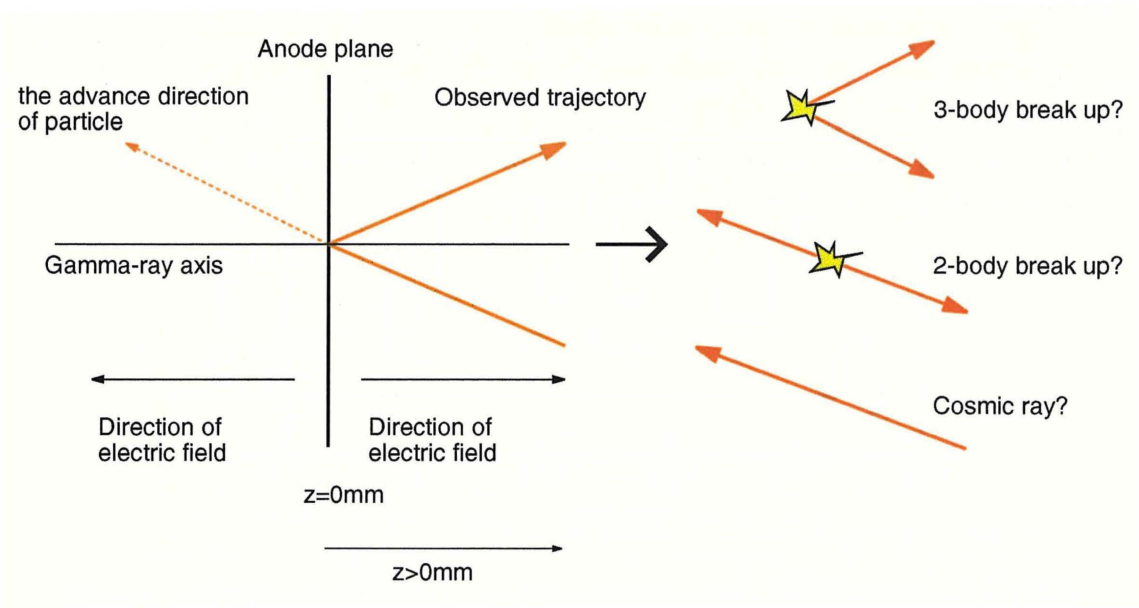


Figure 3.22: Schematic diagram of the events occurred near z=0.

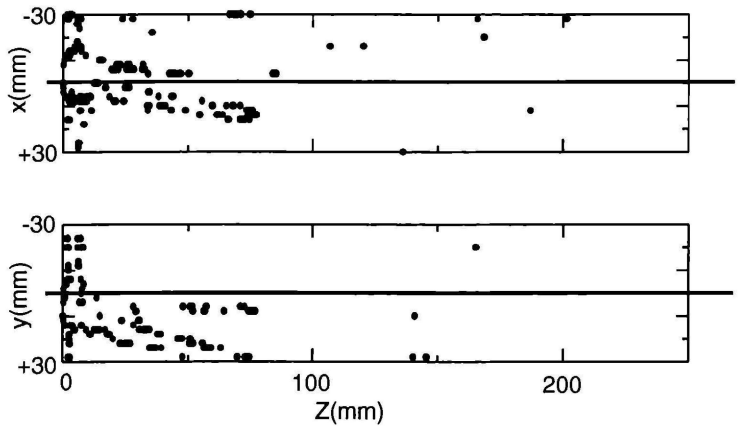


Figure 3.23: Events near z=0mm

### Near z=250mm

In the region $z > 250mm$ the direction of the electric field is different from that in the region of $z < 0$. Hence we can not observe the particle trajectory in the region $z > 250mm$. An example of ambiguous events near $z = 250mm$ is shown in Fig.3.24. Since we could not observe the particle trajectory in the region $z > 250mm$, it is difficult to identify the event whether it is due to the three-body breakup or two-body breakup or natural background. Therefore we exclude such events before the analysis.

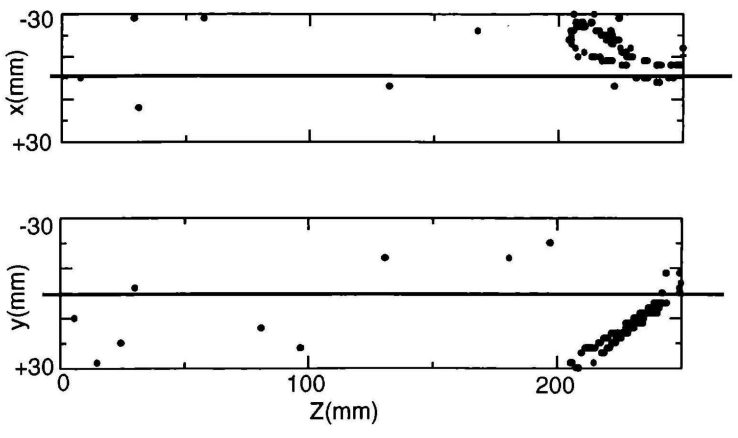


Figure 3.24: Events near z=250mm

The efficiency of analysis is defined as the ratio of analysed events number to events which exceed the discrimination level. A total detection efficiency is obtained as the product of a detector efficiency and an analysis efficiency, and is shown as a red line in Figs.3.20 and 3.21, respectively. The total detection efficiency is 99% or more in the region of $z = 20mm \sim 210mm$. At $z > 210mm$, the detection efficiency decreases because of the attenuation of the pulse peak. At $z < 20mm$ and $z > 230mm$, the detection efficiency decreases by the effect of the ambiguous events.

The accuracy in the determination of the position in the z direction is 2mm, including the inaccuracies of the drift velocity and the timing of the trigger signal of the TPC. Therefore although the detection efficiency is more than 99% in the region of $z = 20 \sim 210mm$, the effective region was taken between $z = 25$ and $205mm$ by taking account of the position resolution. The distributions of the particle tracks along the z axis for the two-body breakup and three-body breakup are shown in Figs.3.25 and 3.26, respectively. In the region between two red lines the detection efficiency is more than 99%. The effective region is 5mm inner side from each red lines. Though the event distributions have statistical uncertainties, they agree with the efficiency curves. And the effective region at $E_\gamma = 10.5MeV$ was also taken between $z = 25mm$ and $z = 205mm$. The number of events within the effective region and the statistical error are shown in Table3.9.

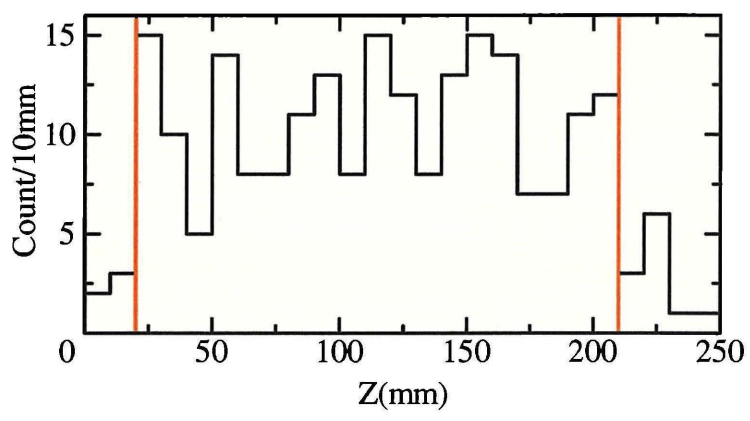


Figure 3.25: Event distribution of the $^3He(\gamma,p)d$ reaction at $E_\gamma$=16.5MeV
Two red lines correspond to z=20 and 210mm, respectively. (Effective length is z=25 and 205mm)

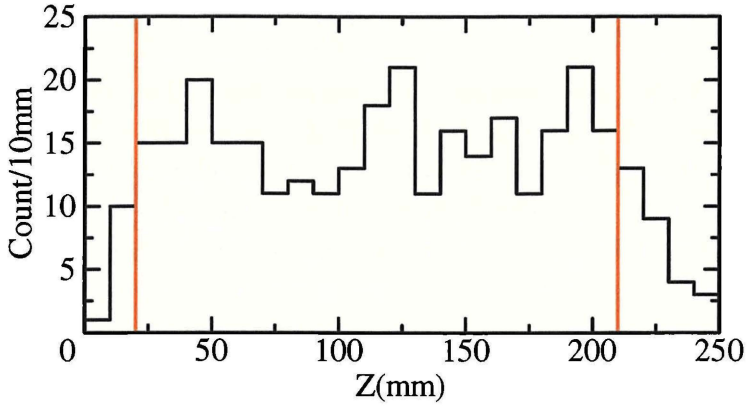


Figure 3.26: Event distribution of the $^3He(\gamma, pp)n$ reaction at $E_\gamma$=16.5MeV
Two red lines correspond to z=20 and 210mm, respectively. (Effective length is z=25 and 205mm)

Table 3.9: The number of events within the effective length

| incident $\gamma$-ray energy | 10.5MeV | | |
|---|---|---|---|
| reaction | $^3$He($\gamma$,p)d | $^3$He($\gamma$,pp)n | $^3$He($\gamma$,p)d+$^3$He($\gamma$,pp)n |
| the number of events | 336 | 65 | 382 |
| statistical error(%) | 5.6 | 12.6 | 5.1 |
| incident $\gamma$-ray energy | 16.5MeV | | |
| reaction | $^3$He($\gamma$,p)d | $^3$He($\gamma$,pp)n | $^3$He($\gamma$,p)d+$^3$He($\gamma$,pp)n |
| the number of events | 204 | 299 | 503 |
| statistical error(%) | 7.0 | 5.8 | 4.5 |

### 3.2.5 The number of target atomic nuclei

The number density of $^3$He atomic nuclei per unit volume is given as follows.

$$N = \frac{4P}{TR} N_A \tag{3.1}$$

Here $P, T, R$, and $N_A$ are the pressure, the temperature, the gas constant, and the Avogadro number, respectively. A time variation of P/T was monitored during the experiment and is shown in Fig.3.27. P/T was kept constant within the error of $\pm 0.4\%$. Substituting the average value of P/T into the equation(3.1), the number density of target atomic nuclei was obtained accurately. The number density of $^3$He and it's error are shown in Tables 3.10 and 3.11, respectively.

Table 3.10: The number density of $^3$He nuclei

| $E_{\gamma max}$ | the number density of $^3$He nuclei |
|---|---|
| 10.5MeV | $2.08 \times 10^{19} atoms/cm^3$ |
| 16.5MeV | $2.06 \times 10^{19} atoms/cm^3$ |

Table 3.11: Evaluation of errors in target thickness

| | |
|---|---|
| chemical purity of $^3$He gas | 99.7% |
| ratio of the quantity of two gas($^3$He:$CH_4$) | error $\pm 0.1\%$ |
| error of temperature measurement | $\pm 1\%$ |
| error of pressure measurement | 0.3% |

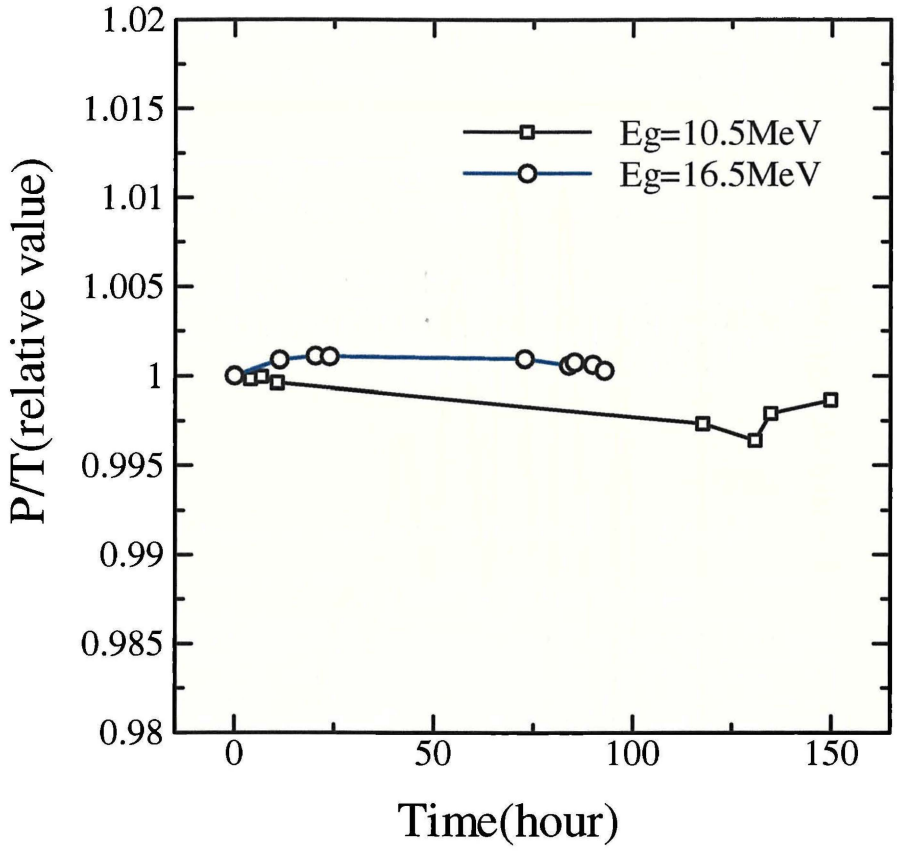


Figure 3.27: Time variation of the ratio of the gas pressure P to the temperature T.

## 3.3 Determinant of $\gamma$-ray flux and $\gamma$-ray energy distribution

### 3.3.1 $\gamma$-ray flux

In order to determine the cross section accurately, the accurate determination of the $\gamma$-ray flux is indispensable. The $\gamma$-ray flux was monitored with the BGO counter during the experiment and it was calculated from the pulse height spectrum of the BGO. A typical BGO spectrum is shown in Fig.3.28.

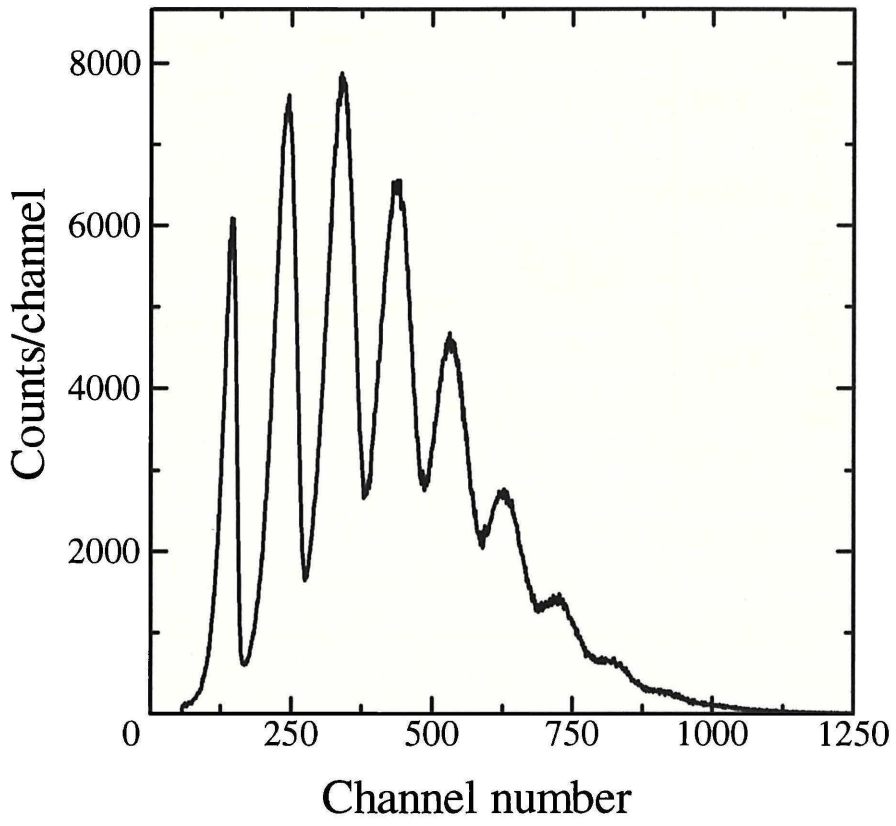


Figure 3.28: The typical LCS $\gamma$ ray spectrum measured by the BGO detector.

We used the pulsed $\gamma$ rays, which were generated with the pulsed laser. In the experiment, the period of a laser pulse was 400$\mu$sec and the width of the pulse was 150ns (Fig.3.29) and a few $\sim$ a few tens photons were generated in one laser pulse. Within this time scale, the separation between the $\gamma$ photon generated by a certain laser pulse and the $\gamma$ photon generated by the next laser pulse is possible, but the $\gamma$ photons generated within the same

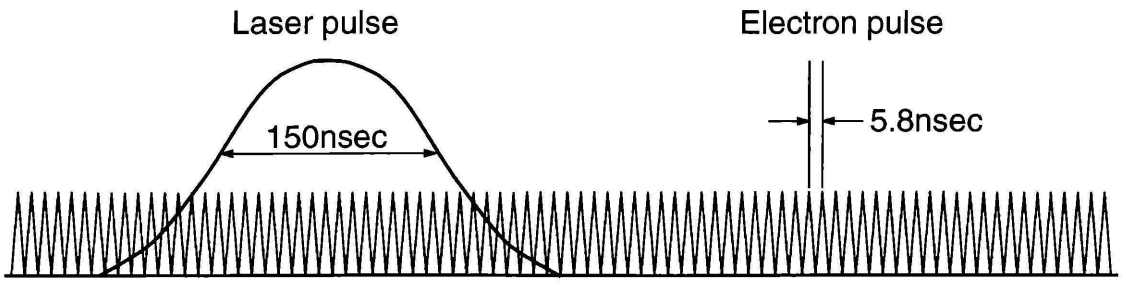


Figure 3.29: Relation of the pulse structure of the electrons and laser. )

pulse cannot be measured separately. Therefore the BGO counter have pile-up signals of the $\gamma$ photons generated by the same laser pulse. We could extract the average number of the $\gamma$ photons per laser pulse from the BGO spectrum as discussed below.

Detection process of $\gamma$-rays can be assumed as follows.

1. An electron pulse period is 5.8ns, and the width of a laser pulse is 150ns. Therefore the electron beam is considered to be a direct current and the $\gamma$-rays are generated by obeying the time distribution of laser pulse.

2. The cross section of Compton backscattering between the laser and the electron is proportional to the number of electrons and that of laser photons. The number of generated $\gamma$ photons is much smaller than that of electrons and of laser photons. Therefore the probability density for generating $\gamma$ photons per laser pulse can be approximated by a Poisson distribution.

3. The BGO responds to each photon independently, and the output of the BGO becomes the sum of the output of each photons.

The $\gamma$ ray flux can be obtained by fitting the BGO spectrum with the response function to M photons taking above mentioned assumption into consideration, where M is the average number of $\gamma$ photons per laser pulse.

The procedure of getting the $\gamma$ ray flux is shown below.

1. First, the response function to one photon was obtained experimentally. A typical BGO spectrum with the pile up component is shown in Fig.3.28. But when the intensity of $\gamma$ rays is very small, the BGO spectrum does not show the pile up spectrum. Such spectrum is obtained when the storage current of electrons is very small or when lowering the laser power. By subtracting backgrounds from this spectrum, the response function to one photon was obtained.

2. The response function to M photons, which obeys the Poisson distribution of average M, is calculated by the Monte Carlo method, based on the response function to one photon. In the calculation, the property of the detection circuits of the measurement system is taken into consideration.

3. By fitting the BGO spectrum with the response function with M photons M was obtained.

4. The $\gamma$-ray flux can be obtained as follows.

$$Y = M \times f \times RT \tag{3.2}$$

   Where $f$ is a laser pulse frequency and $RT$ is a live time of the TPC measurement system.

The measured spectrum is compared with th calculated one as shown in Fig.3.30, where black and red lines indicate the experimental spectrum and the fitted one with M=3.95, respectively. The calculated spectrum is in agreement with the measured one. The $\gamma$ ray flux thus obtained in each measurement is shown in Table3.12. The error was about 2% from the $\chi$ square fitting through all measurements.

Table 3.12: The $\gamma$ ray flux

| $E_{\gamma max}$ | the $\gamma$ ray flux |
|---|---|
| 10.5MeV | $1.11 \times 10^9$photons |
| 16.5MeV | $8.86 \times 10^8$photons |

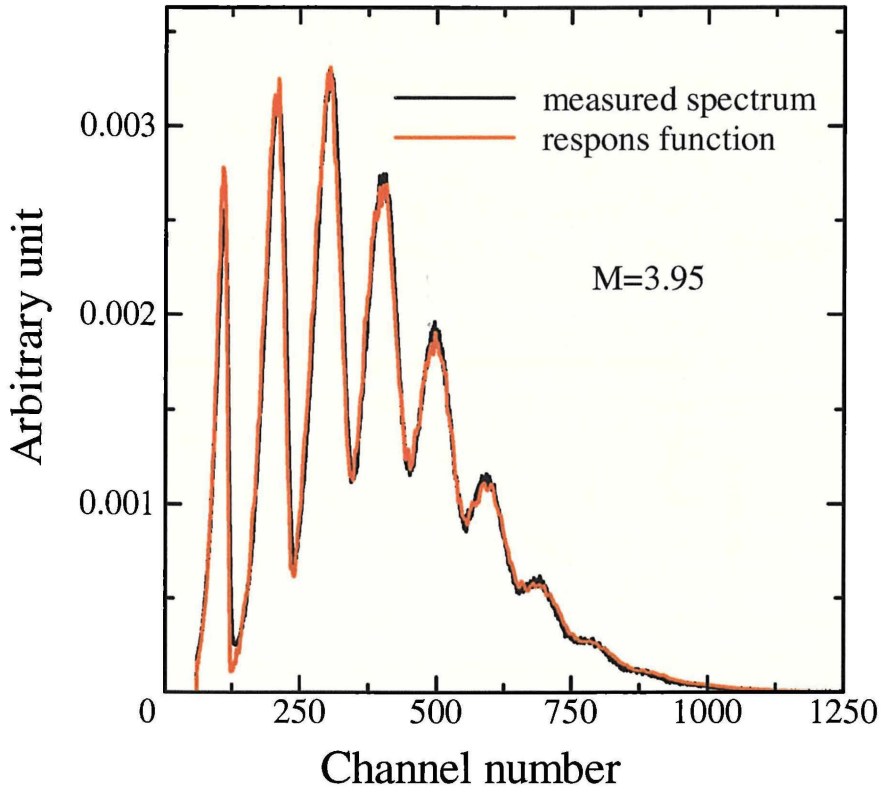


Figure 3.30: Comparison of the measured LCS $\gamma$-ray by the BGO detector with fitted one. average 3.95 photons per laser pulse

### 3.3.2 Energy distribution

The determination of the $\gamma$-ray energy distribution is important to compare the measured cross sections with the theoretical excitation curve. The $\gamma$-ray energy spread is expressed with a formula in eq.(2.5),

$$\Delta E_\gamma / E_\gamma = \left(\frac{2\Delta E_e}{E_e} + (\gamma\Delta\theta)^4\right)^{1/2} \tag{2.5}$$

$$\Delta\theta = (\theta_e^2 + \theta_c^2)^{1/2}$$

where $\Delta E_e$, $\theta_e$ ,and $\theta_c$ are the energy spread of the electron beam, the electron beam divergence, and a collimator half angle, respectively. Ohgaki *et al.* measured the photon energy spread using collimators with angle of 0.056mrad and 0.18mrad at TERAS. They showed that the calculated energy spread were in good agreement with the experimental values in the range of electron energy from 350MeV to 800MeV[39][40].

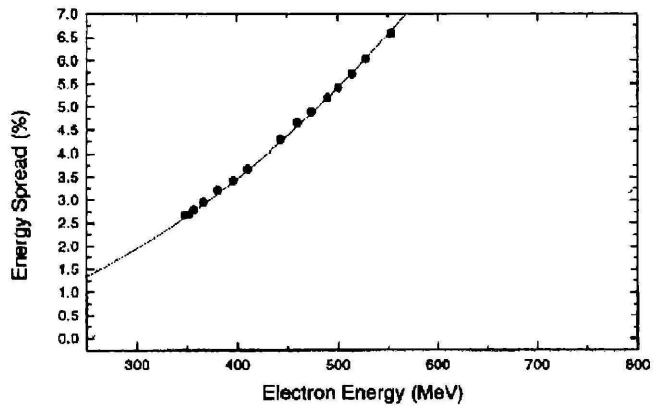


Figure 3.31: Measured photon energy spread as a function of the electron energy[40]

However in the present study the angle of the $\gamma$-ray collimator was not known exactly, and therefore the $\gamma$-ray energy distribution was measured at $E_{\gamma max}$=16.5MeV using a large NaI detector($\phi 8 \times 12 inch$). The setup of measurement is shown in Fig.3.32. We fitted the obtained $\gamma$-ray energy distribution with use of the formula given in eq.(2.5). Here the NaI response function was calculated using sg4 code [46](Fig. 3.33). The obtained NaI $\gamma$-ray spectrum is shown in Fig.3.34 together with the fitted spectrum.

In Fig.3.34, the black, red, and blue lines indicate the NaI $\gamma$-ray spectrum, fitting spectrum, and $\gamma$-ray energy distribution extracted from the red line, respectively. The fit was

performed by the stripping method.

Thus $\theta_c$ was determined to be 0.13mrad, using known values of $\theta_e$=0.115mrad and $\Delta E_e/E_e$ is $6.25 \times 10^{-6}$ as shown in Table 2.1 (Section 2.2). The energy spread is shown in Fig.3.35 together with the previous values measured by Baba *et al.*[45]. Their values are in agreement with our calculated curve. Since their optical system is different from that we used, some deviation exist.

The $\gamma$ ray energy spreads (FWHM) at 10.5MeV and 16.5MeV calculated from the above result are shown in Table3.13. Since the $\gamma$-ray energy distribution was asymmetrical to the energy, the $\gamma$-ray energy of the cross section was determined as the energy of the peak of the distribution, and the energy spread was defined as the FWHM.

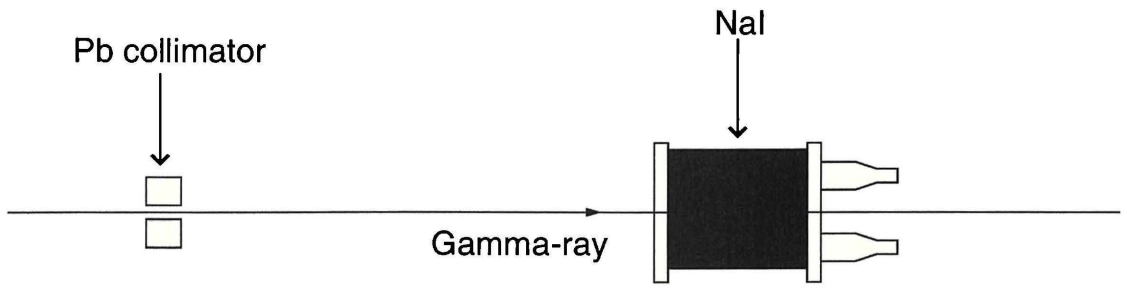


Figure 3.32: Experimental setup

Table 3.13: $\gamma$-ray energy spread

| electron energy | $E_{\gamma max}$ | energy spread | the peak of $E_\gamma$ | FWHM |
|---|---|---|---|---|
| 545MeV | 10.5MeV | 0.035 | 10.2MeV | +0.2/-0.2MeV |
| 685MeV | 16.5MeV | 0.054 | 16.0MeV | +0.3/-0.6MeV |

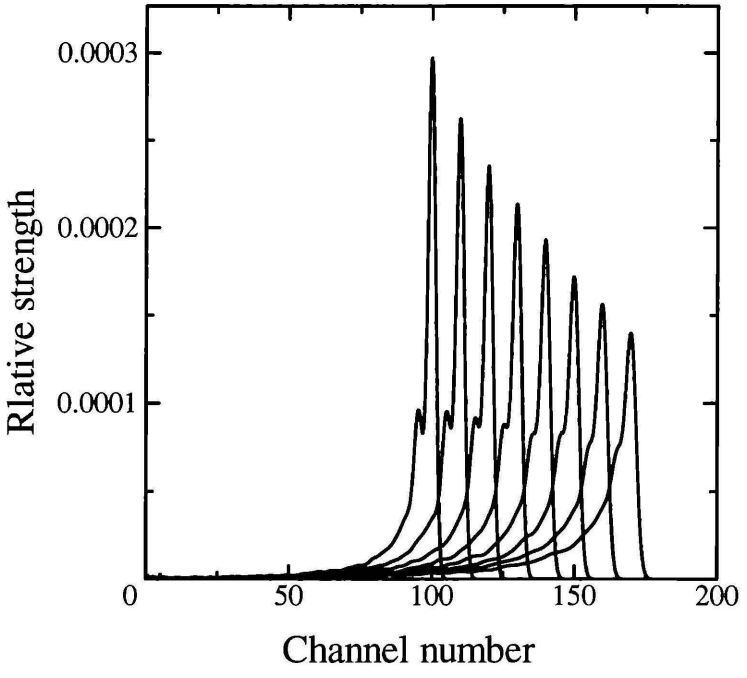


Figure 3.33: Response functions of the NaI(Tl) detector for discrete $\gamma$-rays between 10.0 and 17.0MeV.

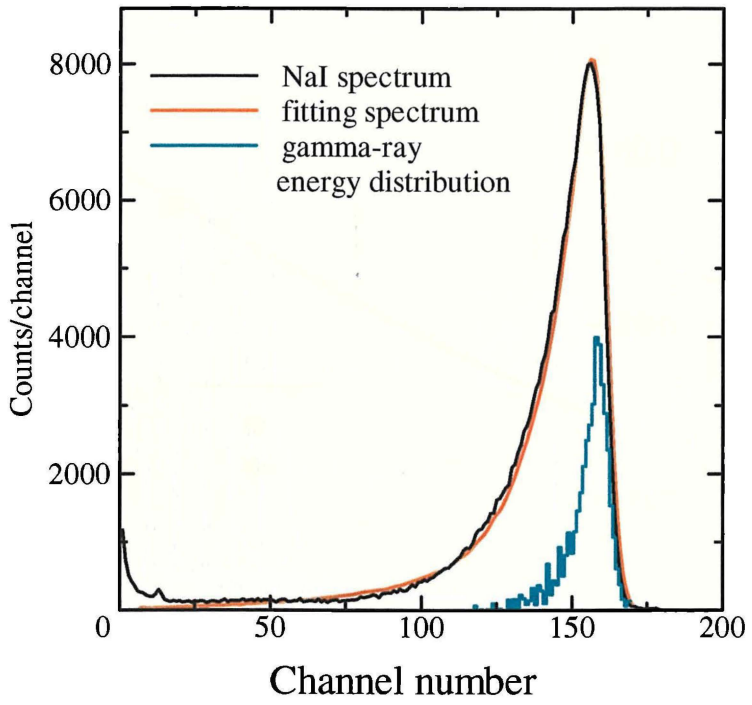


Figure 3.34: Laser Compton backscattering photon spectrum measured by the NaI(Tl) detector

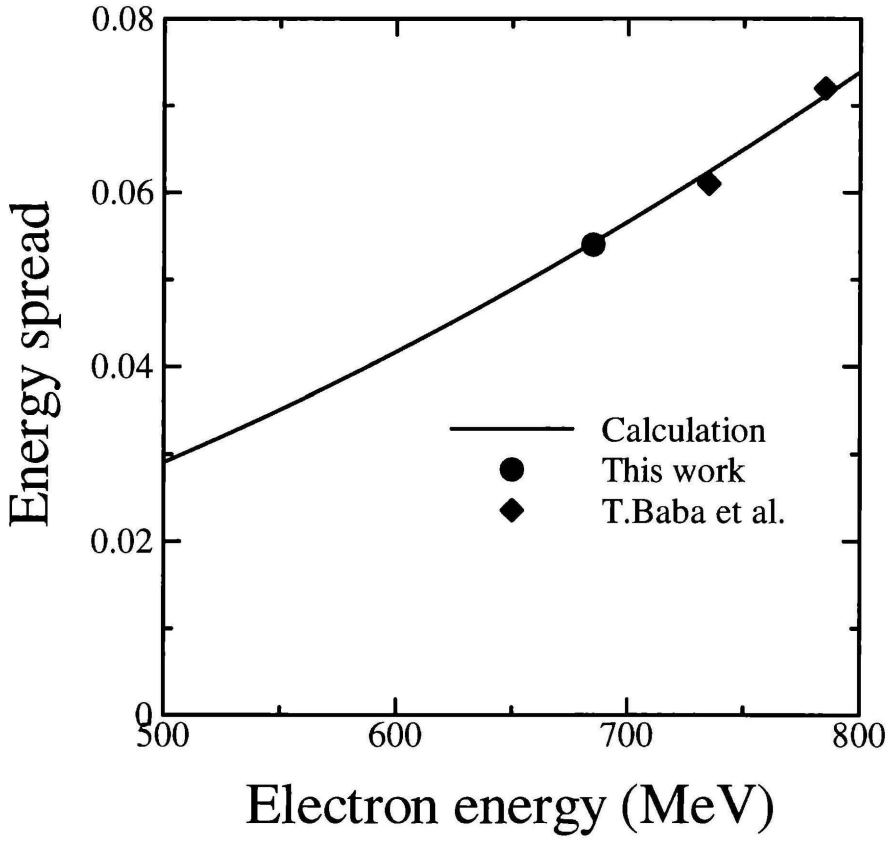


Figure 3.35: Measured $\gamma$-ray energy spread as a function of the electron energy

## 3.4 Results

The photodisintegration cross section was determined by the following formula.

$$\sigma = \frac{Y}{\varepsilon N L \phi} \tag{2.1}$$

Here Y is the number of events, $\varepsilon$ is the detection efficiency, L is the effective length and $\phi$ is the $\gamma$ ray flux. The obtained cross sections are shown in Table 3.14.

The various sources of the systematic error are considered. The estimated errors are given in Table 3.15.

Table 3.14: Cross sections of $^3$He photodisintegration

| | $E_\gamma$ | |
|---|---|---|
| Reaction | $10.2^{+0.2}_{-0.2}$MeV | $16.0^{+0.3}_{-0.6}$MeV |
| $^3He(\gamma,p)D$ | 0.77(5)mb | 0.65(5)mb |
| $^3He(\gamma,pp)n$ | 0.15(2)mb | 0.91(6)mb |
| $^3He(\gamma,p)D +^3 He(\gamma,pp)n$ | 0.92(5)mb | 1.57(8)mb |

(Note)Error includes both statistical and systematic errors.

Table 3.15: Source of systematic error

| elements of systematic errors | error |
|---|---|
| discernment of an event | negligible |
| $\gamma$ ray flux | about 2% |
| the number of $^3$He | 1% or less |
| effective length | about 1% |
| total | less than 3% |

# 4. Discussion and conclusion

## 4.1 Discussion

### 4.1.1 Comparison of the present results with previous experiments

The measured two-body breakup, three-body breakup and total cross sections of $^3$He photodisintegration are compared to previous experimental values and recent calculations as shown in Figs.4.1, 4.2, and 4.3.

#### Two-body breakup cross section

As mentioned before there is a large discrepancy of the two-body breakup cross section in the peak energy region between different data sets. The present experimental values are in agreement with lower values by Wolfli *et al.* and Ticcioni *et al.* as shown in Fig.4.1. While the latest data by Skopik *et al.* are about 40% larger than our data in the peak region of $E_\gamma = 10.5MeV$. The cross section by Skopik *et al.* was obtained by measuring the $\gamma$-ray angular distribution of the D(p,$\gamma$)$^3$He reaction using NaI(Tl) detectors. They obtained a large E2 cross section of 12(5)% of total cross section at $E_\gamma$=10.8MeV,which is much larger than that 2(3)% of the experiment by King *et al.*[47], who did the similar angular distribution measurement using same detectors. Therefore one possible reason of the large discrepancy is due to some problem in the $\gamma$-ray angular distribution measurement.

There is also a discrepancy between the present result and the data by Belt *et al.*, who measured the angular distribution of the emitted $^3$He particle from the H(d,$\gamma$)$^3$He reaction using a spectrometer. From the angular distribution they reported the multipole component higher than E2, which has not been confirmed by other group. Since they used the CH target and they could not distinguish the $^3$He particle from the H(d,$\gamma$)$^3$He from that of the $^{12}$C(d,$^3$He)$^{11}$B reaction, they might have the problem to select the true $^3$He event.

The present data are smaller than the data by Fetisov *et al.* by about 20-30%. One possible reason of the discrepancy is due to the cross section they used to obtain the $\gamma$-ray yield. Namely Fetisov *et al.* used a pulse ionization chamber to determine the incident $\gamma$-ray intensity and the calibration of the chamber was made by counting the yield of $^{11}$C produced by the $^{12}$C($\gamma$,n)$^{11}$C reaction. For this purpose they used the integrated cross section of $0.032(3)MeVb$[48], which is different from the latest value of $0.0250(1)MeVb$[49] by about 20%. Therefore, the cross section by Fetisov *et al.* should be decreased by 20%, and thus -obtained cross section is roughly in agreement with the present data.

### Three-body breakup cross sections

The present result at $E_\gamma$=16.5 MeV is in good agreement with all previous results as shown in Fig.4.2. While the result at $E_\gamma$=10.5MeV agrees with the data by Gerstenberg *et al.*, but slightly differs from the latest data by Faul *et al.*. Here it should be noted that the energy dependence of the three-body breakup cross sections measured by Berman *et al.* and Faul *et al.* is quite different from that obtained by Gerstenberg *et al.*. The reason of the discrepancy is not clear at the moment, and it should be clarified in the future experiment.

### Total cross sections

The present results at 10.5MeV and 16.5MeV are smaller than the data by Fetisov *et al.* by about 20% as shown in Fig.4.3, which may be due to the calibration error as discussed for the two-body disintegration. As one expects the present data at 16.5MeV agrees with the "derived" data by Faul *et al.*, which was obtained by using the three-body cross section by Faul *et al.* and the two-body cross section by Ticcioni *et al.*, since the present results for the two-body and three-body breakup cross sections agree with those by Ticcioni *et al.* and Faul *et al.*, respectively, as discussed before.
While at $E_\gamma = 10.5MeV$, our data is somewhat smaller than that of the "derived" data. This comes from the difference of the cross sections of three-body breakup between ours and Faul *et al.*, as discussed before.

## 4.1.2 Comparison of the present results with theoretical values

### Two-body breakup cross section

The present result is compared to the theoretical values by Schadow *et al.* as shown in Fig.4.1. Although our value at 16.5 MeV is roughly in agreement with the theoretical one, the value at 10.5MeV is quite different from the theoretical one. As discussed before one sees a remarkable potential dependence of the theoretical two-body breakup cross section in the peak region, but the peak heights are strongly dependent on the three-nucleon binding energies, which were obtained for the potentials employed. The obtained binding energies for Bonn A, Bonn B and Paris potentials are -8.28, -8.09 and - 7.37 MeV, respectively. The peak height decreases as the binding energy increases as shown in Fig.4.1. However, since the experimental value of the binding energy of $^3$He is -7.8 MeV, the discrepancy between the present result and the calculated one is not only due to the binding energy effect. It might be quite interesting to include the three-nucleon force in the calculation.

### Three-body breakup cross section

The present data are compared to the old calculation by Gibson *et al.* as shown in Fig.4.2. The measured cross section at 16.5MeV is almost in agreement with the calculated one,

and the small difference is considered to be due to the absence of the tensor force in the calculation. The effect of the tensor force is considered to increase the binding energy, the calculated cross section. Since the tensor force is included in the realistic NN force, it is highly important to perform the theoretical calculation using the realistic NN force. The cross section at 10.5MeV is quite different from the theoretical one. Since the calculated cross section near the threshold region depends strongly on the distortion of the emitted particles, it is necessary to make the detailed calculation taking into account the rescattering effect properly.

### Total cross section

The present data are compared to the theoretical values by Efros *et al.* as shown in Fig.4.3. Although our results at $E_\gamma$=10.5 and 16.5 MeV are somewhat smaller than the theoretical ones, the measured cross section at 16.5MeV clearly favours the calculated one with the three-nucleon forces. Hence it may indicate the important role of the three-body forces. There exists still about 13% discrepancy between the present data and the theoretical ones. It is certainly necessary to calculate the cross section further using modern realistic force such as AV18[50] and Nijm93[51] for understanding the details of the discrepancy.

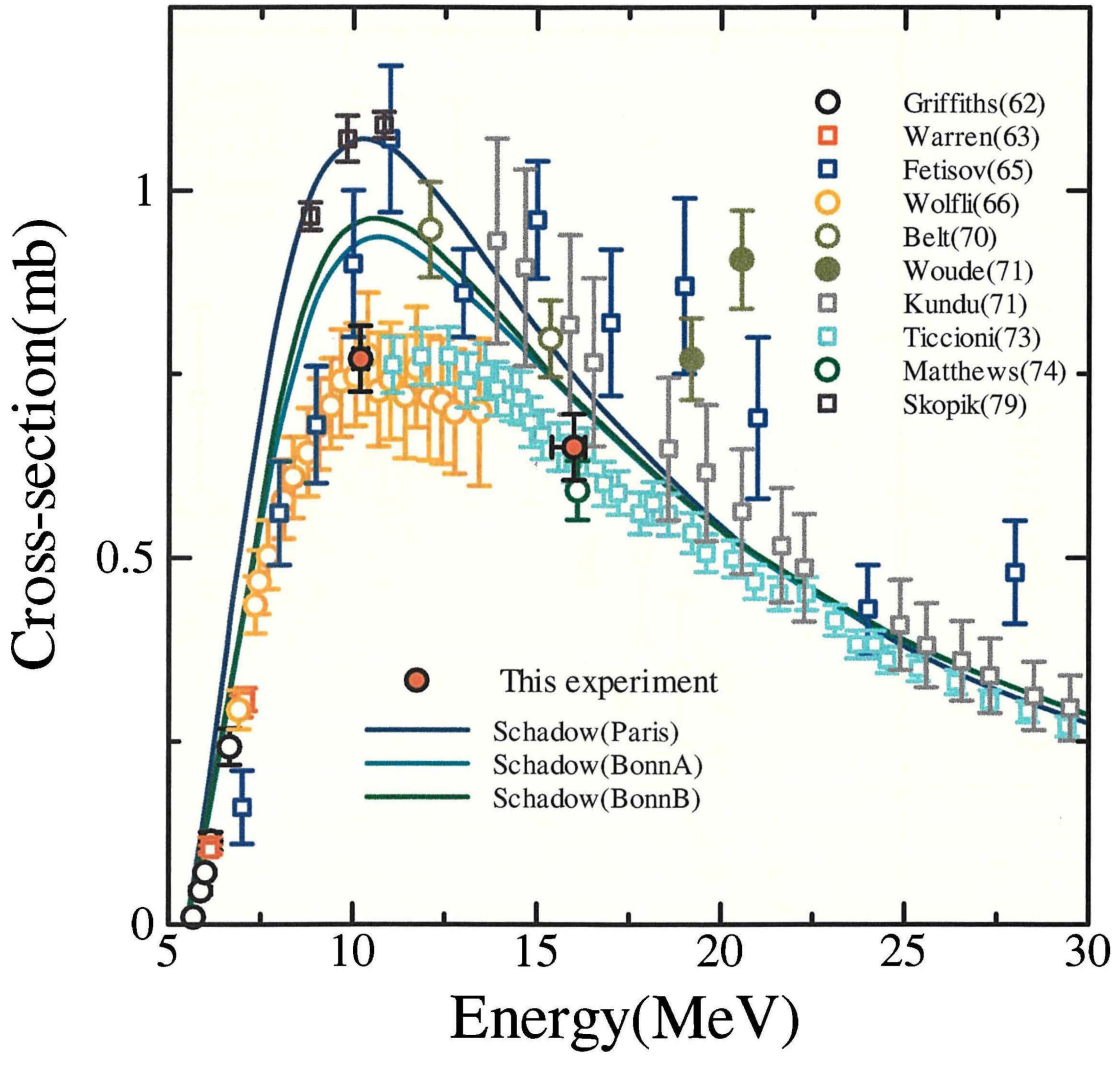


Figure 4.1: Measured and calculated cross sections of the $^3$He($\gamma$,p)d reaction

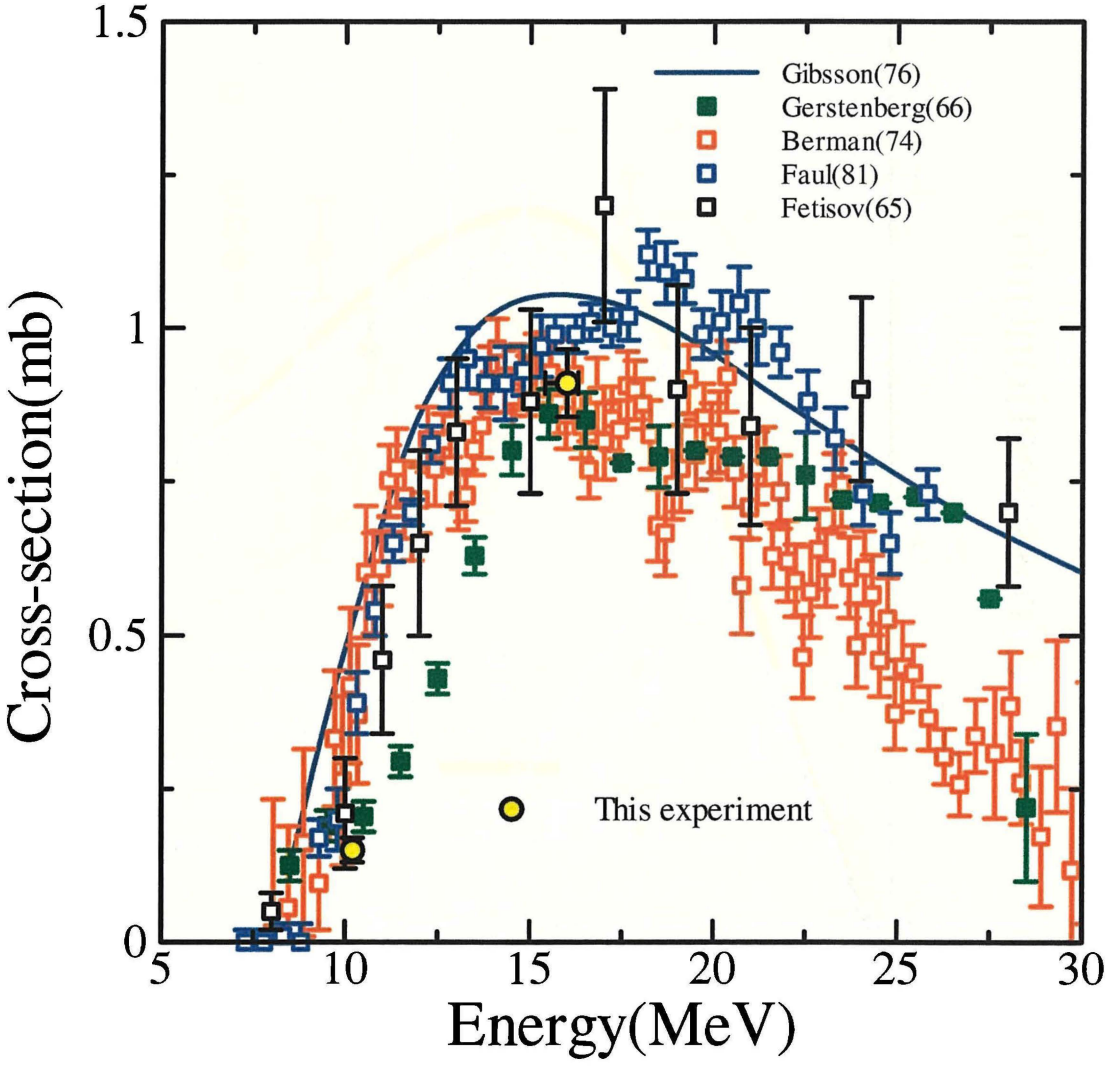


Figure 4.2: Measured cross sections of the $^3$He($\gamma$,pp)n reaction

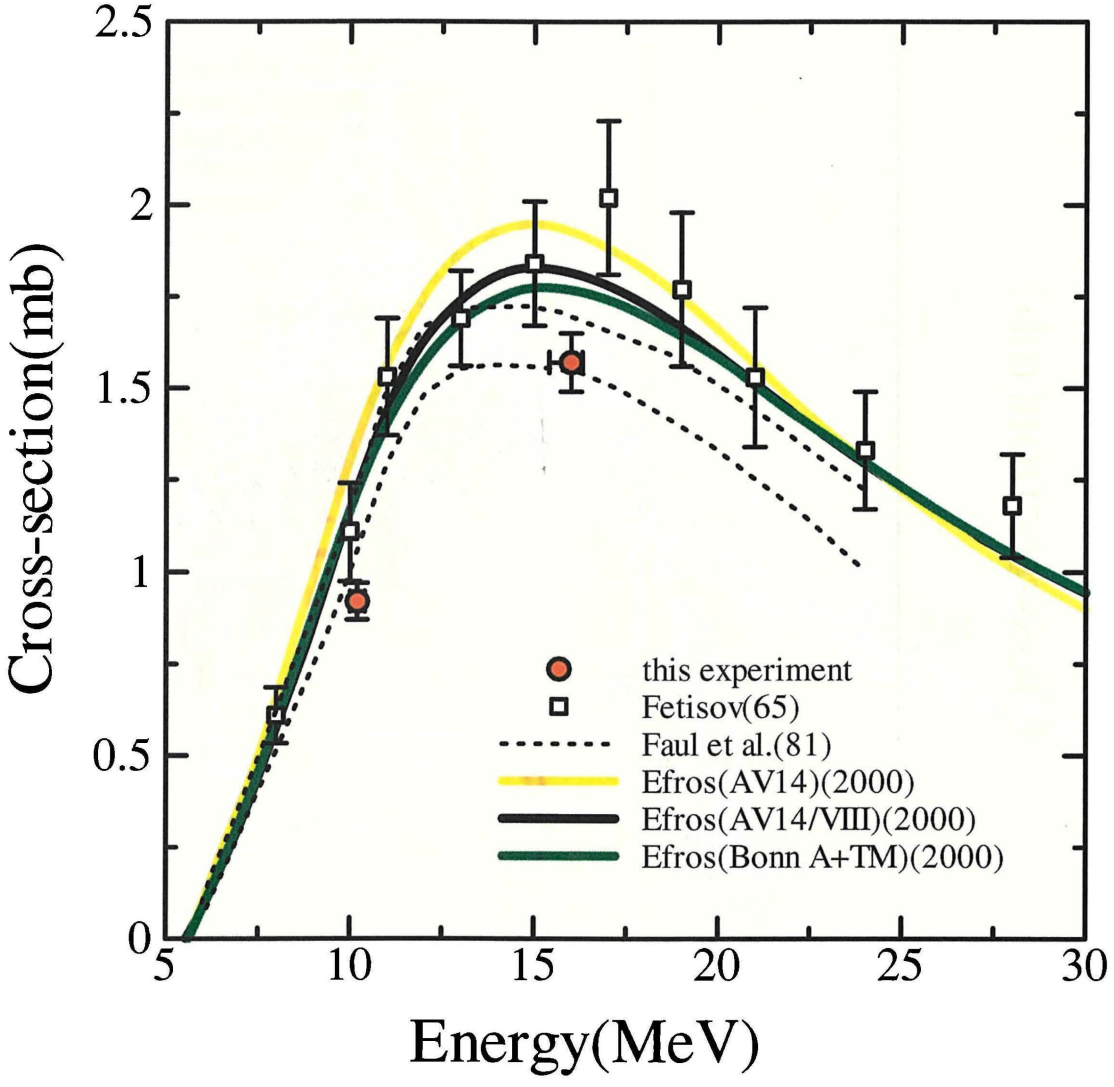


Figure 4.3: Measured and calculated total cross sections of $^3$He photodisintegration

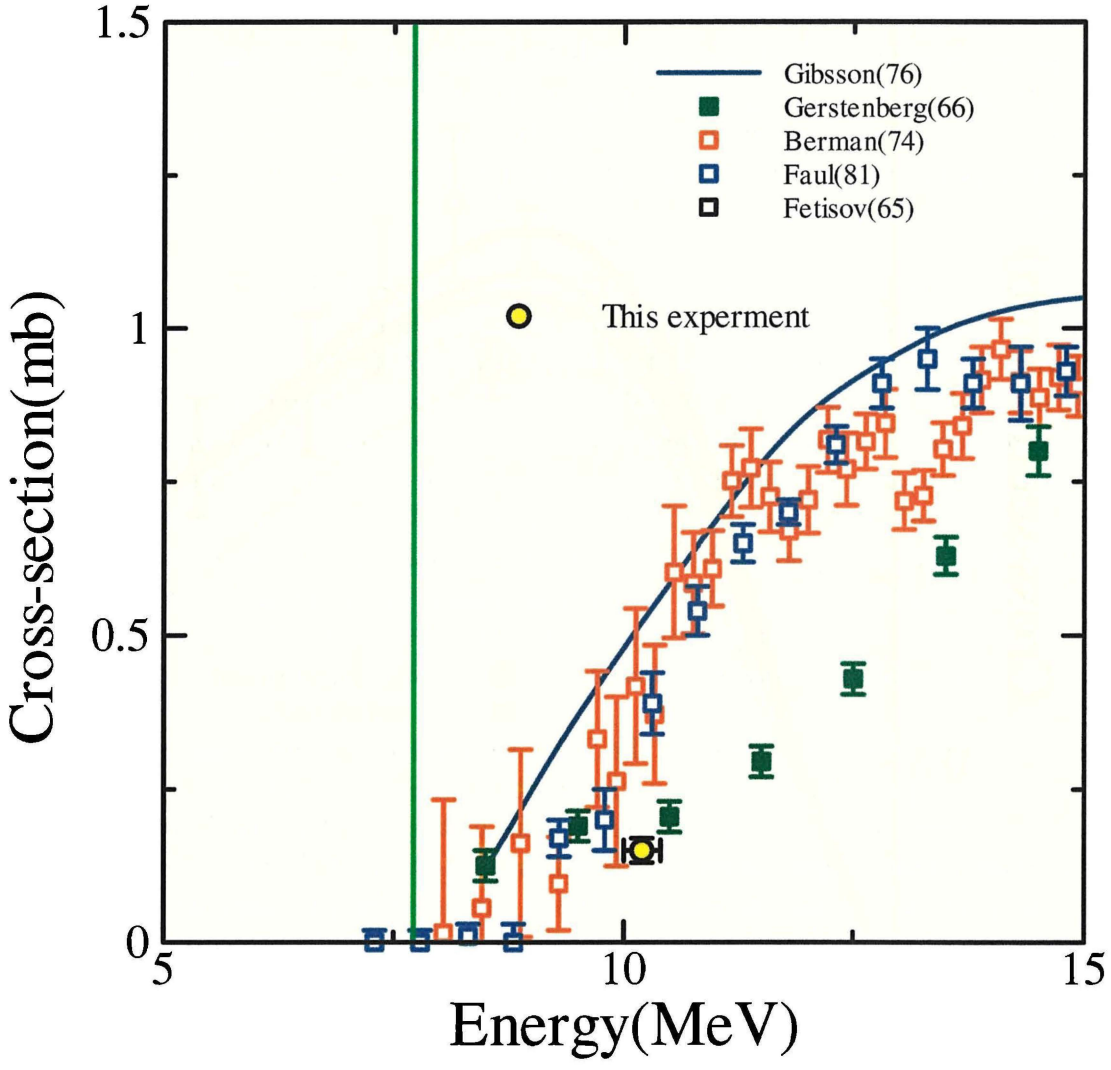


Figure 4.4: Measured cross sections of the $^3$He($\gamma$,pp)n reaction near threshold region. A green line expresses threshold value(7.718MeV) of $^3$He($\gamma$,pp)n

## 4.2 Conclusion

The two-body breakup and three-body breakup photodisintegration cross section of $^3$He have been measured accurately using the newly developed time projection chamber and the laser Compton backward-scattering photon beams. The measurements have been made at the $\gamma$-ray energies of 10.5 and 16.5 MeV, since the cross sections for the two-body breakup and total photodisintegration of $^3$He are predicted to have the maximum values at these energies and to be sensitive to the potentials employed in the calculation. The experimental data for two-body breakup, so far measured, show a large discrepancy between the different data sets and have a large error. Hence one could not use these data to discriminate the theoretical models.

Characteristic points of the present experimental methods are as follows. First, since the TPC contains an active gas target of $^3$He, we could detect very low energy charged particles from the photodisintegration of $^3$He with almost 100% detection efficiency a large acceptance of $4\pi$. Hence the two-body and three-body breakup reaction could be simultaneously measured. Second, we used the quasi-monochromatic $\gamma$-rays whose energy was variable and it's feature was very important for carrying out the measurement at particular energies of 10.5 and 16.5MeV in this study. Third we detected the tracks of the charged particle using the TPC and the LCS photon beam was well-collimated and thus our method provided high capability for distinguishing true events from background. Fourth, the absolute flux of the LCS photon was measured precisely using $\gamma$-ray detectors. These points were crucial to precisely determine the cross sections of $^3$He photodisintegration.

In analysing the data taken by the TPC we used the trajectories and the pulse heights of the charged particles emitted in the photodisintegration of $^3$He. The efficiency of the TPC was determined by fitting the pulse peak histogram with the Monte Carlo simulation. The number of the target nuclei was determined measuring the temperature and pressure of $^3$He. The photon flux was obtained by fitting the pulse height spectrum of the BGO counter with the response function. Thus we obtained the two-body breakup, three-body breakup and total cross sections of $^3$He photodisintegration at $E_\gamma$=10.5MeV and 16.5MeV with small error of $\sim$6%.

The present data for the two-body breakup is in good agreement with the lower values of the previous data, and thus we could solve the long standing problem of the two-body breakup cross section which the total cross section is about 20% smaller than the values measured previously and one of the possible reason of the discrepancy is due to the calibration error in the previous study.

The present results for the two-body, three-body and total cross sections are compared to the theoretical calculations quite recently performed using realistic NN interactions. From the comparison we can draw the following considerations. First, the result of the total cross

section is about 13% smaller than the theoretical one by Efros *et al.*, while the present result favours the theoretical value with the three-nucleon forces. It is important to calculate the cross section using modern realistic force such as AV18 and Nijm93 for understanding the origin of the discrepancy. Second, the result of the two-body breakup cross section at 16.5MeV is roughly in agreement with the theoretical one by Schadow *et al.*, but the value at 10.5MeV deviates considerably 20-40% from the theoretical ones. Since the property of the ground state, such as the binding energy, has not been well described by the theoretical calculation, we strongly encourage theorists to make progress in the calculation of the two-body photodisintegration cross section of $^3$He.

Concerning the three-body breakup is higher appreciated, we also encourage theorists to make a new calculation using realistic potentials, which can be compared with the present measurement.

# Bibliography


[1] L.D.Knutson,Nucl. Phys. A631(1998)9

[2] H. Kamada,Ruhr Univ.,lecture note,Summer school in Kijimataia(1999)

[3] R. B. Bösch, J. Lang, R. Müller, and W. Wölfli, Phys. Lett. 8,120(1964); Helv. Phys. Acta 38, 753 (1965).

[4] R. Kosiek, D. Müller, and R. Pfeiffer, Phys. Lett. 21, 199(1966).

[5] D.D.Faul,B.L.Berman,P. Meyer and D. L. Olson,Phys. Rev. C,24,849(1981)

[6] D. M. Skopik, D. H. Beck, J. Asai, and J. J. Murphy II, Phys. Rev. C 24, 1791 (1981).

[7] G. Mitev, P. Colby, N. R. Roberson, and H. R. Weller, Phys. Rev. C 34, 389 (1986).

[8] J. Mösner, K. Möller, W. Pilz, G. Schmidt, and T. Stiehler, Few-Body Syst. 1,83 (1986).

[9] G.M.Griffiths,E.A.Larson and L.P.Robertson,Can.J.Phys.,40,402(1962)

[10] J.B.Warren et al.,Phys. Rev.,132,1691(1963)

[11] V.N.Fetisov, A.N.Gorbunov and A.T. Varfolomeev. Nucl. Phys., 71, 305(1965); A.N.Gorbunov and A.T. Varfolomeev, Phys. Lett.,11,137(1964)

[12] W.Wolfli et al.,Helv. Phys. Acta,40,964(1967);W.Wolfli et al.,Phys. Lett.,22,75,(1966)

[13] B.D. Belt et al.,Phys. Rev. Lett.,24,20,1120(1970)

[14] A. van der Woude et al.,Phys. Rev. Lett.,26,909(1971)

[15] S.K.Kundu, Y. M. Shin and G. D. Wait,Nucl. Phys. A,171,384(1971)

[16] G. Ticcioni, S.N.Gardiner, J. L. Matthews and R. O. Owens,Phys. Lett. B,46,369(1973)

[17] J.L.Matthews et al.,Nucl. Phys. A,223,221(1974)

[18] D.M.Skopik et al., Pys. Rev. C,19,601(1979)

[19] H. M. Gerstenberg and J. S. O'Connell, Phys. Rev.,144,834(1966)

[20] B. L. Berman, S.C.Fultz and P.F.Yergin, Phys. Rev. C,10,2221(1974)

[21] L. D. Faddeev, Sov. Phys. JETP 12,1014(1961)

[22] E. O. Alt, P. Grassberger and W. Sandhas, Nucl. Phys. B2, 167(1967)

[23] W.Sandhas, W.Schadow,et.al., Nucl. Phys. A631(1998)210c; W.Schadow and W.Sandhas, Nucl. Phys. A631(1998)588; W.Schadow and W.Sandhas, Phys. Lett. C, vol.55,No.3,1074,1997;

[24] V.D.Efros,W.Leidemann,and G.Orlandini,Nucl. Phys. A631 (1998) 658c; V.D.Efros,W.Leidemann,and G.Orlandini, Phys. Lett.B408(1997)1-6

[25] Yu. I. Fenin and V.D.Efros, Sov. J. Nucl. Phys. 15, 497 (1972)

[26] I. M. Barbour and A. C. Phillips, Phys. Rev. C,Vol.1,No.1,165(1970)

[27] I. M. Barbour and J. E. Hendy, Phys. Lett. 38B,151(1972)

[28] G. Barton, Nucl. Phys., A104, 289(1967)

[29] B.F.Gibson and D.R.Lehman,Phys. Rev. C,vol.11,No.1,29,1975

[30] B.F.Gibson and D.R.Lehman,Phys. Rev. C,Vol.13,No.2,477(1976)

[31] W.Schadow, O.Nohodani, and W.Sandhas, Phys. Rev. C, 63, 044006(2001)

[32] M. Lacombe et al.,Phys. Rev. C21,861(1980)

[33] R. Machleidt, Adv. Nucl. Phys. 19, 189 (1989)

[34] V.D.Efros,W.Leidemann,G.Orlandini,and E.L.Tomusiak,Phys. Lett.B484(2000)223

[35] R.B.Wiringa, R.A. Smith, and T.L. Ainsworth, Phys. Rev. D17, 768(1978)

[36] R.B.Wiringa, Phys. Rev. C43, 1585(1991)

[37] S.A. Coon, M.D. Scadron, P.C. McNamee, B.R. Barrett, D.W.E. Blatt, B.H.J. McKellar, Nucl. Phys. A 317 (1979) 242; S.A. Coon, W. Glockle, Phys. Rev. C 23 (1981) 1790.

[38] E.Feenberg and H.Primakoff. Phys. Rev.,73,449(1948); R.H.Milburn, Phys. ReV. Lett., 10, 75(1963); F.R.Arutyunian and V.A. Tumanian, Phys. Lett., 4,176(1963)

[39] H.Ohgaki et al., IEEE Trans. Nucl. Science,38,2,386(1991)

[40] H.Ohgaki et al., Nucl. Inst. Meth. A455,54-59(2000)

[41] N.Tsoulfanidis, Measurement and Detection of Radiation, Hemisphere Publication Corp.(1983)

[42] B.Weissman et al., Nucl. Phys. A174 129(1971)

[43] H.H. Andersen and J.F. Ziegler, The Stopping and Ranges of Ions in Matter vol.3

[44] Toshiteru Kii, doctor theses,Tokyo Institute of Technology(1998)

[45] Takashige Baba, doctor theses,Tokyo Institute of Technology(1999)

[46] Toshirou Ohsaki,doctor theses,Tokyo Institute of Technology(1998)

[47] S.E.King et al., Phys. Rev. Lett.,51,977(1983); S.E.King et al., Phys. Rev. C,30,21(1984); S.E.King et al., Phys. Rev. C,30,1335(1984)

[48] W.C.Barber et al., Phys. Rev. ,Vol.98,No.1,73(1955)

[49] W.E.DEL BIANCO, Phys. Rev.,126,709(1962)

[50] R.B. Wiringa et al, Phys. Rev. C51, 38 (1995)

[51] V.G.J.Stoks et al, Phys. Rev. C49, 2950 (1994)

# Appendix A

# Development of multipass system

## A.1 Introduction

The laser Compton-backscattering (LCS) photon beam has many characteristic features for studying photodisintegration of a nucleus, such as quasi-monochromatic nature and linearly (circularly) polarization. The intensity of the LCS $\gamma$-ray, however, is not so high. Hence it is quite important to make an effort to increase the intensity. The laser Compton backscattering $\gamma$-rays are generated by the head-on collision of the laser photons with relativistic electrons. Usually the laser photons which do not collide with electrons (99.999% of incident photons in TERAS) are not re-used. This system is called as the single pass system.

The multi pass system aims at reusing the non-interacting photons for increasing the LCS $\gamma$ ray flux. Namely with the use of the system one can make several collisions between electrons and laser photons within the photon cavity installed at the electron beam tube. The cavity has high reflectance mirrors.

In the present work we have newly developed the multi-pass system at the electron storage ring TERAS and studied the performance of the system.

### A.1.1 History of the development

For increasing the $\gamma$ ray flux, from the second half of the 1970s to the first half of the 1980s, LADON group at Frascati National Laboratories (FNL) had developed the system like the multi pass system [1][2].

Their idea was to extend the internal cavity of the laser so that it might sandwich an whole electron beam line and might make head-on collisions of laser photons with electrons within the internal cavity. They extended the internal cavity length up to 17.5m, and they tried to increase the $\gamma$ ray flux. However so far there is no published report on the experimental results.

Recently a new idea using a super cavity (the high finesse Fabry-Perot interferometer) has been tested at the Institute for Laser Technology(ILT)[3]. Their plan is to generate intense $\gamma$-rays or X-rays, by installing a compact super cavity to accumulate laser photons and making collisions of the accumulated photons with electrons. J.P.Jorda *et al.* at Jefferson Lab. have succeeded in accumulating laser photons in a super cavity[4].

Although extensive studies have been carried out to increase the LCS photons by making multiple collisions of a laser photon with electron beams as discussed above, no one has ever succeeded to obtain the intense LCS $\gamma$-rays with use of these methods. Here it should be noted that since the above two-cavities studied by ILT and Jefferson Laboratory require the mode-locking laser, one can not get pulsed LCS $\gamma$-rays. In order to generate the pulsed $\gamma$-rays one has to use a pulsed laser. Hence in this study we have developed the cavity, which can be used for the pulsed laser.

### A.1.2 Our design

The cavity is installed at the electron beam tube at TERAS to make head-on collisions of laser photons with electrons. The advantage of head-on collisions is much longer interaction length of laser photons and electrons than aslant collisions.

In order to realize the multipass system there are following problems.

1. Cavity length

Control of laser light is so easy that the cavity length may be short. However, the installation position of the cavity depends on the available space in TERAS. Due to the geometry of the electron beam line we use, the length of the cavity must be at least more than 5m.

2. Accuracy of control of the cavity mirror

The angle resolution required for generating $\gamma$-rays with the singlepass system is $\sim 10^{-3}$rad. However, in the multipass system, since a declination of the angle is accumulated due to multi reflection of laser light within the cavity, the required angle resolution is $\sim 10^{-4}$rad for several round trips of laser photon and $\sim 10^{-5} rad$ for several tens round trips of laser photon.

3. Damage of the mirror by laser beam and synchrotron orbital radiation

In order to reflect the laser light at the mirror with high reflectance, we employed a multi-layer dielectric mirror suitable for the wavelength of the laser system. In order to generate the high intensity $\gamma$ rays, the high power laser is used. Therefore, the mirror must be strong against the amplified intense photon and synchrotron orbital radiation. Also the reflectance

and other characteristics of the mirror should not be affected by the intensity of the light.

The cavity length was determined to be 6m from the limitation of the space in TERAS. The diameter of a mirror was 50mm$\phi$. In order to avoid the attenuation of the laser power in air, cavity mirrors were installed in a vacuum chamber (called the mirror chamber), and the mirror chamber was connected to an electron beam line with gate valves. We could control the installed mirror with the angle resolution of $5 \times 10^{-5} rad$. We did not worry about the damage of the mirror by laser light at this time, since the output power of the laser we used was the continuous wave (CW) laser (not a pulsed laser) and was about 2W. Here it should be mentioned that we can get now a mirror which can be used for intense pulsed laser. The damage by synchrotron orbital radiation occurs when the energy per unit area on a mirror exceeds some limit. We can get rid of this problem by using the mirror with high reflectance for the particular monochromatic wavelength of the laser. Thus most of synchrotron orbital radiation light was made to transmit the mirror. It is needless to say that a gate valve was closed to intercept the synchrotron orbital radiation, when we did not make an experiment.

In the following Section,Details of the optical system, Mirror chamber and results of the test experiments are described in the Section A.2, A.3 and A.4, respectively.

## A.2 Optical system

### A.2.1 Principle

The outline of the optical system is briefly described using Fig.A.1. Two mirrors, M1 and M2, with different focal distance are placed so that the focus position of the M1 may coincide with that of the M2, where electron beams are most converging. Laser beam is introduced into the cavity through a hole of the M1 so that its focus position may coincide with the focal position of mirrors. Incident laser photons are reflected at the M2, and some laser photons travel back and forth within the cavity and others go away through the hole. While repeating round trips, the laser photons make collisions with electrons several times. On the other hand, the size of the laser beam spot increases and the laser beam escapes from the optical system.

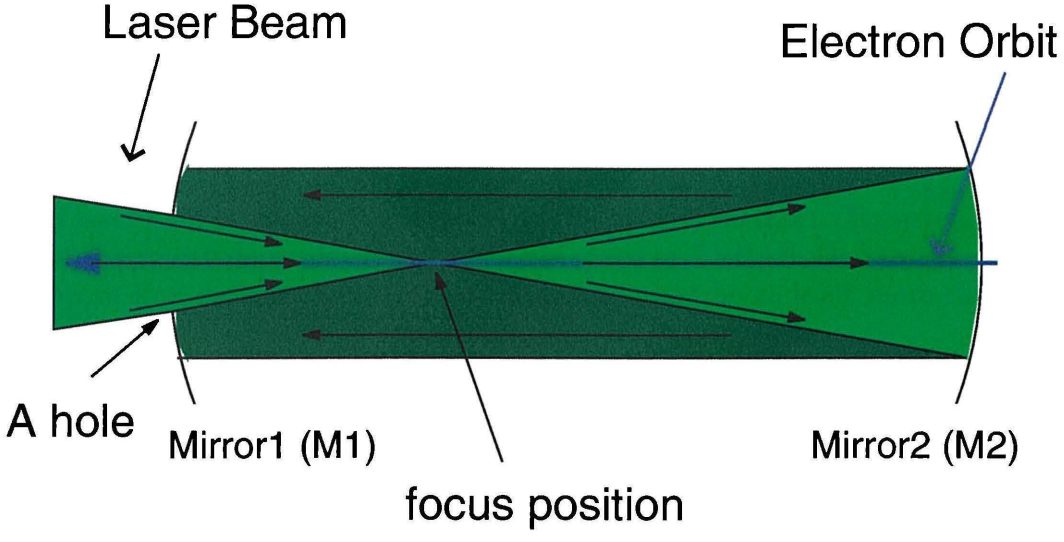


Figure A.1: Optical system

### A.2.2 Details of the optical system

A schematic view of the mirror chamber is shown in Fig. A.2. The distance between two mirrors of M1 and M2 is 6m. In the beam line we use, the position of most converging electrons is 2m away from the M1. While the focal distance of the M2 is 4m. With the above-mentioned geometrical condition we calculated the laser photon track in the mirror chamber using a home-made simulation code. Here the laser photon beam with the diameter of 3mm is introduced into the cavity. The result is shown in Fig.A.3, where z is the center axis of the two mirrors and y is the axis on the mirror perpendicular to the z axis. The positions of M1 and M2 are z=0 and z=6m, respectively, and the electrons move from the right to the left direction on the z-axis.

As shown in Fig.A.3 the size of the laser beam becomes large as the number of the intersection of the laser beam at the focus point of z=2m increases. Namely the size becomes 6mm$\phi$ when the incident laser beam of 3mm$\phi$ is reflected by the M2. In the present case when the number of the interaction is about 5, the size of the reflected laser beam becomes larger than that of the mirror. In order to make 10 collisions between the laser photons and electrons using the system, the size of the incident laser beam should be $50\mu m$, which is very difficult to obtain.

Then the laser power in the cavity was calculated as a function of the transmissivity of the mirror system. Here the calculation was made assuming the Gaussian distribution for the space distribution of the number density of the incident laser photons on the xy plane. The calculated result is shown in FigA.4 and it indicates that the internal laser power becomes maximum when 89.0% of incident laser power is introduced into the cavity through the hole. 44.0% of incident laser power escapes from the hole after first reflection at the mirror, but the remaining 46.4% travels back and forth within the cavity 4 times. As a result, the internal laser power becomes 2.75 ($= 0.464 \times 4.0 + 0.890$) times of incident laser power. If the internal laser power is fully used for generating LCS $\gamma$-rays, the number of $\gamma$ photons will increase by 2.75 times compared to that obtained by the singlepass. The relation of the round trip number and internal laser power is shown in Fig.A.5. This optical system aims at increasing the $\gamma$-ray flux by a factor of 2-4.

This optical system is not sensitive to the distance between mirrors. This was checked by calculating the focal position assuming that the distance between two mirrors is 5.95m instead of 6m, and the result is shown in Fig. A.6. One can hardly find the change of the focal position. Because of this character one can easily adjust the optical system.

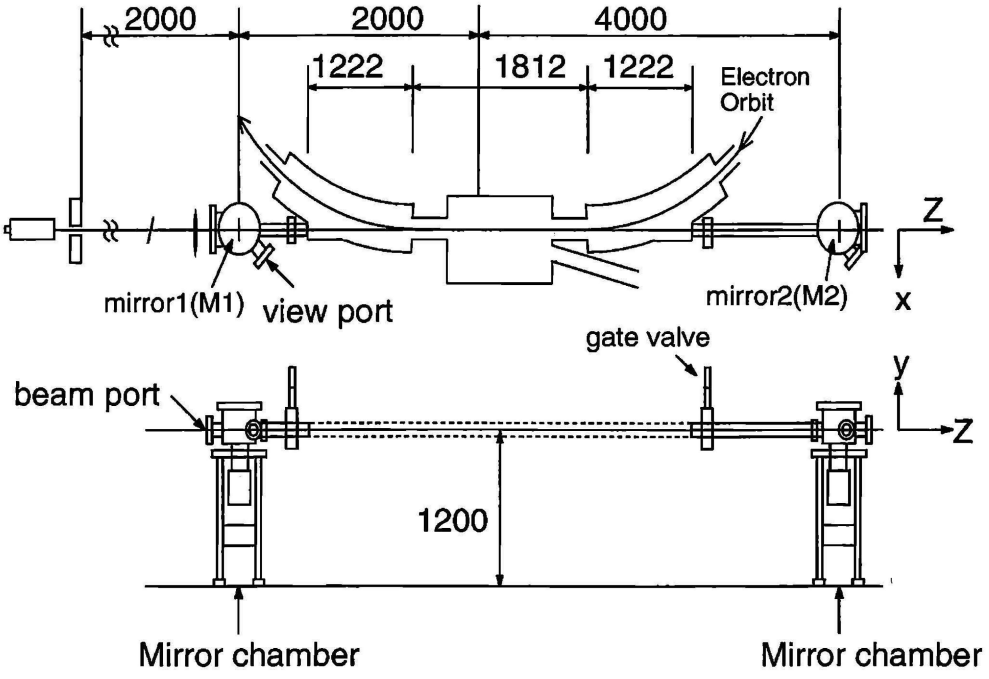


Figure A.2: A schematic view of the mirror chambers

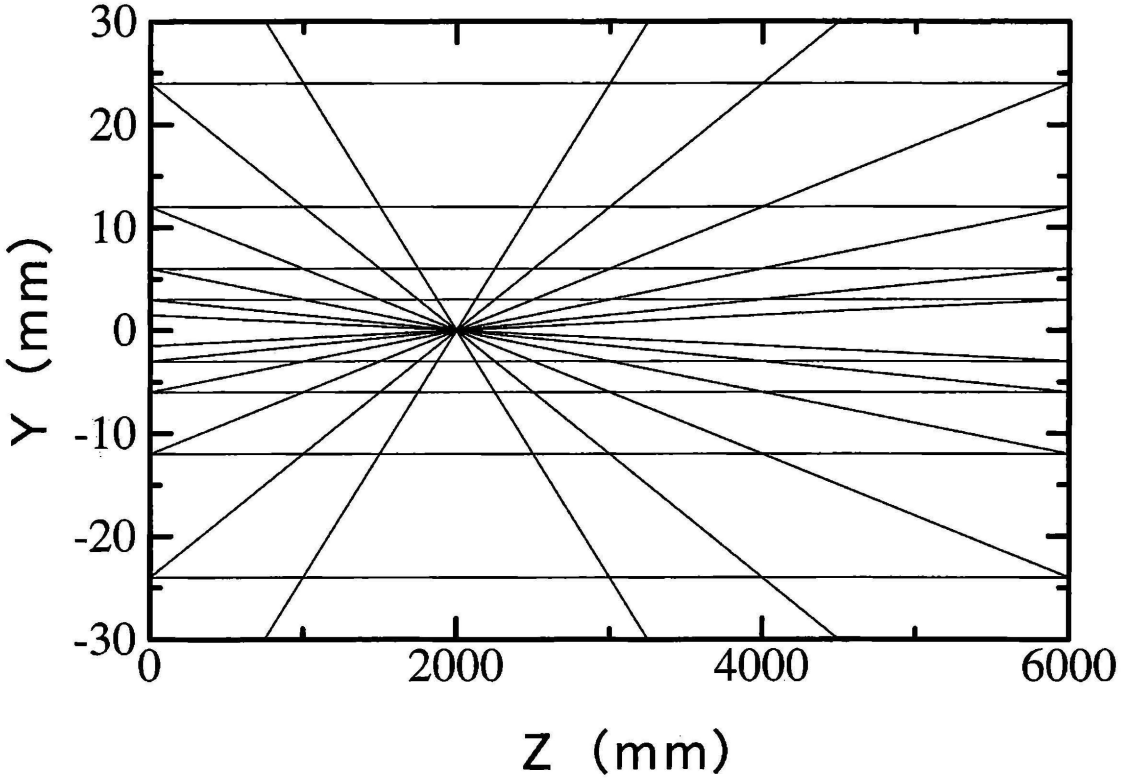


Figure A.3: Calculated laser photon track in the mirror chamber

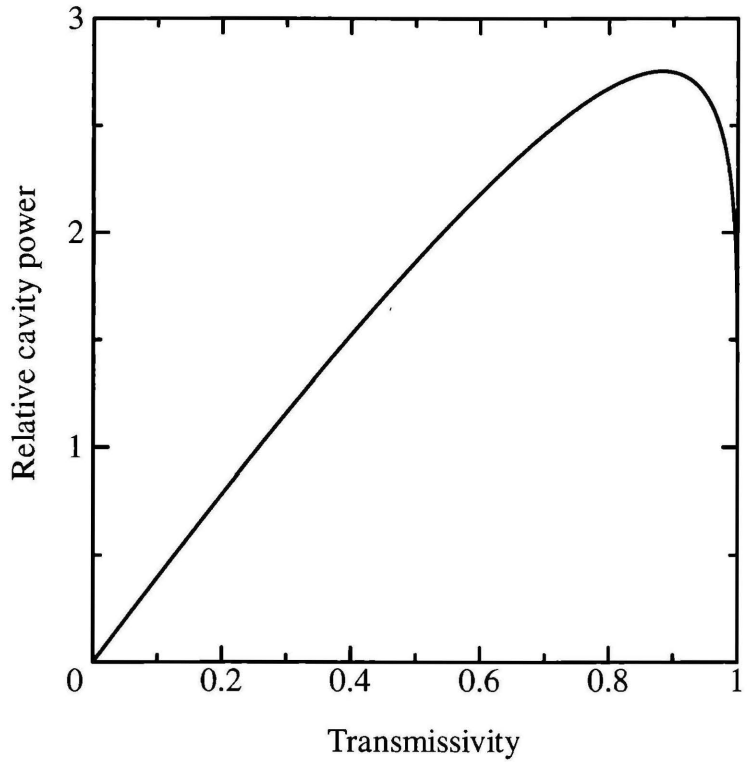


Figure A.4: Transmissivity v.s. relative cavity power

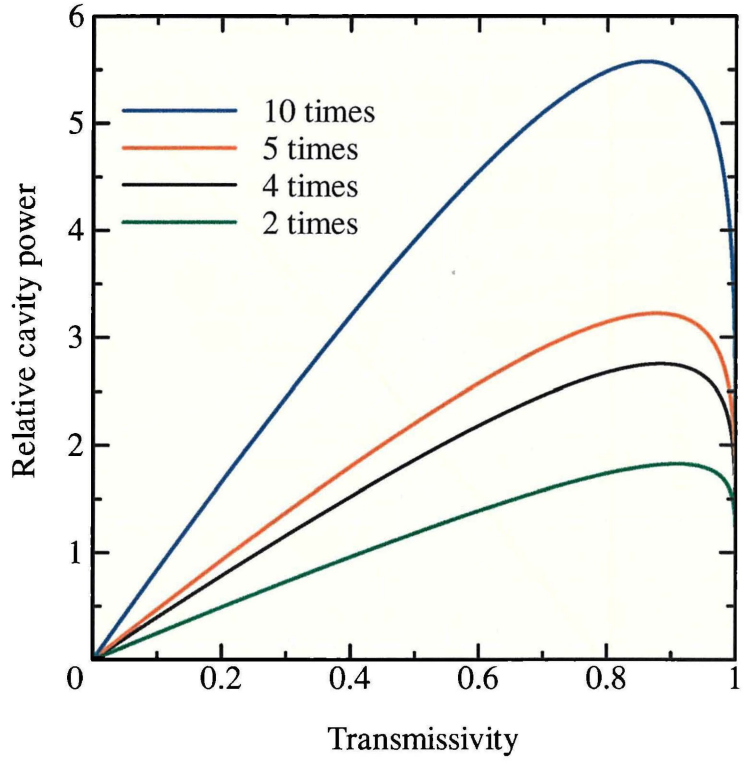


Figure A.5: Dependence of relative cavity power on the transmissivity and on the round trip number

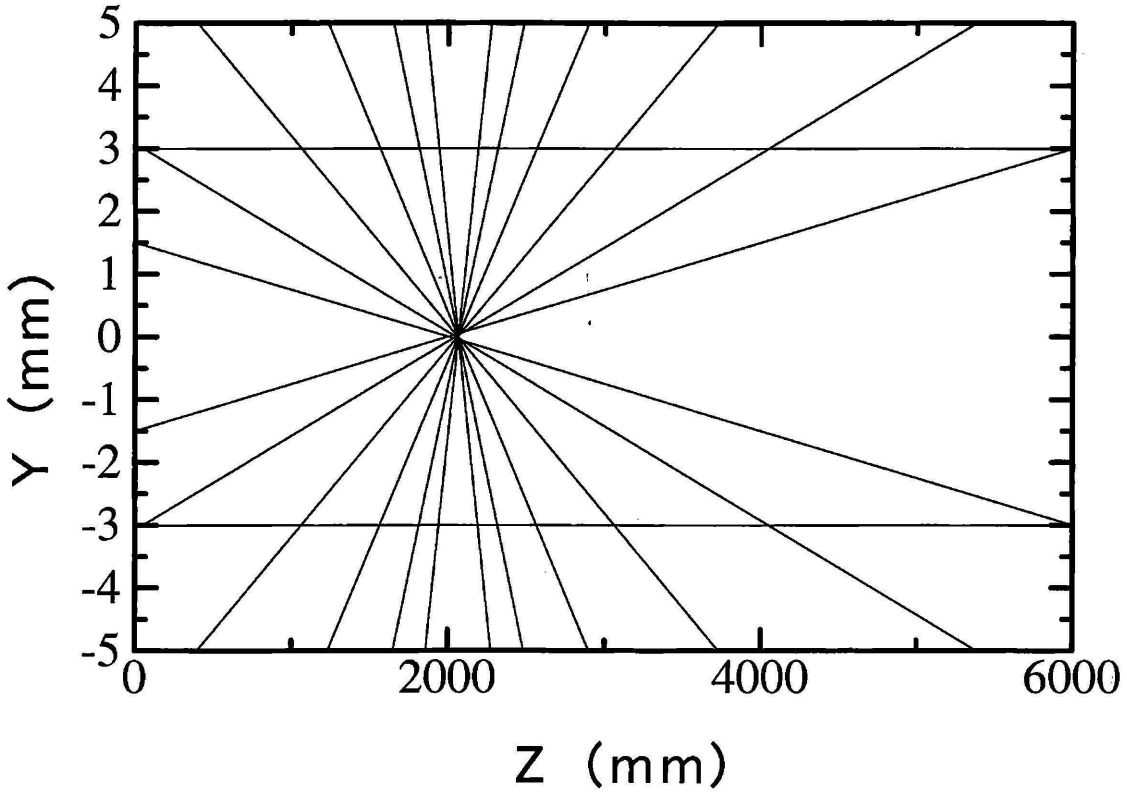


Figure A.6: Calculated focal position when the distance between two mirrors is 5950mm

## A.3 Mirror chamber

A mirror chamber is placed on the TERAS electron beam line through a gate valve (Fig.A.2). One can move the mirror in the mirror chamber to x, y, and z directions manually from outside the chamber and also revolve the mirror automatically on the xy plane. The angle resolution is $50\mu rad$. One can also record the position and the inclination of the present mirror. A beam port is used to inject the laser beam into the cavity. A view port is used to monitor the situation inside the chamber. The specification of the mirror chamber is given in Table A.1.

Table A.1: The specification of a mirror chamber

| The diameter of installed mirror | | 50mm dia. |
|---|---|---|
| x, y advancing-side-by-side shaft | actuation approach | manual |
| | actuation range | $\pm 5mm$ |
| | actuation resolving power | 0.01 mm |
| x, y revolving shaft | actuation approach | remote control |
| | actuation range | $\pm 3^o$ |
| | actuation resolving power | below 1/6000 rad(in practice $50\mu$rad) |
| | reproducibility | below 1/2000 rad |
| z advancing-side-by-side shaft | actuation approach | manual |
| | actuation range | $\pm 20mm$ |

## A.4 Measurements

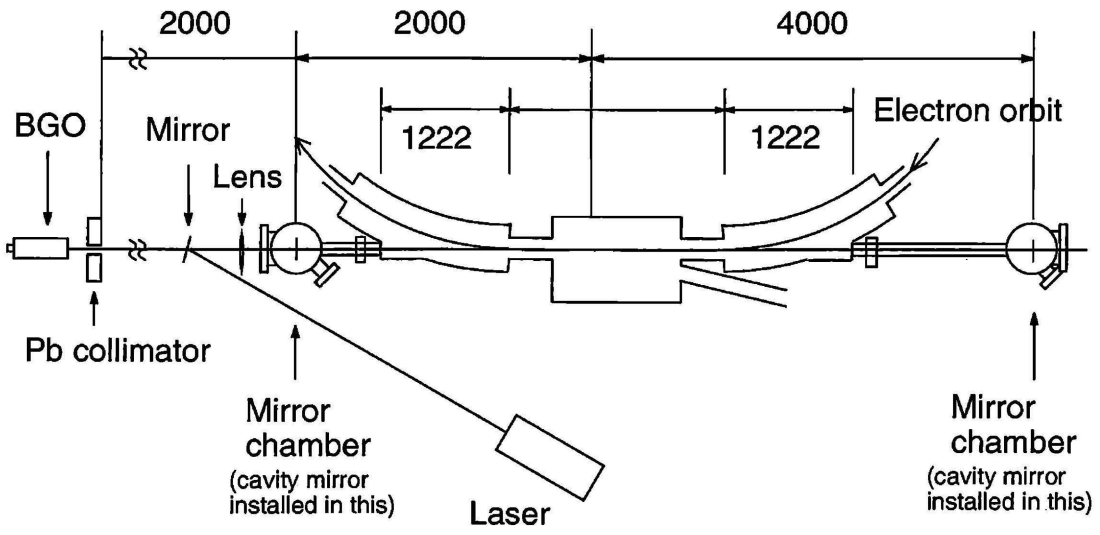


Figure A.7: Experimental setup for the multipass system

Using the newly constructed cavity with two mirrors we have carried out the experiment to test the performance of the system using the LC1 line in TERAS. The experimental setup is shown in Fig A.7. Generated LCS $\gamma$-rays were measured with BGO scintillator ($2inch\phi \times 6inch$) and the data were recorded in personal computer after histgramized with MCA. Experimental conditions are given in Table A.2.

We used the laser with visible wavelength (532nm). This can generate the LCS $\gamma$-ray in the energy range of 2-20MeV (see Section 2.2). The adjustment of the optical system was performed visually with the transmitted light through the mirror and the scattered light from the surface of the mirror. Since the diameter of this laser was about 3mm$\phi$, the diameter of the mirror M1 was 3.2mm$\phi$.

Before installing the mirrors in the mirror chamber, this optical system was built and its performance was tested. And the spot size of laser beam on the mirror and the transmissivity were measured with the iris-narrowed-down-holder and the laser power meter, respectively. The spot size of laser beam was less than $3.4mm\phi$ on the hole opening mirror, and the transmissivity was about 97%.

After installing the mirror and adjusting the optical system, we confirmed that laser beams focussed at the focal position of the cavity 4 times, which was the maximum number expected from the calculation.

We used very low electron current of 8-9mA. This was because when the current was high, the current value changed violently with time. The laser track and the electron orbit were finely tuned so that the yield of generating $\gamma$-rays might become maximum.

Table A.2: The experimental conditions

| | | |
|---|---|---|
| TERAS<br>LC1 course | electron energy | 512MeV |
| | stroage current | 7.78-9.20mA |
| | electron spread | horizonal $\sim 2mm$<br>vertical $\sim 0.5mm$<br>divergence $0.1mrad$ |
| laser<br>Showa Optronics JUNO5000 | wave length | 532nm |
| | mode | CW |
| | beam spot size | about 3mm dia. on the mirror |
| | divergence | $< 0.5mrad$ |
| | power | 2.0W(MAX5.0W) |
| mirrors<br>CVI corp. multilayer dielectric mirror | refectivity | 99.7% or more at 532nm |
| | hole-opening mirror | f=2000mm,50mm dia. of the mirror ,<br>3.2mm dia. hole<br>at the center of the mirror |
| | hole-less mirror | f=4000mm,50mm dia. |
| generated $\gamma$-ray maximum energy | | 9.3MeV |
| $\gamma$-ray collimator | | about 0.54mrad |
| mesurement time | | about 100 sec on each run |

## A.5 Results

The $\gamma$-ray spectrum measured with the BGO is shown in Fig.A.8, where 'multipass' expresses the spectrum when using a multipass system. The 'singlepass' expresses the spectrum for the singlepass system. It turns out that the amount of photons is increasing clearly compared with singlepass system. The $\gamma$-ray flux was calculated by subtracting the background, and thus-obtained flux was $182 photons/mA/W/sec$ for the multipass system and $69 photons/mA/W/sec$ for the singlepass system. Here after correcting for the transmissivity we could obtain 2.6times intensive LCS $\gamma$-rays with use of the multipass system than the single pass system.

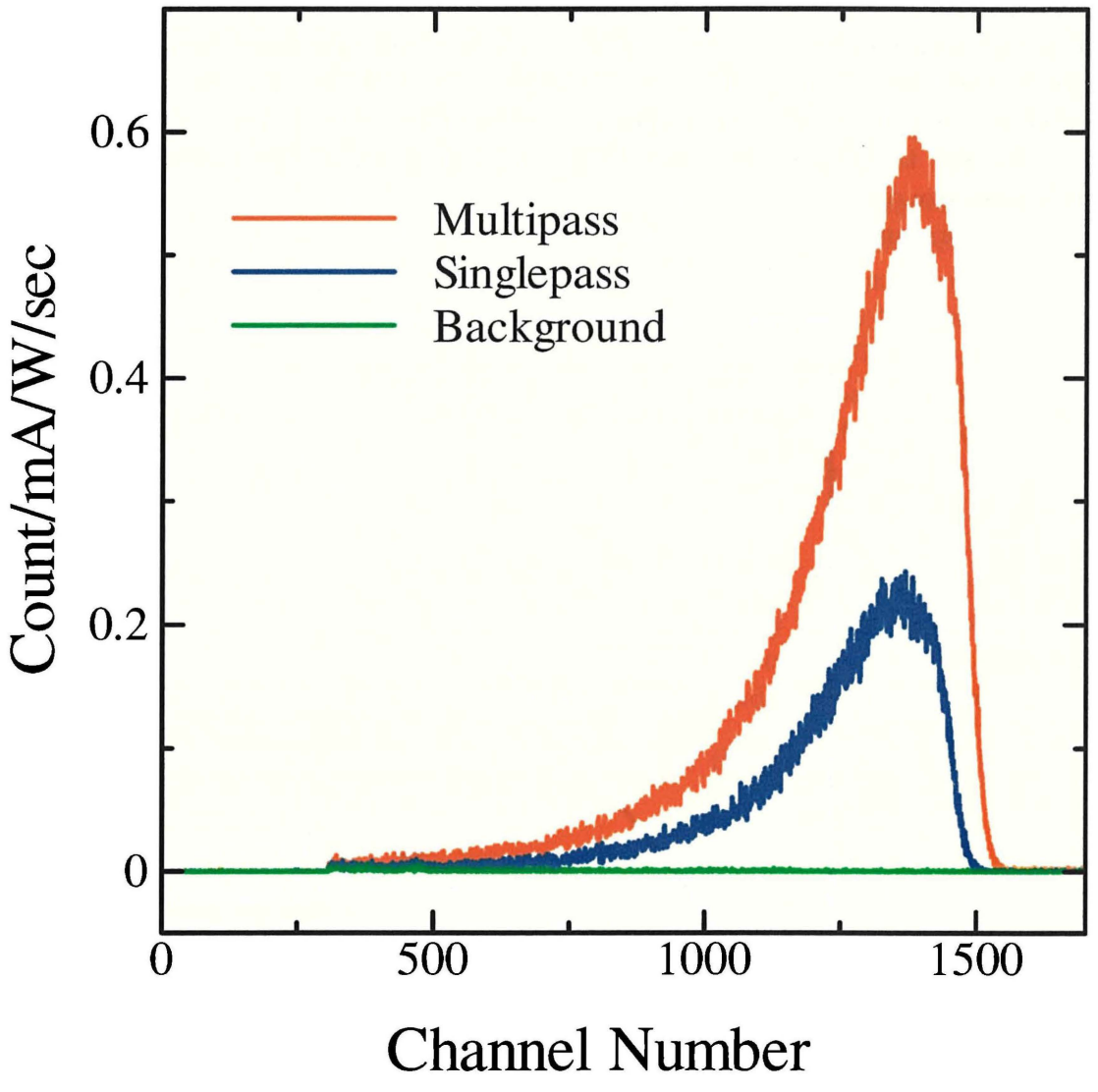


Figure A.8: Measured $\gamma$ ray spectrum for the single pass and the multi pass system, respectively.

## A.6 Discussion

When we used the multipass system, the LCS $\gamma$-ray flux increased by a factor of 2.6 (=182/69 $\times$ 0.97; 0.97 is transmissivity correction) compared with the singlepass system. This amplification factor of 2.6 is in good agreement with calculations (Section A.2.2). Comparison of the experiment with the calculation is shown in Fig.A.9.

In order to increase the $\gamma$-ray flux it is important to increase the number of collision between reflected laser photons and electrons. The available collision number is determined by the size of the incident laser beam. In order to make one more collision in the present system the size of the incident laser beam should be 1.6mm$\phi$. The size of laser spot depends on the performance of the optical system and laser system.

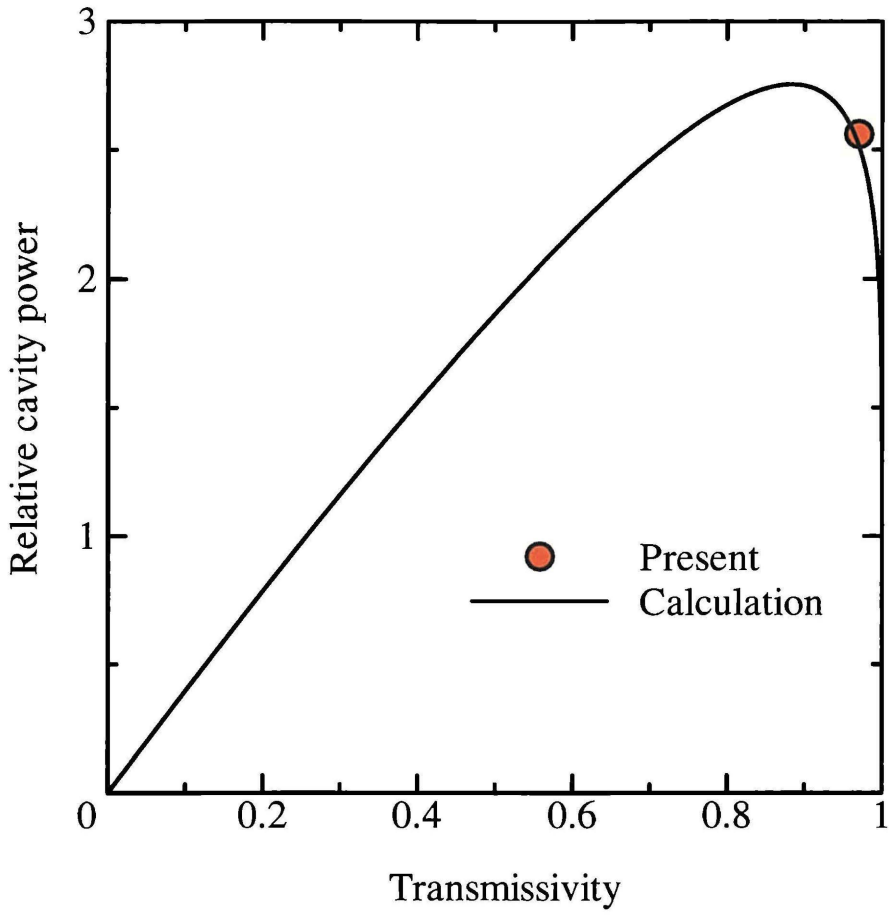


Figure A.9: Comparison of the measured amplification factor with the calculated one.

## A.7 Conclusion

Following the strong requirement of increasing the LCS $\gamma$-rays flux for experiments, we developed the multipass system. The optical system developed here does not need the mode-locking laser, and therefore one can generate the pulsed LCS $\gamma$-rays. Furthermore since the $\gamma$-rays are generated by head-on collision, long interaction length can be available.

We have tested the performance of the multipass system by using a laser with visible wavelength of 532nm. We succeeded to increase the LCS $\gamma$ ray flux by a factor 2.6 for the first time in the world.

In order to increase the LCS $\gamma$-ray flux further we propose to construct the following optical system as shown in Fig.A.10. Two mirrors, M1 and M2, with different focal distance are placed so that the focus position of the M1 where electron beams are most converging may coincide with that of the M2. Laser beam is introduced into the cavity in parallel with the electron beam axis and then it follows a track as shown in Fig.A.10. Repeating the collision of the laser with electrons, the orbit of the laser beam approaches the electron beam axis. Finally, the laser beam is just on the straight-line of the electron orbit and continues going and coming back on the electron beam axis. In principle, the laser power within the cavity becomes infinite.

The point of this optical system is that the internal cavity power becomes infinite and thus one can expect many collisions of the laser with the electrons.

We calculated the expected performance of this system and found the following problems.

1. This optical system is sensitive to the position of the mirror and the change of the angle of the mirror.

   For example, if the angle of the mirror changes by 0.1 $mrad$ or the position of the mirror changes by 2mm in the z direction from an initial place, the round trip number becomes about 15 but not infinity.

2. The divergence of laser beam

   In many round trips, the divergence of laser beam affects the collision of photons with electrons greatly. The divergence and the spot size of the laser which has the best position resolution among the lasers are 0.5mrad and about 2mm$\phi$, respectively. The spot size of $\phi$2mm of incident laser beam becomes $\phi$5mm after the first collision and $\phi$11mm after the second collision and so on. Comparing the spot size of the laser with that of electron beam ($\Delta x = 1mm, \Delta y = 3mm$), the size of the laser is quite large, and thus the yield of generated $\gamma$-rays becomes low. From the yield calculation of

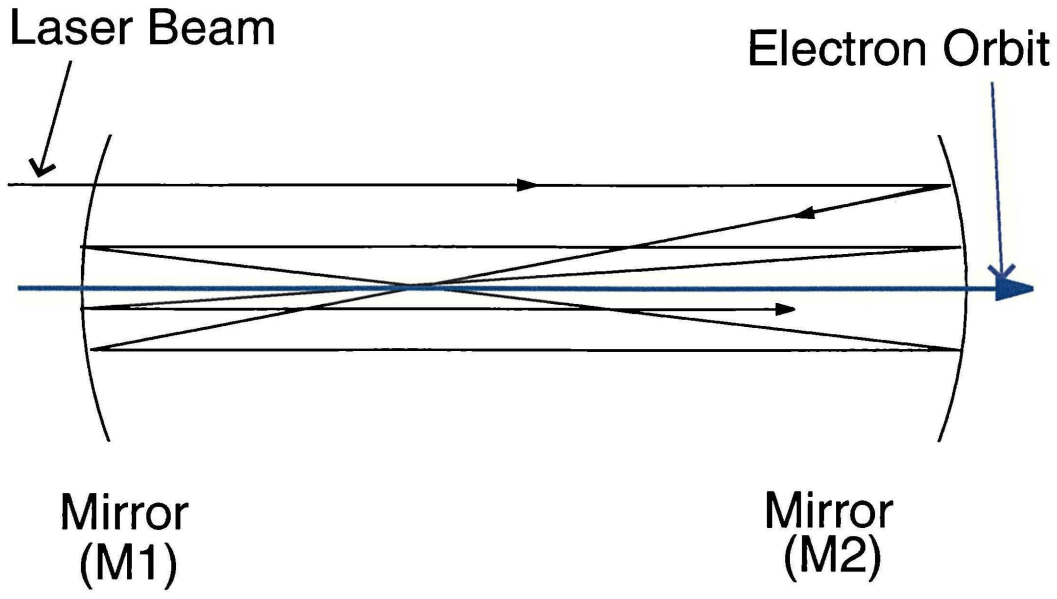


Figure A.10: Proposed new optical system

generated $\gamma$-rays for the laser with divergence of 0.5mrad, it turns out that the yield in ten round trips is about 0.8 times of the singlepass.

We did the experiment using the 0.5mrad laser and we found the maximum number of collisions of electrons and laser photons was 6 collisions.

The possible reason why the collision number is smaller than the expected number is due to the lack of the exact information about the position of the electron beam. In the experiment, the position was monitored using the synchrotron orbital radiation. However the exact position could not be obtained from the information of the radiation and it was quite difficult to control the electron orbit with that information. Therefore, after setting the optical system roughly, we searched the electron beam axis by monitoring the $\gamma$-ray flux. Since the adjustment of this optical system took time very much, the work was very hard.

Now, at the Electrotechnical Laboratory, there is a plan to install an electron beam monitor into the beam tube for the multipass system to know the electron beam orbit more precisely.

We can now get the laser system with the same wavelength having the divergence of less than $30\mu rad$ of divergence and power of over 40W. When we use this laser, we can make 16 round trips. Then the yield increases by a factor of 8.5 of the singlepass.

# Bibliography

[1] L.Federich et al.,IL NUOVO CIMENTO,vol.59B,N.2,247(1980)

[2] L.Federich et al.,LETTERE AL NOUVO CIMENTO,vol.27,N.11,339(1980)

[3] M.Fujita et al.,Nucl.Instrum.Methods Phys.Res., A375, ABS14(1996).

[4] J.P. Jorda et al., Nucl. Ins. Meth. A412,1(1998)

**Acknowledgements**

First and foremost, I would like to thank my thesis advisor, Prof. Yasuki Nagai, for providing me with many advises to carry out this research. His enthusiasm and physical intuition were the decisive factors for the completion of this research. His guidance during the span of my graduate career cannot be adequately acknowledged.

Special thanks are offered to Dr. Tatsushi Shima for spear-heading the completion of the various stages - always with an eye on the scope of the overall experiment. His expert advice and guidance were essential in competing this experiment and data analysis.

I would also like to thank Dr. Hideaki Ohgaki and Dr. Hiroyuki Toyokawa at ETL for their un-tiring efforts provided the necessary conditions to run the experiment and for providing me with the opportunity to develop the multi-pass system.

I would like to thank Prof. Takahisa Itahashi and Dr. Keiji Takahisa for their advice and encouragement through this research.

I would like to pay tribute to the other members of this experimental collaboration. They are: Kouichi Tamura, Hiroyuki Makii and Kenji Mishima. Their supports by day and night, I express deep gratitude.

I would like to thank Japan Society for the Promotion of Science for the financial support.